ABSTRACT

Title of Document: NANOSCALE MANIPULATION, PROBING, AND ASSEMBLY USING MICROFLUIDIC FLOW CONTROL

Chad Ropp, Ph.D., 2013

Directed By: Professor. Edo Waks
Department of Electrical and Computer Engineering

Nanoparticles have unique properties that can be beneficial in fields ranging from quantum information to biological sensing. To take advantage of some of some of these benefits, techniques are required that can select single particles and place them at desired locations with nanoscale precision. This capability allows for bottom-up assembly of nanoparticle systems and facilitates development of improved tools for probing nanoscale physics. Current manipulation approaches are inadequate for positioning nanoparticles such as single quantum dots. Quantum dots can act as single photon sources, and are useful for applications in nanophotonics and quantum optics. In this thesis, I present a technique for manipulation of single quantum dots and other nano-objects. Using this technique, I demonstrate nanoparticle manipulation, assembly, and probing with nanoscale precision.

The nanomanipulation approach I introduce employs electroosmotic flow to position colloidal nanoparticles suspended in an aqueous system. Single quantum dot

manipulation is demonstrated with a precision better than 50 nm for holding times of up to one hour. This technique is useful for studying the behavior of single quantum dots and their interactions with the environment in real time. A fluid chemistry was developed for the deterministic immobilization of nanoparticles along a two-dimensional surface with 130 nm precision. In addition, a technique for assembling systems of silver nanowires is demonstrated. A method for imaging the local density of optical states of silver nanowires is presented using single quantum dots as probes, achieving an imaging accuracy of 12 nm. Spontaneous emission control is accomplished simultaneously by placing the quantum dot at various locations along the wire. Together, these experiments illustrate the versatility of microfluidics for the advancement of nanoscience research and engineering.

NANOSCALE MANIPULATION, PROBING, AND ASSEMBLY USING MICROFLUIDIC FLOW CONTROL

By

Chad Ropp

Dissertation submitted to the Faculty of the Graduate School of the
University of Maryland, College Park, in partial fulfillment
of the requirements for the degree of
Doctor of Philosophy
2013

Advisory Committee:
Professor Edo Waks, Chair
Professor Christopher Davis
Professor Thomas Murphy
Professor Benjamin Shapiro
Professor John T. Fourkas

Acknowledgements

First, I would like to acknowledge and thank my advisor, Prof. Edo Waks, for his support throughout my Ph.D. He encouraged me with my research and taught me to always explore options and seek improvements in my academics and research. He taught me everything I know about building optical setups and helped me grow into the experimentalist I am today. I started my research project with a question poised by Edo, asking whether single quantum dots could be positioned using microfluidics. The solution to this question grew to become the focus of my research. Through Edo, I learned the importance of always asking questions.

I would like to thank my defense committee Prof. Benjamin Shapiro, Prof. Christopher Davis, Prof. Thomas Murphy, and Prof. John Fourkas. Specific thanks go to Prof. Shapiro who has been like a second advisor to me. He always provides a thoughtful perspective on my research and has never hesitated to help me when I needed it. My research would not have been possible without him. In addition, I would like to thank Prof. Fourkas whose collaboration and discussions have also been central to my success.

Over the years I have had many other mentors that I would like to thank. I greatly appreciate collaborations with Prof. Srinivasa Raghavan, who was instrumental in helping start my research project. I would like to thank Prof. Julius Goldhar for introducing me to scientific research and getting me interested in optics. I am also grateful for discussions with Prof. Nader Engheta, Dr. Glenn Solomon, and Dr. Peter Carmichael.

I would like to thank all my research colleagues: Dr. Roland Probst, Zach Cummins, Dr. Rakesh Kumar, Kunqiang Jiang, Dr. Linjie Li, Sijia Qin, Dr. Sanghee Nah, Dr. Kathleen Monaco, Dr. Farah Dawood, and Dr. Samrat Dutta. Special thanks goes to Dr. Probst for mentoring me on microfluidics and Zach for always being willing to help me in the lab. I would also like to thank Dr. Pramod Mathai and Brian Edwards for useful discussions. In addition, I want to thank the clean room technicians at Maryland: John Abrahams, Jon Hummel, and Tom Loughran and at NIST: Jerry Bowser and Lei Chen. All of whom where helpful instructing me on how to use clean room equipment.

I want to thank my labmates, past and present, Dr. Deepak Sridharan, Sina Sahand, Shilpi Gupta, Dr. Ranojoy Bose, Dr. Hyochul Kim, Kangmook Lim, Thomas Shen, Shuo Sun, Tao Cai, and Dr. Kaushik Roy. I would also like to thank all undergraduate and high school students who have worked along side me in the lab: Armand Rundquist, George Luo, Vikas Mendhiratta, and Emily Lathrop. Thanks for making this time memorable!

Finally, I want to thank my family and friends. Thanks to my parents who have always supported me and encouraged me with my life decisions. Thanks to my sisters and their families who have grounded me and always been there asking about my research. And I want to thank Rebecca for being especially supportive of my time researching.

Table of Contents

List of Figures

Figure 5: Trajectory of a controlled QD. (a-c) Time-stamped CCD camera images of a single quantum dot being steered along the desired trajectory. The white trace shows the measured path of the quantum dot up until its current location. The square magenta box shows the subpixel averaging window used to determine the current position of the QD. The insets in panel (a) show the orientation of the channel with the trajectory (green) and a close-up of the subpixel averaging window that contains the QD near its center. (d) Plot of QD position along its trajectory. The dotted black line shows the desired trajectory. The measured QD trajectory is shown in blue. The solid red squares denote times when the QD blinks off. At the end of the trajectory the QD is held in place for 2 minutes. The mean displacement from the trajectory is calculated to be 119.5 nm.

Figure 6: QD positioning accuracy. (a) Blue points represent the measured position of the QD as it is held in place for 5 minutes. The standard deviation along x of the blue points is calculated to be 49.3 nm. The controller is subsequently turned off and the QD is allowed to drift away for another five minutes, as shown by the red points. The drift to the right is caused by a small pressure flow in the device that is continuously compensated when feedback control is on. Measured positions of an immobilized QD are shown in green. From the immobilized QD position uncertainty, we measure the vision accuracy of the setup, which has a standard deviation along x of 18.8 nm. Subtracting the vision noise from our measured variance demonstrates that we are positioning with 45.5 nm precision. (b) Histogram of the measured positions along the x direction for a held QD with a Gaussian fit with standard deviation of 49.3 nm. The center of the Gaussian is slightly to the right of zero, corresponding to the small pressure flow towards the right. (c) Calculated positioning precision due to diffusion (dashed red line), vision noise (dotted green line), and both noise sources combined (solid blue line) as a function of camera frame rate.

Figure 7: Characterization of positioning accuracy for a long holding time. Plotted is the measured position of a single QD as it is held at a desired location for one hour. The blue points represent the measured position when the controller was on,

corresponding to a 52 nm positioning accuracy. The red points represent the position of the QD when the controller is subsequently turned off for five minutes. Green data points are the positions of an adhered QD illustrating the spatial uncertainty due to vision noise.

Figure 8: *In-situ* measurements of a single QD. (a) Autocorrelation measurement of a single controlled QD obtained from a 15 minute integration with 1 ns binning and exponential fits shown. From the exponential fit $g^2(0)$ is determined to be 0.37 ± 0.02 and the decay time t_d is determined to be 22.7 ± 1.1 ns. (b) Fluorescence intermittency as measured from a single held QD.

Figure 9. Microfluidic device and setup. (a) The microfluidic device is formed between a glass cover slide and a molded PDMS block. Colloidal CdSe/ZnS QDs are suspended in the photoresist, which is used to fill the channel. Electrodes placed in the four fluid reservoirs provide the voltages necessary to move QDs as desired using EOFC. A UV laser is integrated to expose the photoresist at a central location in the setup. This location can be moved by translating the sample stage. (b) Experimental setup showing a cross section of a microfluidic channel. Dichroic beam splitters are used to integrate the UV source for photoresist exposure and the green source for illumination. Signals from the QDs are filtered and imaged on a CCD camera. Data collected from the camera are analyzed through image processing to determine the location of the QDs. The desired feedback signals are calculated and then sent to the electrodes, the piezo stage, and the UV shutter to coordinate the positioning.

Figure 10. Optical images showing QD films along surfaces. (a-c) Microfluidic channel filled with rheology modifier and the immiscible monomer (0.6% RM-825 and 40% SR-9035) shown at different planes within the device. QDs in focus at both the top (PDMS) and bottom (glass) surfaces can be seen along with a large globule (red) and thin layers of QDs along the channel walls (blue) in the middle of the channel. (d-f) Microfluidic channel filled without the monomer (0.6% RM-825) at the

same planes within the device. QDs are dispersed uniformly vertically throughout the device.

Figure 11. Positioning and immobilization of a single QD. (a-c) A single QD is chosen (magenta box) and moved towards the target location. The line shows the distance between the QD and the target. (d) Image showing the local UV exposure aligned with the target location used to immobilize the QD once it is in place. (e-f) After the QD is encapsulated (magenta box) it does not move with an applied voltage to the top electrode, although the QDs in the surrounding solution do move. Several other QDs are circled in blue in panel (e) and their displacements after one second of flow are shown in panel (f).

Figure 12. Immobilized array of individual QDs. (a) Image of the 3 × 3 array of immobilized QDs with 5 μm spacing within the microfluidic channel. (b) Measured positions of the nine QDs from averaging over many frames. (c) A zoomed-in view of the measured positions for the QD in the center-right of the array with the origin corresponding to its mean position. (d) Image of the 3 × 3 array after channel removal and cleaning, demonstrating that several of the QDs are still emissive. All of the exposed regions have remained adhered to the glass surface (seen as oval shaped bright patches) and the four visible immobilized QDs are shown circled in red.

Figure 13. Immobilization of individual QDs to target QDs adhered to the substrate. (a) Spectra of the two different types of QDs and the bandpass transmission spectra of the two filters used to distinguish between them. (b) Relative positions of the nine positioned and immobilized QDs that emit at 655 nm (blue dots) versus their 705 nm targets (all marked by a single red dot at the origin). The average distance between an immobilized QD and its target QD was measured to be 155 nm. The two circles denote the sample QD pair whose pixilated images are overlaid in panel (c), here the red and blue asterisk mark the location of the diffraction pattern centroids inferred by the sub-pixel averaging algorithm.

Figure 14. Array of preselected QDs. (a) Idealized array design with the two different types of QDs alternating in a checkerboard pattern. (b) Completed array as visualized through a bandpass filter centered at 710 nm. The four QDs emitting at ~705 nm are circled in red while the 655 nm emitting QDs are not visible. (c) The same completed array as visualized through the 655 nm band pass filter. The QDs emitting at 655 nm are circled in blue.

Figure 15. Measured position of a QD as the piezo stage was moved in 24 nm increments (a) Measured data showing the subpixel accuracy of our centroiding algorithm. The black data are the measured pixel position of the QD, while the red line is the average position for each step. Discrete steps are seen clearly in the measured data. (b) Measured average position (from panel a) showing the mean and standard deviation compared to the actual position imparted by the piezo stage when converted into actual length units. The blue line denotes when the measured position equals the actual position. In general the measurement has high accuracy and can easily distinguish changes in piezo displacement.

Figure 16. Array of immobilized dots and their measured $g^2(\tau)$s. (a) Image of the 2 × 2 array of QDs spaced 5 μm apart. (b) The corresponding $g^2(\tau)$ measurements for each of the four respective QDs. Autocorrelations are taken over a 1 minute integration time while the QDs are still in the channel. The measured $g^2(0)$s are 0.29, 0.26, 0.26, and 0.35 and all show signs of the photon antibunching that is characteristic to quantum emitters.

Figure 17. Proximity of QDs to the surface. (a) Graph of the diffraction spot size of an encapsulated QD at varied focal distances from the surface. At each position the diffraction spot size was measured many times (blue data points) and a median size (black points) was calculated. A fit was used to find the location of the minimum spot size (black line), establishing the vertical position of the QD. (b) Measured in-focus vertical positions of three encapsulated QDs (red) and three QDs adhered to the

surface (black) with corresponding error bars. The blue circle denotes the data point corresponding to measurements shown in panel a.

Figure 18: Illustration of nanowire positioning through two obstacles. {ii-v} Time-stamped images. In all figures arrows denote direction of fluid flow.

Figure 19: (a) Scatter plot of the measured centroid location of a nanowire held in place by flow control. (b-c) Histograms of the measured positions in the direction perpendicular and parallel to the wire axis.

Figure 20: (a){i} Illustration of nanowire rotation using a nanoparticle pivot. {ii-v} Time-stamped images. (b){i} Illustration of nanorod rotation using a nanoparticle pivot. {ii-v} Time-stamped images. (c){i} Illustration of nanowire rotation using a polymerized obstacle, created by UV-exposure (purple). {ii-v} Time-stamped images. Green crosshairs denote the aligned location of the UV laser. In all figures, arrows denote direction of object translation and rotation and green circles indicate location of pivot obstacle

Figure 21: (a) Orienting a nanowire by immobilizing one end. {i-ii} The wire is positioned by flow control, where a local UV immobilizes one end of the wire. {iii-iv} The wire is then rotated about this pivot point and held at vertical orientation. {v} The stage is translated so the UV is aligned to the second end. {vi} A second UV exposure immobilizes the second end. {vii-viii} Another wire is positioned with flow control (in blue) to show that the first wire is immobilized. (b) Composite image from several frames of a wire rotating 360° about its immobilized end.

Figure 22: (a) Histograms comparing the measured centroid location of a nanowire that is immobile on a surface (red) with one that is held to an angle by flow control (blue) (b) Histogram of the measured difference in angle from the desired orientation for 15 wires that were fully immobilized.

Figure 23: (a){i} Illustration of QD separation (blue from red) using an AgNW barrier. {ii-v} Time-stamped images. (b){i} Illustration of quantum dot coalescence (blue to red) using an AgNW barrier. {ii-v} Time-stamped images. In all panels arrows denote direction of particle motion and green delineates the location of the obstacle barrier.

Figure 24: (a){i} Illustration of nanorod alignment to an nanowire guide. {ii-v} Time-stamped images. (b){i} Illustration of nanowire rotation using the foothold of an nanowire barrier. {ii-v} Time-stamped images. In all panels arrows denote direction of fluid flow and object rotation and green delineates the location of the obstacle barrier.

Figure 25: Images of nanowire structures assembled using our toolbox of techniques.

Figure 26: QD polarization in a microfluidic channel. The emission anisotropy of three pairs of QDs (a-c) as a function of polarization (which was rotated in time). Each pair consisted of a free-floating (red) and an immobilized (blue) QD. The emission polarizations for each pair were characterized simultaneously using a setup in which the emission was sent through a half-wave plate and then split into vertical (V) and horizontal (H) polarization by a calcite beam displacer. Plotted here is the measured emission anisotropy, $(I_V-I_H)/(I_V+I_H)$, for each QD as the emission polarization is rotated with the half-wave plate. The immobilized QDs demonstrate a clear polarization dependence, however the free-floating QDs appear largely unpolarized. We attribute this lack of polarization for the suspended QDs to rotational Brownian motion, which causes polarization effects to be averaged out if the data acquisition time exceeds the orientational diffusion rate. As a result, free-floating probe QDs behave as effectively isotropic emitters.

Figure 27: Near-field probing with a single QD. (a) Optical image of the microfluidic crossed-channel device. Flow in the center control region (dashed circle) is manipulated in two dimensions by 4 external electrodes (not shown). Scale bar is 500

μm. (b). Schematic of the positioning and imaging technique. A single QD is driven along a trajectory close to the wire by flow control. The coupling between the QD and AgNW is measured either by the radiated intensity from the wire ends or by QD lifetime measurements. The inset shows an SEM image of a typical AgNW used in our experiments with 1 μm scale bar. The x-y coordinate system is defined relative to the orientation of the AgNW, as illustrated in the inset.

Figure 28: QD tracking and positioning accuracy. (a) Scatter plots of the measured positions of a QD over the course of one minute. Red data points correspond to a QD that is immobilized while blue data points correspond to a QD that is held in place by flow control. (b-c) Histograms of the x and y coordinate corresponding to data from panel a. Red bars are the histogram for an immobilized QD, while blue bars are the histogram for a positioned QD. The yellow solid line is a Gaussian fit for an immobilized QD showing a measure standard deviation of 12 ± 1 (11 ± 1) nm along the x (y) coordinate. The black solid line is a Gaussian fit for the positioned QD with standard deviation of 36 ± 2 (40 ± 2) nm for the x (y) coordinate.

Figure 29: Coupling a QD to an AgNW. (a-c) This series of images shows coupling of the QD to the AgNW as the QD is moved closer to the wire. The scale bar is 500 nm and intensities are plotted on a logarithmic scale. The red and blue boxes show the image integration region used to calculate the radiation intensities and positions of the QD and the wire ends, respectively. The measured location of the QD is labeled with a red star and the axis of the AgNW is labeled with a blue dashed line.

Figure 30: Scanning Trajectories. (a) Mid-wire scanning trajectory (corresponding to Figure 31). (b) A trajectory scanning the wire tip (corresponding to Figure 34). (c) A trajectory scanning the wire along the side (corresponding to Figure 36). Blue points connected with lines correspond to the trajectory points, connected in order of scanning. During the experiment, flow is applied to position the QD to the desired trajectory point for two seconds before moving on to the next point. Red boxes define the scanning regions. Black lines designate the physical extent of the wire. Some

points along the trajectory lie inside the wire or on the opposite side of the wire, however, since the wire acts as an obstacle the QD cannot generally reach these points and instead is forced against the wire to ensure data is collected as close as possible to the surface. Additionally, the trajectory points are more densely spaced closer to the wire in order to ensure probing of the near-field region.

Figure 31: Probing the LDOS profile near the middle of the AgNW. (a) $\bar{I}$ as a function of position near the middle of the wire. The dashed region indicates the assumed location of the AgNW surface. (b) $\bar{I}$ as a function of distance from the wire axis (x coordinate) using data from panel a. The blue line indicates the best fit to a modified Bessel function. The red dotted line is an FDTD simulation of the AgNW evanescent field. The simulation result was fit to the data using an overall scaling factor. (c) Radiative decay of the QD at 200 nm (red squares) and 30 nm (blue circles) distance from the AgNW axis with lifetime fits of 17 and 8 ns respectively. (d) QD lifetime as a function of x position. The second y-axis denotes the Purcell factor corresponding to the measured lifetimes. Colored markers indicate the data points used for panel c.

Figure 32: SPP decay along AgNW length. Ratio of emission intensity measured from both AgNW ends as a function of position along the wire. The black line is an exponential fit.

Figure 33: Spatial accuracy of measured QD positions. (a) Figure 31b with Bessel-function fit. Red lines indicate spatial distance between the measured QD position and position predicted by Bessel-function fit based on the measured intensity. $\bar{I}_{thresh}$ is labeled with a blue line. (b) Plot of σ_d for a range of $\bar{I}_{thresh}$ values. The minimum standard deviation of 12 nm occurs at $\bar{I}_{thresh} = 0.02$ and is represented by the horizontal blue line.

Figure 34: Probing the tip of an AgNW. (a) Scatter plot of measured positions and intensities near the end of the AgNW. The color of each data point corresponds to $\bar{I}$. The dashed region indicates the location of the AgNW. (b) Reconstructed image using a Gaussian-weighted average. The image intensity is normalized by its maximum. (c) FDTD simulation of the AgNW mode profile showing an enhancement at the tip (also normalized by its maximum). (d) Image of the measured QD lifetime as a function of position. The color scale is labeled with both lifetime and Purcell factor.

Figure 35: Spatial accuracy of measured AgNW end positions. (a) Scatter plot of the measured positions of an AgNW end over the course of 1 minute. (b-c) Histograms of the x and y positions with Gaussian fits measuring 24 ± 2 and 30 ± 3 nm standard deviations respectively. A single QD is placed on an AgNW and the position of the wire end is determined by measuring the center of the diffraction spot of the radiated light and fitting it with a Gaussian point spread function. This light radiated from the wire end is much dimmer than the direct emission from the QD. Thus, the accuracy with which we can track the AgNW is worse than the accuracy with which we can track the QD.

Figure 36: SPP wave interference along an AgNW. (a) Scatter plot of the measured QD positions near the end of the wire. The color of each data point corresponds to the value of $\bar{I}$ measured at each location. The dashed region indicates the location of the AgNW. (b) Reconstructed image using a Gaussian-weighted average. The image intensity is normalized by its maximum. (c) Plot of an averaged value of $\bar{I}$ as a function of position along the wire. (d) FDTD simulation of the field intensity standing-wave pattern along the side of the AgNW (normalized by its maximum) with the profile within the dashed wire region corresponding to the field immediately outside the wire. (e) Image of the measured QD lifetime as a function of position. The color scale is labeled with both lifetime and Purcell factor. (f) Plot of QD lifetime measured along the length of the AgNW.

Figure 37: Single QD Spectrum. Emission spectrum (red) of a single QD that was immobilized on a glass coverslip as measured using a grating spectrometer (Acton SP 2758). The black curve is a Lorentzian fit that indicates a spectral linewidth of 17 nm.

Chapter 1: Introduction

1.1 Overview

Continued advances in computational technology rely on reducing power consumption and increasing speed. One possible route to this goal is the use of photons in place of electrons. Photonics can provide larger bandwidth than electronics [1] with low power consumption [2]. Light is also a natural distributer of quantum information that has been suggested as a means of secure communication [3] and faster information processing [4].

Optical computation requires devices that employ interactions between light and matter to perform optical switching. Light-matter interactions are stronger at the nanoscale than in bulk materials due to the quantum mechanical [5] and plasmonic [6] resonances that can occur in nanoscale structures. For this reason, researchers are increasingly focusing on developing nanophotonic systems that exploit nanoscale physics to implement optical logic [2,7,8].

Central to the challenges of nanoscience research is the ability to manipulate and position individual nanoparticles with nanoscale precision. In this chapter I discuss the characteristics of two specific types of nanoparticles, plasmonic nanowires and quantum dots, and outline an approach to position these particles using microfluidic flow control. Chapter 2 provides a detailed study of microfluidic manipulation as it pertains to positioning single quantum dots. Chapter 3 introduces a novel fluid chemistry that enables assembly of single quantum dots on a two-dimensional surface. In chapter 4, I present a toolbox of techniques for manipulating various nanoparticles along a planar surface and demonstrate assembly with single metallic

nanowires. In chapter 5, I demonstrate deterministic probing of plasmonic wires using positioned single quantum dots to image the local density of optical states of the wire. Chapter 6 concludes by discussing some of the future prospects of manipulating nanoparticles with microfluidics.

1.2 Plasmonics

Overview

Plasmonic elements confine electromagnetic energy to the interface between a metal and a dielectric. This excitation is called a surface plasmon polariton (SPP). SPP waves are coherent oscillations of unbound electrons in the metal. In SPP waves, power propagates along the metal surface and electric fields decay exponentially from the interface, as depicted in Figure 1. The large overlap of the electric field with the metal means that SPP waves are lossy. Typical SPP propagation lengths are on the order of several microns [9].

Plasmonics offer a solution to optical diffraction, which is a limiting factor in the development of optical computation. Optical computation requires all-optical switches, which take advantage of the nonlinearities in materials [10]. The challenge of employing optical nonlinearities for switching is that they are weak compared to electronic nonlinearities. To attain the same affect, optical nonlinearities require either longer distances or stronger fields [11]. Plasmonic structures confine light to volumes that are small compared to the diffraction limit, greatly increasing field strength and enhancing optical nonlinearities [12]. Plasmonic structures also can be scaled down to compete with electronics for high on-chip density.

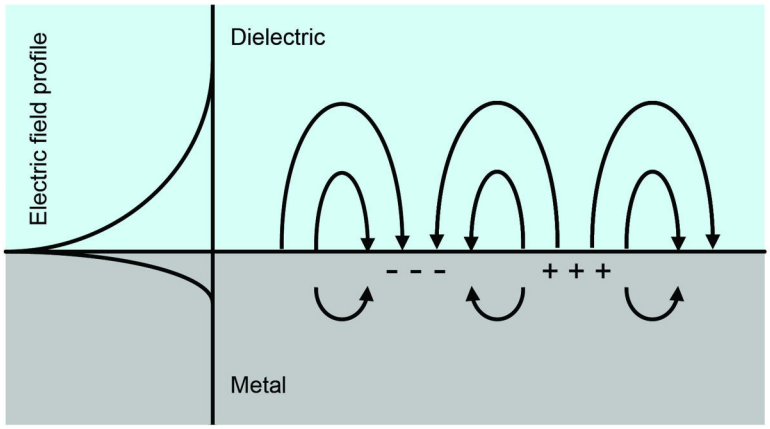

Figure 1: Diagram of the field distribution of a surface plasmon polariton. Unbound surface charges in the metal oscillate coherently and create a propagating electromagnetic wave along the surface. The field profile, which is indicated on the left, extends evanescently into the dielectric and the metal.

Plasmonic nanowires

SPP waves are generally difficult to excite from free space due to the momentum mismatch between SPPs and far-field modes. As a result, exciting SPP waves in metal sheets requires either evanescent-field couplers, periodic gratings, or near-field scatters [9]. Metallic wires support SPP waves, which can be readily excited from the far-field by focusing light on their ends. The wire ends act as far-field to near-field converters and scatter light into the SPP mode [13]. The wire confines SPP propagation with sub-wavelength lateral dimensions. These guided waves can also radiate to the far field from the wire ends, which act as antennas (a reverse process of coupling to the wire). Wire end read-out offers a way to peer into near-field interactions and to study plasmonic propagation and interference effects [14].

Interactions with quantum emitters

Plasmonic wires confine light to nanoscale volumes. A single emitter placed within the mode volume of a plasmonic wire experiences an increase in its rate of spontaneous emission [15]. This increase is useful for creating fast, single-photon sources for quantum applications [16] and optical transistors that could work at the single photon-level [17]. Increased spontaneous emission also suppresses an undesirable non-radiative processes, such as Auger recombination and transitions to trapped states [18]. As a result of these properties, plasmonic objects can greatly improve the emission properties of single emitters.

1.3 Quantum dots

Overview

Quantum dots (QDs) are bright, single-photon emitters. They are semiconductor nanocrystals, whose valence and conduction bands become discrete due to three-dimensional electronic confinement. The discrete energy levels are atom-like and transitions among these levels emit single photons at specific wavelengths [19]. The size, shape, and material composition of QDs affects their emission wavelength [5].

QDs are useful for photonics engineering and biological imaging. They have been integrated with photonic devices to create solar cells [20], LEDs [21], lasers [22], optical switches [2], and single-photon sources [23]. QDs can also be functionalized and used as fluorescent markers in biological tagging [24], imaging [25], and detection [26].

Epitaxial and colloidal QDs

There are two types of QDs— epitaxially grown QDs, which are self-assembled in a solid host medium [27], and colloidal QDs, which are synthesized in solution [5]. Molecular-beam epitaxy is used to create self-assembled QDs. Such QDs form as islands of low bandgap material inside a larger bandgap host. The host is a solid matrix in which the QDs are physically bound. Colloidal QDs are synthesized in a liquid environment. These dots are not restricted to any specific material system and can be dispersed in various liquids and polymers for deposition on substrates [28].

Both types of QDs suffer from size and shape inhomogeneity, resulting in inhomogeneous emission spectra [29,30]. For applications involving single QDs, we desire a technique to place QDs with specific properties at specific locations. Compared to epitaxial QDs, which are bound in place, colloidal QDs can be preselected in their liquid environment and placed deterministically.

CdSe QDs

In this thesis, I demonstrate positioning and measurements using cadmium selenide (CdSe) QDs. CdSe is one of the most developed colloidal QD materials [25]. The core of the QD consists of a CdSe nanocrystal, which may be encapsulated within a variety semiconductor shells to improve quantum yield [29]. Ligands attached to these QDs can stabilize the particles in various liquids including water and organic solvents [26]. Figure 2 compares the emission spectrum of a single CdSe-ZnS core-shell QD with that of an ensemble of QDs (OceanNano Tech® vendor), which are

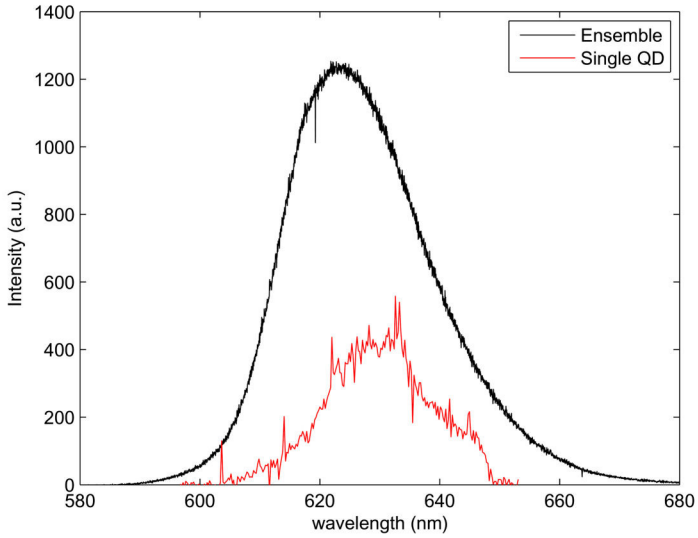

Figure 2: Plot comparing the spectrum of a single CdSe/ZnS QD with its ensemble.

found to have linewidths of 17 nm and 27 nm respectively. The difference in linewidth indicates the spectral inhomogeneity of commercially available QDs.

CdSe QDs are versatile light sources that can be integrated in nanophotonic systems [15,31]. One can also employ these QDs to study nanoscale physics. Their nanoscopic size makes them ideal for probing optical features at high-resolution [32]. QDs can be used to communicate near-field interactions to the far field for studying nanoscale phenomena [33]. The ability to position single QDs deterministically can enable control of nanoscale interactions for improved nano-engineering.

1.4 Microfluidic particle positioning

Overview

Deterministic placement of individual nanoparticles is an ongoing challenge in nanoscience. The ability to choose a single nanoparticle with desirable characteristics

and to position it in a determined location is essential for the emerging field of nano-engineering. Such a technique could enable the assembly of multiple nanoparticles to build nanoscale systems or to probe interactions at the nanoscale. In this thesis, I present a technique to position single nanoparticles for both assembly and probing. In particular, I focus on the manipulation of single colloidal quantum dots with nanoscale precision, which has remained a difficult goal for nanoscience research [34–36].

One of the most developed techniques for positioning microscopic particles is optical tweezers [37]. In optical tweezers, the gradient force of a focused laser creates a three-dimensional potential that traps a particle. Translating the laser focus will drag along particles trapped within this potential. However, the trapping force of tweezers is proportional to the polarizability of the object. An object's polarizability depends on its material composition and size [37]. As a result, not all objects can be positioned with optical tweezers. The force produced to trap an object scales with the object's volume. For small enough particles these forces cannot overcome random diffusion, and the objects cease to be trapped. Particles can also be manipulated using magnetic tweezers [38] or dielectrophoretic actuation [39], but these methods suffer from similar problems as optical tweezers.

In other techniques, tapered-probe tips allow for direct mechanical positioning of particles along a surface [40]. These approaches are generally independent of particle size, but can be highly dependant on the properties of the surface and interactions with the particle [41]. This type of mechanical positioning also requires mechanically stabilized probes, which can cause damage the object being manipulated [42].

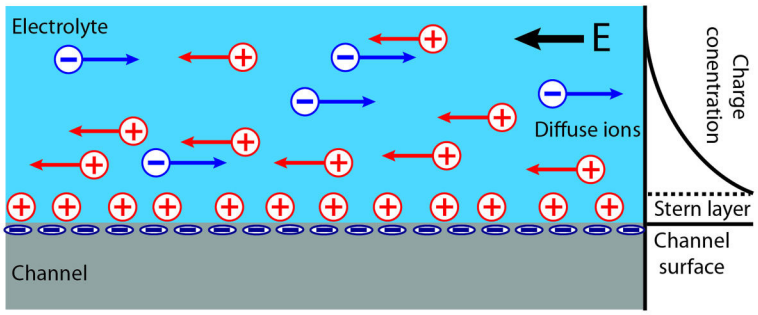

Figure 3: Diagram of the Debye layer that forms at the interface between the electrolyte and the channel wall. Ions from the liquid adsorb onto the surface (blue "-" charges). A shielding Stern layer of cations forms along with a concentration of diffuse cations in the region above the surface. The predominance of cations in the diffuse region facilitates electroosmotic actuation.

Electroosmotic flow control

Electroosmotic flow control allows for positioning of single nanoparticles. With this technique, suspended particles are moved by actuating flow of the surrounding liquid. Compared to other approaches, electroosmotic flow control exhibits several key advantages. First, object positioning arises from fluid actuation, which is independent of the composition of the particle. Second, particle diffusion in the liquid is the main limitation to control. Diffusion scales with object length (instead of volume), which makes flow control better suited to position nanoscale objects than techniques like optical tweezers. Finally, fluidic forces can position delicate objects without damaging them from local heating [43] or mechanical friction [42]. As a result, electroosmotic flow control is well suited for positioning a variety of nanoparticles.

In electroosmosis, an electric field actuates flow of an electrolyte solution through a capillary channel [44]. Fluid actuation results from ion motion in the Debye layer that

forms at the surface of the channel. Figure 3 illustrates the structure of the Debye layer and its behavior under an applied field. Ions from the liquid adsorb to the surface of the channel (shown here with flattened negative charges). A subsequent screening layer (the Stern layer) forms immediately above the surface and remains fixed there. The diffuse ions above the Stern layer move with the applied field. These ions have predominantly the same charge and exhibit net motion, which causes the bulk of fluid in the channel to flow, including any suspended particles.

Incorporating feedback control with electroosmotic actuation enables dynamic positioning of suspended particles. This positioning is achieved using a microfluidic cross-channel to actuate electroosmosis in two dimensions [45]. Vision-based tracking measures a particle's position in real time as it moves with the flow. The position is input into controller software to determine how to actuate electroosmotic flow and move the suspended particle along a desired path. Feedback control of fluid actuation is used to incrementally adjust any deviation in motion from the particle's desired path in order to achieve accurate positioning.

Chapter 2: Manipulating quantum dots with nanometer precision by flow control

2.1 Introduction

Manipulation and control of nanoscopic objects such as QDs is a fundamental requirement for a broad range of applications in the fields of photonics, nanoelectronics, and biology. In particular, there is currently great interest in precise placement of pre-selected particles with desired properties, such as emission spectrum or brightness, on patterned or functionalized surfaces to engineer nanophotonic and nanoelectronic systems. Some important examples include the precise placement of single QDs in the high field region of nanophotonic [46–48] or plasmonic [15,49] structures for scalable engineering of quantum information processors [50] and nanoscale electronic circuits [51]. Manipulation of QDs serving as biological tags could also enable *in situ* characterization of biological molecules and the controlled investigation of biological processes [25].

To date, the most notable successes of nanoparticle manipulation have involved optical tweezers [36,52] and optofluidic devices [53,54]. These methods make moveable, active traps, either by laser-created optical gradient forces or by dynamic virtual electrodes that exert dielectrophoretic forces on polarizable particles. However, optical and dielectric forces scale with volume, making the trapping of nanoscopic objects such as QDs challenging [37]. Furthermore, these trapping forces are non-specific, in that all particles are pulled in, resulting in a significant probability for capturing multiple objects. In quantum optics applications, the capture of multiple particles can ruin the single-photon nature of the emission. For biological applications, the use of high-power lasers for optical trapping can easily damage

biological objects [43]. Thus, the development of particle manipulation methods that scale more favorably with particle size and do not require high power lasers is needed.

In this chapter I demonstrate a method for manipulation and positioning of nanoscopic objects with nanometric precision in two dimensions without using traps. Instead, manipulation is achieved by moving the surrounding fluid via electroosmosis, in which an applied electric field moves a layer of surface ions that pulls the fluid, along with any suspended objects, by viscous drag [44]. The position of a chosen object is measured in real time with a microscope and a sub-pixel imaging algorithm that provides sub-wavelength precision [55]. Flow is then created to move that object continuously from its current location towards its desired position in discrete time steps. This continual sensing and correction of errors (feedback control) enables nanometric precision for positioning. Only the chosen object is always corrected back towards its target location. All other nearby objects are not controlled, and drift away by a combination of random Brownian motion and diverging non-correcting fluid flows at their locations in the device. This flow control approach is particularly promising for the manipulation of extremely small dielectric particles, such as QDs, for which trap-based approaches are limited [37] due to the small particle volumes. To demonstrate this advantage, the work in this chapter focuses on the manipulation of single QDs which have an ellipsoidal core/shell structure and a radius of 6 nm (3 nm) on the major (minor) axis.

2.2 Electroosmotic flow control

Flow control has previously been used to manipulate particles with micrometer precision [34,45,56–60]. Improved methods based on rotating laser sensing [61–64] enabled random capture of nanoscopic objects for short times with nanometric precision [65–67]. The ability to position and hold pre-selected nanoscopic objects with nanometric precision has proven significantly more challenging due to their small size, which increases Brownian motion and makes it hard to visualize their location accurately. QDs are particularly difficult to manipulate due to their inherent blinking, which renders them invisible for prolonged periods of time [68]. During these "dark" periods, a QD can drift a significant distance away from its last observed location. For this reason, previous capturing methods were limited to 90-second trapping times [34]. The approach demonstrated here enables any QD in the field of view to be moved from its current position to any desired location over a well defined path with nanometric precision for times exceeding one hour. In addition, since we have the ability to manipulate the QD over a large control area, our technique is insensitive to QD blinking. When a QD blinks off, we can wait for it to blink back on and immediately reposition it back to the correct location even if it has drifted a significant distance away due to Brownian motion.

Figure 4a illustrates the device and operating principle used to manipulate single QDs using flow control. The device is composed of two microfluidic channels that intersect at a 90° angle. This design is patterned into polydimethylsiloxane (PDMS). The PDMS is adhered to a glass cover slip to form the microfluidic channels. The

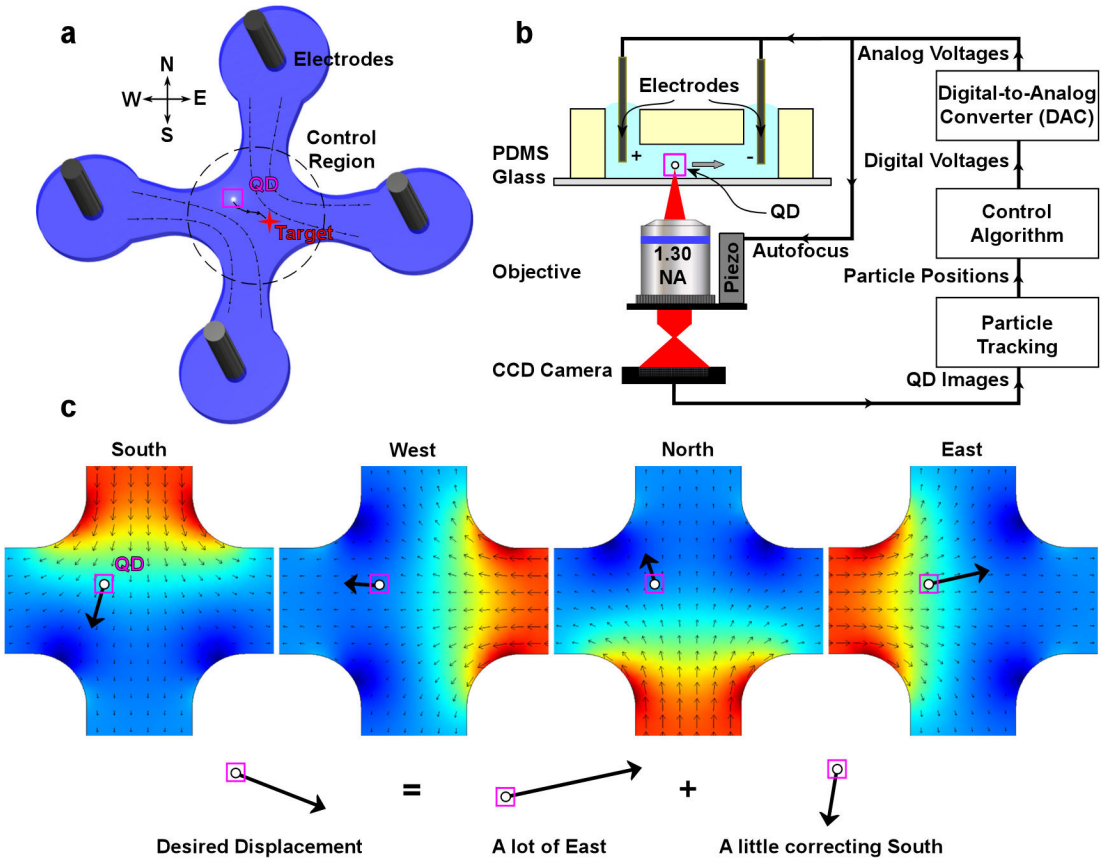

Figure 4: Experimental setup and control principle for flow control. (a) Schematic of our microfluidic device structure for 2D control of nanoparticles. An intersection between two microfluidic channels forms the control chamber of the device. Electrodes positioned in the fluid reservoirs actuate flow electroosmotically, while feedback is used to correctly move the nanoparticle to its target location. (b) Illustration of the optical and electronic setup for tracking and feedback control of QDs. A CCD camera images the QD and sends the information to a tracking algorithm that uses subpixel averaging to accurately determine the current position of the QD. The control algorithm uses this information to determine the proper voltage to apply to the electrodes in order to move the QD to its desired position. A second feedback loop moves the imaging objective in the z direction using a piezo stage to keep the QD in focus. (c) Model of the four flow modes resulting from voltages applied to each electrode. Any desired correcting velocity, at any particle location, can be created by combining these four actuation modes. (Black arrows show the microfluidic velocities, color shows the applied electric potential, and the enlarged black arrows show a representative velocity decomposition).

control region is located at the intersection of the two channels and is approximately 5 μm in height and 100 μm in diameter, although it can easily be made larger. The four cardinal directions are labeled in panel a, which are used to describe particle motion. Electroosmotic flow actuation is created by electrodes placed in four fluid reservoirs at the ends of the channels. The channels are subsequently filled with an aqueous fluid containing CdSe/ZnS QDs (Qdot® 655 nm ITK™ amino), along with a mixture of mass fraction 1.25 % of an associating polymer (RM-825, Rohm and Haas Co.) [69] and 0.55 % of a zwitterionic betaine surfactant [70]. The associating polymer is used to increase the viscosity of the fluid to 0.23 Pa-s by hydrophobic clustering [69] to decrease QD Brownian motion, while the surfactant is used to enhance fluid actuation. The colloidal QDs are illuminated with 532 nm light at an intensity of 250 W/cm^2 and imaged using an inverted microscope.

The tracking system with the feedback control loop is depicted in Figure 4b. Images are acquired from a CCD camera at a 20 Hz frame rate and then processed in real time using a centroid algorithm for precise determination of the position of the QD. The control algorithm then calculates the voltages needed to move that QD in the required direction by decomposing the desired displacement vector into components of fluid motion in the four cardinal directions (North, South, East, and West) that can be actuated by each electrode, as illustrated in Figure 4c. The magnitude of the actuation is set by a control gain. In our device, the size of the electroosmotic actuation can depend somewhat on the height of the QD due to a different zeta potential at the top PDMS versus the bottom glass substrate. Electrophoretic forces can also contribute to the actuation, but for QDs they are much weaker than the

actuation due to electroosmotic flow. The control gain is set to an intermediate value that achieves good manipulation over the entire height of the device. Once computed, the necessary voltages are applied to each of the four electrodes to move the QD as desired. Platinum electrodes are used to minimize unwanted electrochemistry effects in the fluid [44]. Although the target QD is controlled in the plane, the QD can still drift slowly in the third dimension, causing it to go out of focus and thus degrading the performance of the vision-based control. To correct for this effect, the imaging objective is mounted on a piezo stage and a second Newton-bracketing feedback control algorithm uses the width of the QD image as its metric to track the QD in the z direction, thus keeping it in focus. This approach improves control precision in the xy plane.

2.3 Characterization of positioning accuracy

The ability to manipulate QDs precisely in two dimensions is shown in Figure 5. A single QD is selected from the 100 μm × 100 μm control region that contains approximately 10 QDs. A small area around the QD, denoted by the box, defines the 16 pixel × 16 pixel tracking window used to calculate the QD position via the centroid algorithm. Panels (a-c) show the position of a single QD at several different times as it is controlled along a well-defined path. The inset to Figure 5a shows the orientation of the trajectory with respect to the cross channel and a close up of the tracking window. The desired position was moved along the fixed trajectory at a speed of 2 μm/s while the control algorithm continuously adjusted the applied voltages to move the QD towards this moving target. To determine whether the QD

had blinked off, a threshold camera intensity was selected. When the camera signal fell below this threshold, all voltages were switched to zero and the controller halted to wait for the QD to begin re-emitting. While waiting for the QD to resume photon emission, the tracking region was temporarily expanded to three times its size to ensure that Brownian motion would not carry the QD out of the detection window before it began re-emitting. The full trace of the QD position is shown in Figure 5d and is overlaid on the desired trajectory. The times when the QD blinks 'off' are

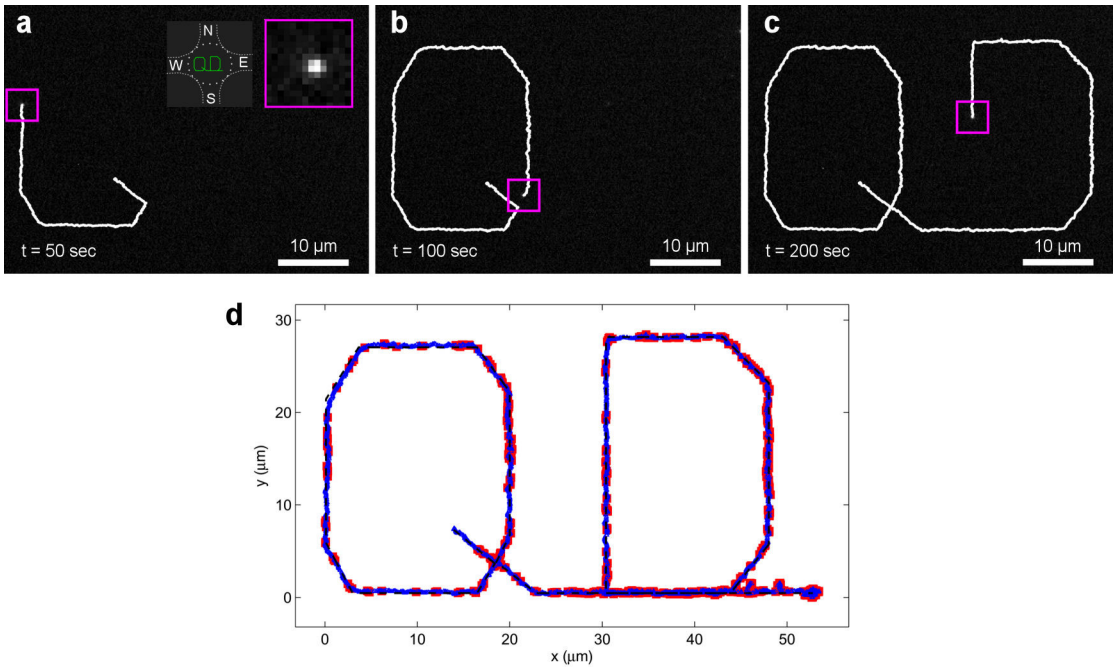

Figure 5: Trajectory of a controlled QD. (a-c) Time-stamped CCD camera images of a single quantum dot being steered along the desired trajectory. The white trace shows the measured path of the quantum dot up until its current location. The square magenta box shows the subpixel averaging window used to determine the current position of the QD. The insets in panel (a) show the orientation of the channel with the trajectory (green) and a close-up of the subpixel averaging window that contains the QD near its center. (d) Plot of QD position along its trajectory. The dotted black line shows the desired trajectory. The measured QD trajectory is shown in blue. The solid red squares denote times when the QD blinks off. At the end of the trajectory the QD is held in place for 2 minutes. The mean displacement from the trajectory is calculated to be 119.5 nm.

shown in red. From analysis of the position data, the average displacement of the QD from the path was found to be 119.5 nm.

To determine the positioning precision of the control method, a single QD was selected and moved to a specified location near the center of the control region. The QD was held in that position by feedback control and monitored for 5 min, after which the control was turned off and the QD was allowed to diffuse for another 5 min. Figure 6a shows the measured positions of the trapped (blue spots) and freely-diffusing (red spots) QD. The accuracy of the centroid algorithm in detecting the particle location was determined independently by taking position measurements on a QD that was immobilized on a glass slide for 5 min. The measured positions of the immobilized QD are plotted in Figure 6a as green spots. From the variance of the green spots, the vision noise was determined to be 18.8 ± 0.9 nm [18.7 ± 1.7 nm] in the x [y] direction. Figure 6b is a histogram of the x positions of the held QD. From a Gaussian fit the standard deviation was found to be 49.3 ± 0.7 nm. A similar calculation gives a standard deviation of 47.0 ± 0.7 nm in the y positions. The measured fluctuation in QD position is due to a combination of the random motion of the particle and vision noise of the imaging system. Subtracting the vision noise from the accuracy of the holding proceedure, the positioning precision of the particle is determined to be 45.5 ± 0.9 nm [43.1 ± 1.0 nm] in the x [y] direction.

2.4 Theoretical limit for positioning accuracy

High positioning precision is enabled by feedback, the continual sensing and correction of the QD's deviation from its desired location. This process is successful

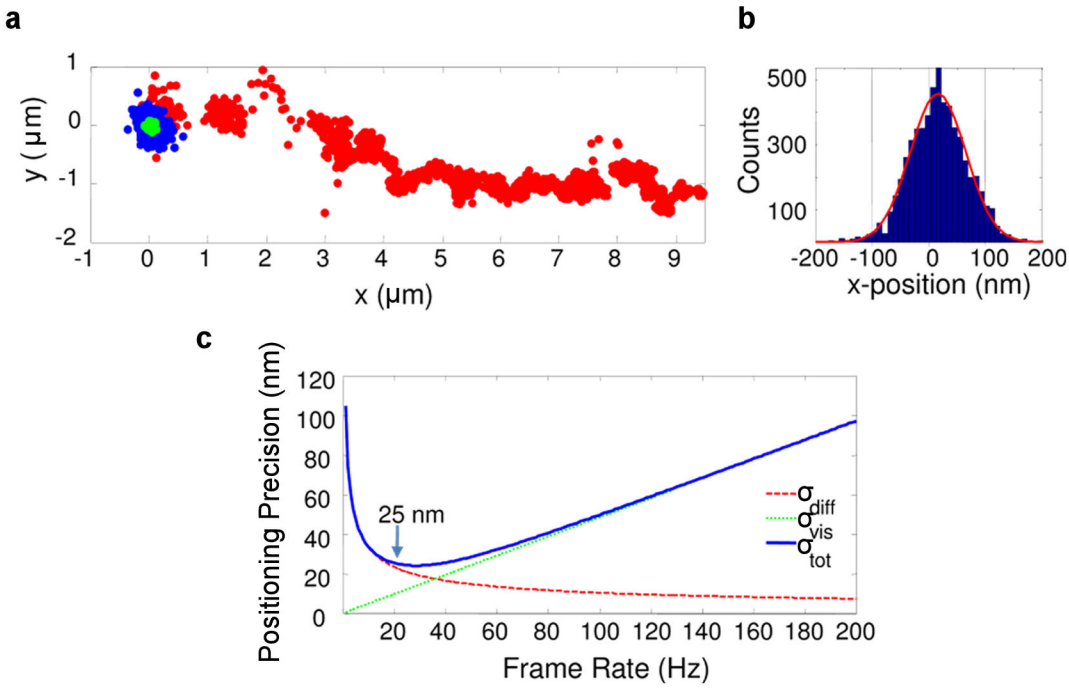

Figure 6: QD positioning accuracy. (a) Blue points represent the measured position of the QD as it is held in place for 5 minutes. The standard deviation along x of the blue points is calculated to be 49.3 nm. The controller is subsequently turned off and the QD is allowed to drift away for another five minutes, as shown by the red points. The drift to the right is caused by a small pressure flow in the device that is continuously compensated when feedback control is on. Measured positions of an immobilized QD are shown in green. From the immobilized QD position uncertainty, we measure the vision accuracy of the setup, which has a standard deviation along x of 18.8 nm. Subtracting the vision noise from our measured variance demonstrates that we are positioning with 45.5 nm precision. (b) Histogram of the measured positions along the x direction for a held QD with a Gaussian fit with standard deviation of 49.3 nm. The center of the Gaussian is slightly to the right of zero, corresponding to the small pressure flow towards the right. (c) Calculated positioning precision due to diffusion (dashed red line), vision noise (dotted green line), and both noise sources combined (solid blue line) as a function of camera frame rate.

even if the flow fields in the device are not known perfectly. So long as the actuation is sufficient to move the QD towards where it should be, the control acts to decrease the position error significantly, quickly driving the QD to its desired location. The resulting positioning accuracy of the control is fundamentally limited by the Brownian motion of the particle between control updates and the accuracy of the vision sensing [64], and is thus given by $\sigma_{total}^2 = \sigma_{diff}^2 + \sigma_{vision}^2$. In this expression, $\sigma_{diff}^2 = 2D/F$ is the noise due to diffusion, where D is the diffusion coefficient and F is the camera frame rate. For a spherical particle of radius a in the limit of low Reynolds' number, the diffusion coefficient is given by the Einstein-Stokes relation $D=k_BT/(6\pi\eta a)$, where k_B is Boltzmann's constant, T is the fluid temperature, and η is the fluid viscosity. The second noise term, σ_{vision}^2, is the camera vision noise, which is primarily due to photon shot noise and camera read noise (background noise was determined to be negligibly small compared to these noise sources) and is given by

$$\sigma_{vision}^2 = \frac{\lambda^2 F}{8R} + \frac{d_{\text{pix}}^2 n_r^2 \sigma_u^2 F^2}{R^2}. \tag{2.1}$$

The first term in the above expression accounts for shot noise, while the second term accounts for read noise (which is assumed to be equal for each pixel). The parameter λ is the emission wavelength of the QD, R is the total photon detection rate integrated over the entire camera image, n_r is the camera read noise, d_{pix} is the distance on the sample represented by the separation between adjacent pixels, and $\sigma_u^2 = N^2(N/2+1)(N+1)/6$ where N is the size of the subpixel averaging window. We note that out of all the noise sources, only σ_{diff}^2 depends on the size of the

particle. This dependence occurs through the diffusion coefficient, which is inversely proportional to the particle radius. Thus, the positioning precision scales inversely with particle radius, in contrast to optical traps, in which it scales inversely with radius cubed [52].

The camera read noise was found to be 6.3 electrons, d_{pix} was found to be 160 nm, and the peak photon detection rate was determined from the CCD image intensity to be R=175 000 s^{-1}. It should be noted that the photon detection rate varied significantly throughout this experiment due to blinking and intensity noise of the QD emitter. The diffusion coefficient was found to be $(5.5 \pm 0.4)\times10^{-15}$ m^2/s by tracking free floating QDs in the microfluidic chamber and performing a maximum likelihood estimate on the data. This measured diffusion coefficient differs significantly from the number that would be calculated by the Stokes-Einstein relation using the particle radius and measured viscosity. This discrepancy is well known and is attributed to the fact that the particle interacts with the nearby liquid to create an effective hydrodynamic diameter that can be much larger than the actual diameter of the particle [71]. We thus use the measured diffusion coefficient in our calculations.

Setting the QD emission wavelength to λ = 655 nm, we plot σ_{diff}, σ_{vision}, and σ_{total} as a function of the camera frame rate in Figure 6c. From the plot one can see that there is a tradeoff between vision noise and Brownian motion. As the frame rate is increased noise, due to Brownian motion is reduced because the particle has less time to diffuse between successive camera frames. However, vision noise increases because fewer photons are collected from the QD. At 20 Hz, the position precision is

25 nm. The optimal position precision of 24 nm is achieved at a frame rate of 28 Hz, which is close to our actual frame rate. The experimental results do not achieve the theoretical positioning limit due to additional noise sources such as mechanical vibration and instability, imperfections in the control algorithms, and frame averaging effects caused by the fact that the QD is moving during the acquisition of a single camera image.

2.5 Characterization of trapping time

To determine the trapping time, we positioned and trapped a second QD for 1 hour

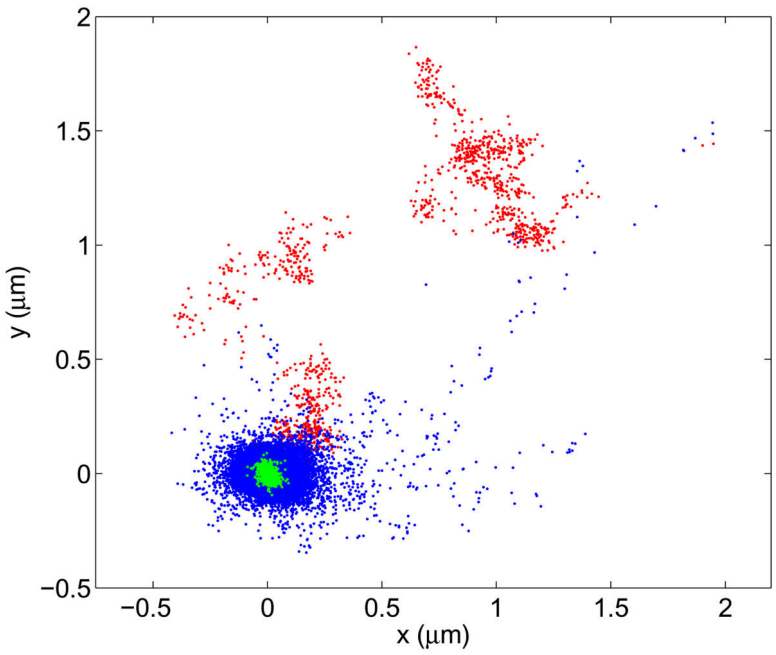

Figure 7: Characterization of positioning accuracy for a long holding time. Plotted is the measured position of a single QD as it is held at a desired location for one hour. The blue points represent the measured position when the controller was on, corresponding to a 52 nm positioning accuracy. The red points represent the position of the QD when the controller is subsequently turned off for five minutes. Green data points are the positions of an adhered QD illustrating the spatial uncertainty due to vision noise.

(Figure 7). From the position data it was found that this QD was held with 51.5 ± 0.8 nm precision. The slight increase in position error was due to the fact that by the end of the 1 h, the QD was emitting much less efficiently and was blinking significantly more (presumably due to oxygen contamination and photobleaching). The increase in blinking served to reduce the position precision because the QD was able to drift for a longer distance before re-emitting. This degradation is due to oxygen contamination and be can be reduced by incorporating oxygen scavenging chemicals in the solution [72]. At no time during the 1 h period were multiple QDs inadvertently trapped by the controller. Such trapping times for single QDs have not been demonstrated using other trapping methods. For comparison, the non-specific trap created by optical tweezers will typically trap multiple QDs on a timescale of 5-10 minutes [36].

2.6 Characterization of photon emission

To ensure that we are controlling a single QD, and to demonstrate that we can characterize the single photon nature of our emitter while simultaneously performing control, we carried out an autocorrelation on a dynamically positioned QD. A 25-75 beam splitter was used to deflect 75% of the light away from the camera and into a Hanbury-Brown-Twiss type autocorrelation setup composed of a 50-50 beamsplitter and two avalanche photodiodes. The remaining 25% was sent onto the CCD camera to position the QD at a fixed location in the microfluidic device. To reduce uncorrelated background counts, we gated the autocorrelation setup to accumulate data only when the QD was not blinked off using the intensity threshold from the CCD camera image. The results of the autocorrelation measurement, which was taken

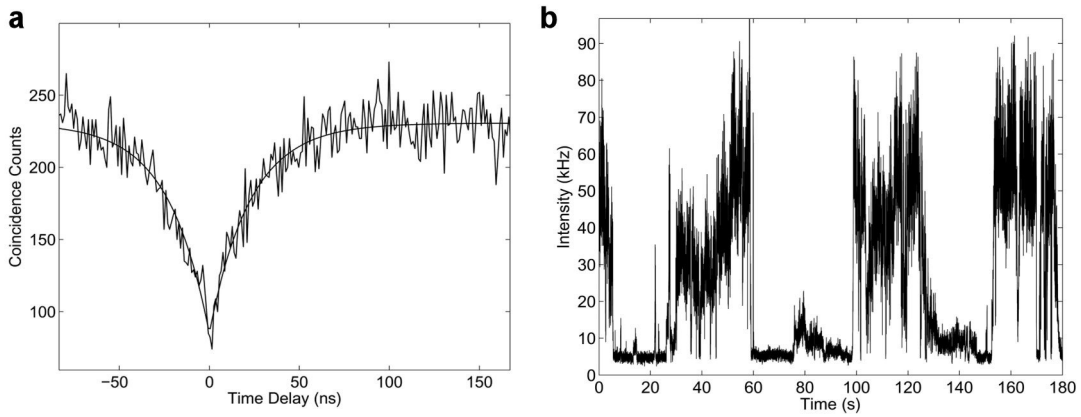

Figure 8: *In-situ* measurements of a single QD. (a) Autocorrelation measurement of a single controlled QD obtained from a 15 minute integration with 1 ns binning and exponential fits shown. From the exponential fit $g^2(0)$ is determined to be 0.37 ± 0.02 and the decay time t_d is determined to be 22.7 ± 1.1 ns. (b) Fluorescence intermittency as measured from a single held QD.

over 15 min, are shown in Figure 8a. The autocorrelation was fit to a function of the form $G^2(\tau) = G_\infty^2[1-(1-g^2(0))e^{-\Gamma\tau}]$, where $\Gamma = \Gamma_s + \Gamma_e$ with Γ_s being the spontaneous emission rate and Γ_e being the excitation rate. In our experiment the excitation power was set to 250 W/cm^2, which is well below saturation [19,73]. In this limit the excitation rate is much smaller that the spontaneous emission rate, so $\Gamma \approx t_s^{-1}$ where t_s is the QD spontaneous emission lifetime. From the data fit we find that $g^2(0) = 0.37 \pm 0.02$, which is a clear signature of anti-bunching, demonstrating that we are indeed controlling a single QD. The fit also yields a QD spontaneous emission time of t_s = (22.7 ± 1.1) ns, which is consistent with previously measured values [19,65,73].

In addition we were able to take an intensity time trace of the blinking behavior from a single QD while it was being held in place. The resulting trace of the blinking intermittency is shown in Figure 8b. The observed blinking behavior is characteristic

of a single QD. These results ensure that we are manipulating single QDs and that we can use them as single photon sources for integration with nanophotonic structures while simultaneously positioning them with flow control.

2.7 Summary

In summary, we have demonstrated the ability to individually select, characterize, and position single nanoscopic objects with nanometric precision. In our current experiments, control can only be achieved in two dimensions for individual QDs. However, recent theoretical work has shown that it is possible to achieve three-dimensional control in two-layer microfluidic devices [74]. It is also possible to extend the control to multiple particles using techniques experimentally demonstrated in Ref. [60]. Our capabilities could enable integration of single QDs, or other visualizable nano-scale objects, with photonic structures and facilitate the development of novel nanophotonic devices and sensors. Additional techniques enabling immobilization of objects via surface chemistry [75] or cross linking polymerization [76] could be further incorporated with the procedure demonstrated here for scalable fabrication of integrated devices that require the precise placement of preselected nanoparticles with desired properties.

Chapter 3: Positioning and immobilizing quantum dots with nanoscale precision

3.1 Introduction

The ability to place nanoscopic objects at precise locations on patterned or prepared surfaces is essential for a broad range of device applications. One important example is the positioning of QDs in nanophotonic structures such as cavities [46–48] and waveguides [77], for applications such as single-photon generation [23,78,79], QD lasers [80], and nonlinear optical devices [81]. Another example is the nanoscale positioning of metallic and dielectric particles on prepared metamaterial surfaces to engineer nanoscopic electronic circuits [51]. The majority of these applications exploit optically resonant interactions that require the nanoscopic particles to have the correct spectral properties. For these applications it is essential to have a technique that can pre-select particles with desired spectral properties and place them at the correct locations on a surface.

In this chapter we demonstrate a broadly-applicable method for the positioning and immobilization of nanoparticles at precise locations on a surface. This method takes advantage of electroosmotic flow control (EOFC), a technique that provides precise, nanoscale positioning of nanoparticles [82]. Previous demonstrations of flow control have achieved manipulation of micron-sized particles with micrometer precision [45,60], random capture of nanoparticles with nanometric holding accuracy [34,58,66], and more recently manipulation of nanoparticles with nanometric precision [82].

3.2 Experimental technique

A major limitation of EOFC to date has been that actuation of individual particles can only be achieved in two dimensions, since fluid flow occurs only along the directions that lie parallel to the fluid channels. Thus, a particle that is being manipulated on the bottom surface of the device is free to diffuse out of plane, making it difficult to place the particle on a pre-patterned surface. Another important limitation is that all particles in the device are subject to flow. Therefore, once a desired particle has been positioned, it is not possible to manipulate a second particle without disturbing the position of the first one.

Here we demonstrate a technique that overcomes both of these difficulties. The specific nanoparticles that we manipulate are colloidal cadmium selenide QDs. Single QDs are generally difficult to manipulate due to their small sizes and sensitivity to their physical environment. To achieve manipulation and immobilization of individual QDs along a surface we have developed a low-viscosity, water-based, negative-tone photoresist that causes QDs to be localized within a thin sheath along the surfaces of a microfluidic channel. When using this photoresist, EOFC of the nanoparticles occurs effectively in two dimensions at the surface of interest. After the QD has been delivered to a desired location by EOFC, a brief exposure to ultraviolet light polymerizes the surrounding fluid to immobilize the QD. Once a selected QD has been immobilized, manipulation of subsequent QDs does not affect its position. This technique makes possible the sequential, high-precision positioning and immobilization of a large number of selected nanoparticles on a 2D surface.

A schematic of the microfluidic device used in our experiments is shown in Figure 9a. The device is composed of a pair of microfluidic channels formed between a glass cover slip and a molded block of PDMS. The control region resides at the intersection of the two channels and has a width of 100 μm and a height of 5 μm. The microfluidic channels are filled with a mixture of QDs (Invitrogen Qtracker PEG CdSe/ZnS 655 nm) suspended in an aqueous photoresist that we have developed. The photoresist is composed of a water-soluble multifunctional acrylic monomer, a radical photoinitiator, and a rheology modifier used to increase fluid viscosity. When exposed to UV light, the photoresist will cross-link in the exposed area to form a small polymerized region that can be used to encapsulate and immobilize a QD. The monomer is added at a concentration near its solubility limit, which causes the QDs to segregate to the surfaces of the device, as shown and discussed in detail in subsequent section. Four electrodes are immersed in the fluid reservoirs, providing the voltages necessary for EOFC [44]. These electrodes can actuate the buffer to flow in any of the four cardinal directions parallel to the glass substrate.

Figure 9b shows a diagram of the experimental setup, which consists of an inverted confocal microscope that images the QDs onto a CCD camera operating at a 10 Hz frame rate. QDs are illuminated with a 532 nm laser at 100 W/cm^2. Individual QDs are tracked in real time by the imaging system. Sub-pixel averaging, based on a centroid estimate, is used to determine the position of a QD to a precision that is much better than the diffraction limit of the optical system [55]. Once the position of a QD is determined, a control algorithm applies voltages to the four electrodes to actuate the correcting electroosmotic flow [45]. The control algorithm applies the

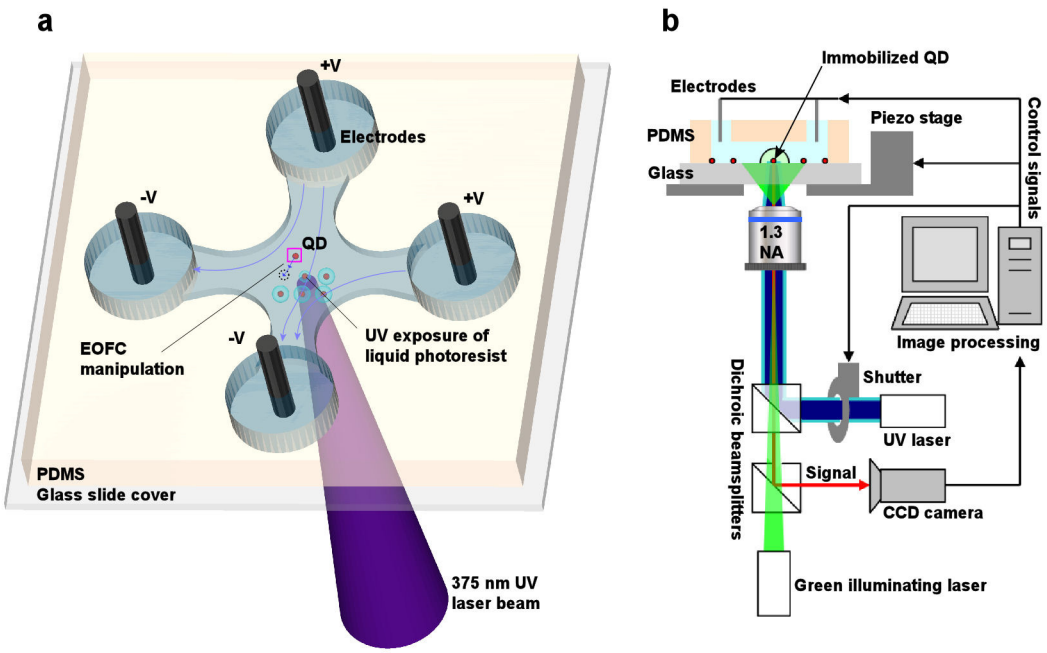

Figure 9. Microfluidic device and setup. (a) The microfluidic device is formed between a glass cover slide and a molded PDMS block. Colloidal CdSe/ZnS QDs are suspended in the photoresist, which is used to fill the channel. Electrodes placed in the four fluid reservoirs provide the voltages necessary to move QDs as desired using EOFC. A UV laser is integrated to expose the photoresist at a central location in the setup. This location can be moved by translating the sample stage. (b) Experimental setup showing a cross section of a microfluidic channel. Dichroic beam splitters are used to integrate the UV source for photoresist exposure and the green source for illumination. Signals from the QDs are filtered and imaged on a CCD camera. Data collected from the camera are analyzed through image processing to determine the location of the QDs. The desired feedback signals are calculated and then sent to the electrodes, the piezo stage, and the UV shutter to coordinate the positioning.

voltages needed to move the QD from its current location towards the target location via a continuous control loop, quickly driving the position error down to a limit set by the imaging accuracy and particle diffusion between control updates [60].

3.3 Fluid chemistry

The photoresist used in our experiments is composed of 0.6 wt% rheology modifier (Acrysol RM-825, Rohm and Haas Co.) [69], 40% by volume ethoxylated-15 trimethylolpropane triacrylate (SR-9035, Sartomer), 0.3 wt% sodium 4-[2-(4-Morpholino)benzoyl- 2 dimethylamino]butylbenzenesulfonate (MBS) photoinitiator [83], and QDs with a molar concentration of 100 pM (Qtracker PEG CdSe/ZnS 655 nm) in deionized water. The monomer and photoinitiator provide the photocrosslinking capability, while the rheology modifier is used to increase the viscosity of the fluid and therefore reduce the Brownian motion of the colloidal QDs. The polymer also notably decreases QD surface binding.

All fluid components mix well with water except the monomer at this proportion. When the monomer is mixed an emulsion is formed that includes globules of fluid containing the colloidal QDs. These globules can be seen filling the microfluidic channel and adsorbing to the surfaces within the devices. The resulting films of QDs in water still exhibit good EOFC and the QDs within these films do not show significant signs of surface binding or agglomeration. Figure 10 shows images of the filled microfluidic channel at different heights with (Figure 10a-c) and without (Figure 10d-f) the monomer added to the fluid. When the monomer is added the QDs are found to be dispersed only at the top PDMS surface (Figure 10a) and bottom glass surface (Figure 10c) of the devices. A large QD-containing globule can be seen in focus only in the middle of the cross channel (red in panel b). Figure 10b also distinctly shows QDs forming a thin film along the channel walls (blue), indicating

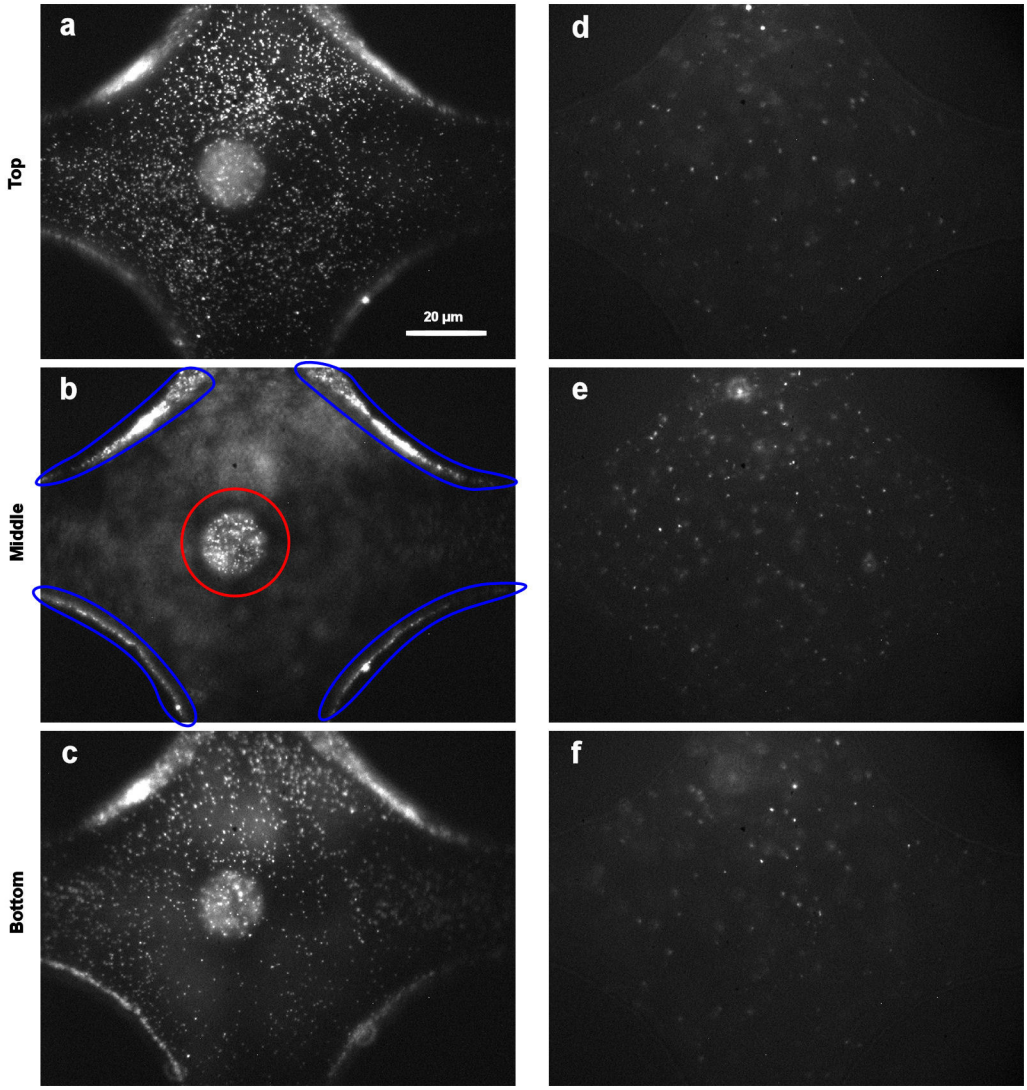

Figure 10. Optical images showing QD films along surfaces. (a-c) Microfluidic channel filled with rheology modifier and the immiscible monomer (0.6% RM-825 and 40% SR-9035) shown at different planes within the device. QDs in focus at both the top (PDMS) and bottom (glass) surfaces can be seen along with a large globule (red) and thin layers of QDs along the channel walls (blue) in the middle of the channel. (d-f) Microfluidic channel filled without the monomer (0.6% RM-825) at the same planes within the device. QDs are dispersed uniformly vertically throughout the device.

that the QDs are coating all surfaces. These results can be compared to Figures 10d-f, which correspond to the situation in which there is no monomer. In this latter case,

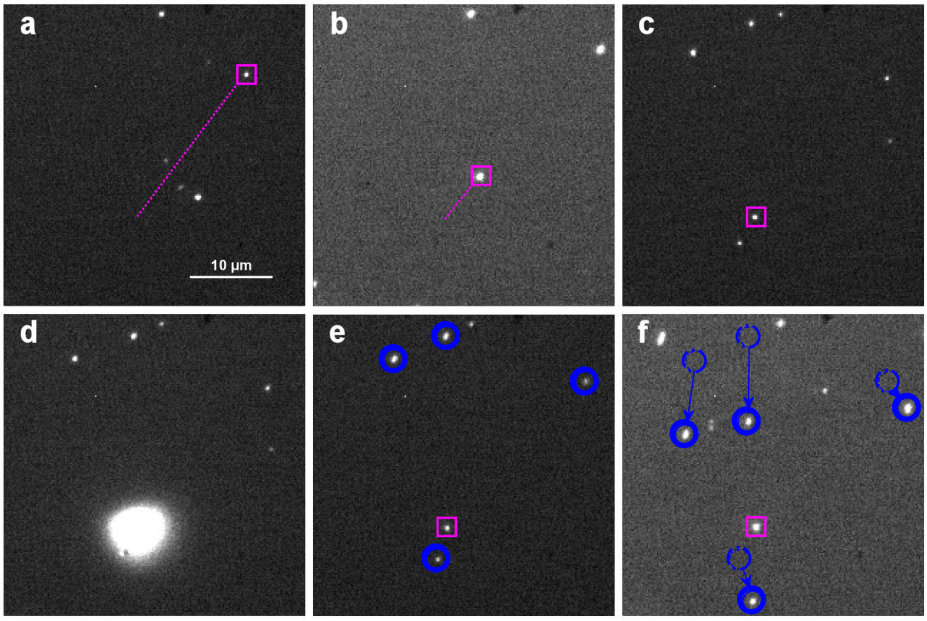

Figure 11. Positioning and immobilization of a single QD. (a-c) A single QD is chosen (magenta box) and moved towards the target location. The line shows the distance between the QD and the target. (d) Image showing the local UV exposure aligned with the target location used to immobilize the QD once it is in place. (e-f) After the QD is encapsulated (magenta box) it does not move with an applied voltage to the top electrode, although the QDs in the surrounding solution do move. Several other QDs are circled in blue in panel (e) and their displacements after one second of flow are shown in panel (f).

the QDs are equally dispersed throughout the microfluidic channel, as evidenced by the fact that the number of in-focus QDs is the same at each focal plane.

3.4 Positioning and immobilization of single QDs

Figure 11 shows how QDs that have been pushed to the surfaces of the device can be manipulated along the surface by electroosmotic actuation. The chosen QD is selected by our control software and moved towards the specified location, as shown in Figures 11a-c. We observe a strong blinking behavior, which is evidence that we are indeed manipulating single QDs (definitive proof that we are manipulating single

QDs is obtained by performing photon anti-bunching measurements, as discussed in the section of this chapter on system characterization). The control algorithm performs actuation only when the QD is in the luminescent state, as determined by a threshold value for its observed intensity. Once the QD is at the target position, the area containing the QD is irradiated by a 375 nm laser beam that is centered on the target position to achieve local crosslinking of the photoresist. The UV laser is focused to a spot size of 2 μm with an intensity of 500 W/cm^2. A shutter is trigged automatically to expose with UV light for 400 ms (Figure 11d) once the QD is determined to be within 80 nm of the target position. Figures 11e and 11f show successive camera frames obtained after the QD was immobilized. In this particular example, a voltage was applied on the top electrode to create electroosmotic actuation in the South direction. As can be seen from these two frames, the immobilized QD remains at the same position while the surrounding QDs move with the flow.

3.5 Complex assembly of multiple QDs

The ability to position and immobilize nanoparticles opens up the possibility for assembling complex patterns of pre-selected QDs. As an example, we created a 3 × 3 square lattice array of QDs with 5 μm separation between adjacent lattice sites. A single QD was first positioned and immobilized at a desired location near the center of the control area. A piezo stage was then used to move the sample to the next location in the array, where a QD was subsequently positioned. Figure 12a shows the resulting 3 × 3 array. This image is an average of 4 consecutive frames, each with a 500 ms exposure time, and is displayed on an intensity-log scale. The leftmost QD in

the middle row emitted less brightly than the others during this exposure period, and so appears dimmer in the image. The entire array was monitored over a period of 15 seconds and subpixel averaging was used to measure the position of every QD during frames in which they were in the luminescent state (Figure 12b). Figure 12c shows a zoomed-in plot of the measured positions for one of the QDs. These measured positions are all well localized. We note that there is a slight asymmetry between the variance in the x and y directions of the measured positions. This asymmetry is attributed to a small drift of the piezo stage over the measurement time.

Positions for each of the nine QDs were determined by averaging over each data set. We determined the vision accuracy of the subpixel averaging, based on the standard deviation of measured positions for each QD, to be 14 nm (8 nm) in the x (y) directions. To obtain a measure of the relative in-plane positioning precision for QD

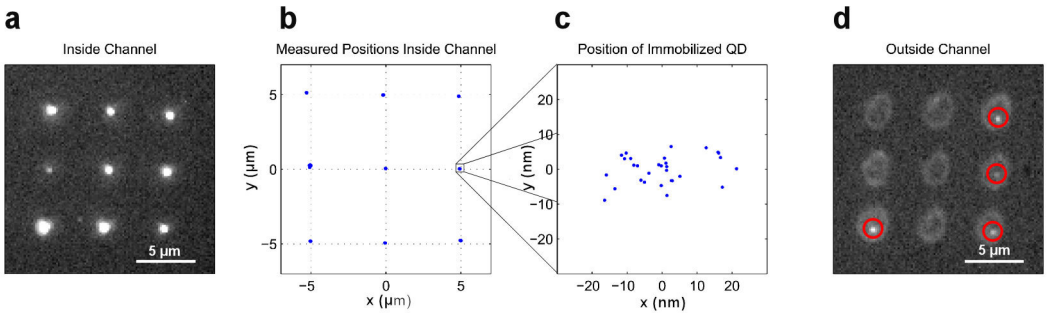

Figure 12. Positioning and immobilization of a single QD. (a-c) A single QD is chosen (magenta box) and moved towards the target location. The line shows the distance between the QD and the target. (d) Image showing the local UV exposure aligned with the target location used to immobilize the QD once it is in place. (e-f) After the QD is encapsulated (magenta box) it does not move with an applied voltage to the South electrode, although the QDs in the surrounding solution do move. Several other QDs are circled in blue (e) and their displacements after one second of flow are shown in panel (f).

immobilization, we fit our data to an ideal 5 μm grid by translating and rotating the data and optimizing the average distance between the two. When optimized, the average error in distance was measured to be 127 nm, which is our precision in reproducing the array on the surface.

A single image of the encapsulated QDs after channel removal is shown in Figure 12d on an intensity-log scale. All of the polymerized regions remained adhered to the slide surface, and several of the QDs (shown circled in red) can be seen clearly emitting at the correct locations even after channel removal. The remaining QDs were in a dark state during this particular frame. At other camera frames, these QDs became luminescent while some of the other QDs became dark. The data in Figure 12 demonstrate that devices can be assembled in a fluidic environment and then used once the channels have been removed. We note that a degradation in emission brightness of the QDs is observed after channel removal. The cause of this emission degradation is not fully understood, but it may be due to oxidation during assembly and cleaning. Methods for reducing this contamination using oxygen scavengers have been investigated previously, and could serve to reduce QD degradation [72]. We also note that the polymerized regions shown in Figure 12c are on the order of 2-3 μm in diameter. Such large polymerized regions are not suitable for applications requiring close packing of many nanoscopic particles. These spot sizes could be reduced with improved focusing of the UV beam, and could potentially be made much smaller (sub 100 nm diameter) using multiphoton absorption polymerization [84,85].

3.6 Assembly with two QD species

To demonstrate that this positioning technique can deliver a QD to a marked location on a surface, we deposited a low concentration of a different species of QDs emitting at an average wavelength of 705 nm (Invitrogen Qtracker PEG CdSe/ZnS 705 nm) onto a dry slide cover. These QDs, which remain adhered to the glass surface after filling the channels, served as targets. The channels were filled with the same 655 nm emitting QDs used in previous experiments. The two species of QDs can be distinguished visually by using bandpass filters centered at 655 nm and 710 nm, respectively, in front of the imaging camera. We measured the emission spectra of the two types of QDs using a grating spectrometer (Acton SP 2758 with a resolution of 0.06 nm). Figure 13a shows the measured emission spectra of bulk samples of both

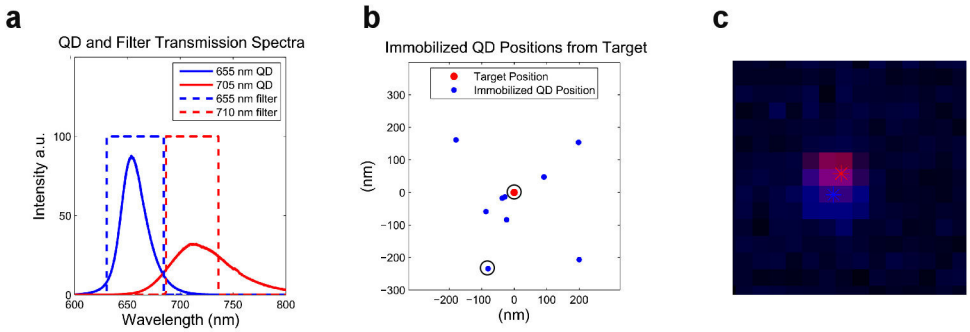

Figure 13. Immobilization of individual QDs to target QDs adhered to the substrate. (a) Spectra of the two different types of QDs and the bandpass transmission spectra of the two filters used to distinguish between them. (b) Relative positions of the nine positioned and immobilized QDs that emit at 655 nm (blue dots) versus their 705 nm targets (all marked by a single red dot at the origin). The average distance between an immobilized QD and its target QD was measured to be 155 nm. The two circles denote the sample QD pair whose pixilated images are overlaid in panel (c), here the red and blue asterisk mark the location of the diffraction pattern centroids inferred by the sub-pixel averaging algorithm.

types of QDs. Additionally, overlaid in Figure 13a are the transmission spectra of the bandpass filters, demonstrating that they can be used for selective visualization of the two different types of QDs.

Individual 705-nm-emitting QDs served as stationary targets for the positioning and immobilization of 655 nm emitting QDs. Target QDs whose emission does not bleed through the 655 nm filter were chosen so that the tracker would not get confused between the two QD types while performing the positioning. Nine 655 nm QDs were immobilized on top of nine chosen 705 nm QD targets, and the positions of all of them were then measured using subpixel averaging. In Figure 13b, the red dot at the origin marks the 705-nm QD target position for all nine pairs and the blue dots show the measured relative displacements of the nine placed and immobilized 655 nm QDs. The average distance between an immobilized QD and its target was calculated to be 155 nm. An overlapped diffraction image of one of the immobilized 655 nm QDs (blue) versus its 705 nm target QD (red) is shown in Figure 13c, with an asterisk labeling their inferred centroid positions.

A unique feature of our positioning and immobilization technique is that it enables us to characterize QDs before they are immobilized. Thus, QDs with desired spectral properties can be pre-selected and delivered to specific locations on a device. As a demonstration of this capability, we fabricated a 3 × 3 array of QDs with different specified colors at each point (Figure 14a). To construct this complex structure, we injected a mixture of both the 655-nm-emitting and the 705-nm-emitting QDs. By alternating between filters after each immobilization step, we assembled a 3 × 3 array of color-selected QDs in a checkerboard pattern.

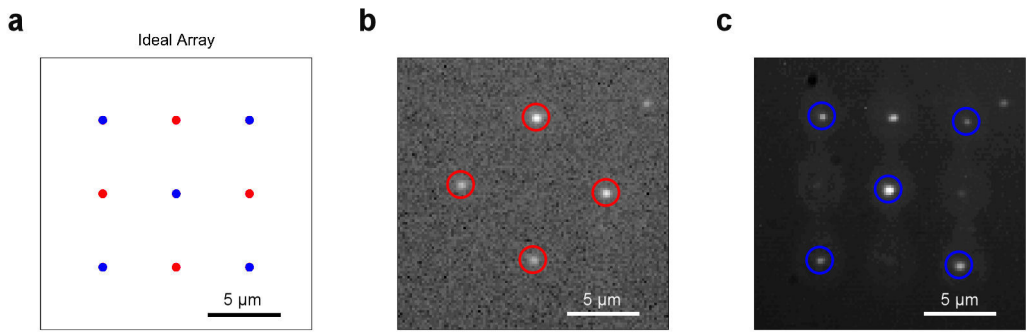

Figure 14. Array of preselected QDs. (a) Idealized array design with the two different types of QDs alternating in a checkerboard pattern. (b) Completed array as visualized through a bandpass filter centered at 710 nm. The four QDs emitting at ~705 nm are circled in red while the 655 nm emitting QDs are not visible. (c) The same completed array as visualized through the 655 nm band pass filter. The QDs emitting at 655 nm are circled in blue.

Figures 14b and 14c show the final assembled array as seen through the 710 nm filter and the 655 nm filter, respectively. The picture in Figure 14b was acquired in one image frame with a 500 ms exposure time. The picture in Figure 14c was acquired from an average of many minutes of frames with 500 ms exposure times each so that we could visualize all five of the QDs, which were never in the luminescent state simultaneously. The QDs that are expected to be seen based on the filter used are circled in each picture. With the 710 nm filter in place only the correct QDs are visible. However, the top-middle QD from the 705 nm batch is clearly visible through the 655 nm filter (Figure 14c), due to the fact that the 705 nm QDs have more inhomogeneous spectral broadening than do the 655 nm QDs (as seen in the spectra in Figure 13a). Therefore, a QD from the 705 nm sample is more likely to overlap partially with the passband of the 655 nm filter.

3.7 System characterization

Subpixel averaging

Achievement of nanometeric positioning and immobilization of single nanoparticles using our microscope setup requires us to be able to extract subwavelength-of-light information from an optical signal. To attain this goal we employ subpixel averaging, which requires that the diffraction spot of the imaged particle be spread out over several pixels on the imaging CCD. A center-of-mass of calculation of the image will measure the position of the particle at the center of its diffraction spot. The accuracy of this technique is fundamentally limited by the signal-to-noise ratio of the particle compared to the read and shot noise of the camera. However, the measurement accuracy gets better as this position is averaged over many frames. With this technique we are able to measure nanoscopic changes in position. To demonstrate the power of this technique, a single QD stuck on a slide cover was moved in increments of 24 nm using a piezo actuator while its position was measured continuously via our centroiding algorithm. The data are shown in Figure 15a. The incremental steps of 24 nm can be seen above the noise from the raw data (black), but the steps are especially visible when the positions are averaged over time (red). The measured average positions and the actual positions imparted by the piezo are displayed in Figure 15b, and show very good agreement. Therefore, we are able to perform position measurements on immobilized QDs with high accuracy despite being limited to diffraction spot information from our nanoparticles.

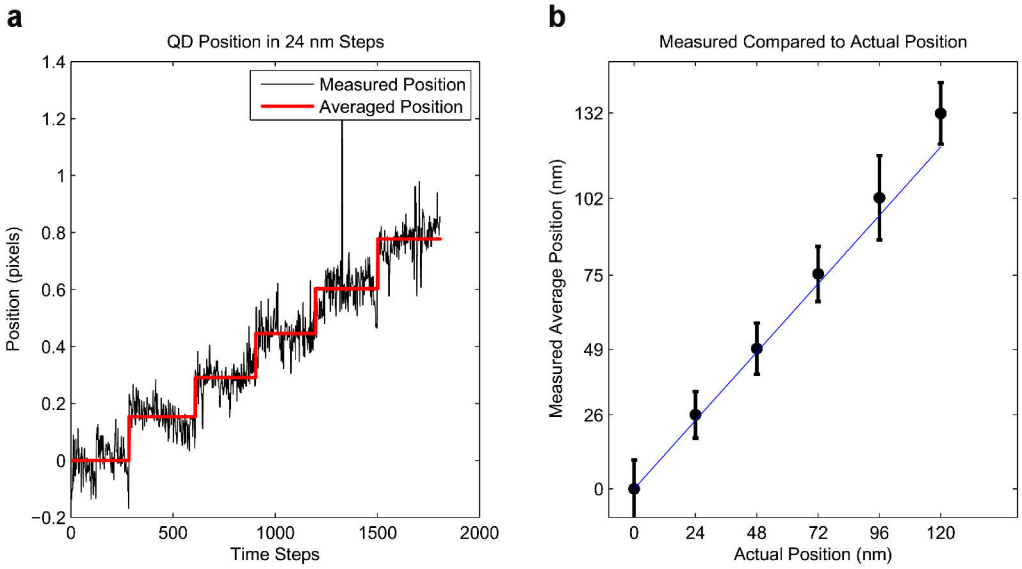

Figure 15. Measured position of a QD as the piezo stage was moved in 24 nm increments (a) Measured data showing the subpixel accuracy of our centroiding algorithm. The black data are the measured pixel position of the QD, while the red line is the average position for each step. Discrete steps are seen clearly in the measured data. (b) Measured average position (from panel a) showing the mean and standard deviation compared to the actual position imparted by the piezo stage when converted into actual length units. The blue line denotes when the measured position equals the actual position. In general the measurement has high accuracy and can easily distinguish changes in piezo displacement.

Single QD characterization

To ensure that we are controlling and immobilizing single QDs, a 2 × 2 array of QDs was assembled (Figure 16a) and an autocorrelation measurement was performed on the encapsulated QDs while they were still inside the microfluidic channel. An aperture was closed down around the beam for spatial filtering of the QD signal, which was then diverted into a Hanbury-Brown-Twiss type autocorrelation setup consisting of a 50:50 beam splitter and two avalanche photodiodes set to count coincidence photons. The photodiodes were also gated so as not to accumulate counts

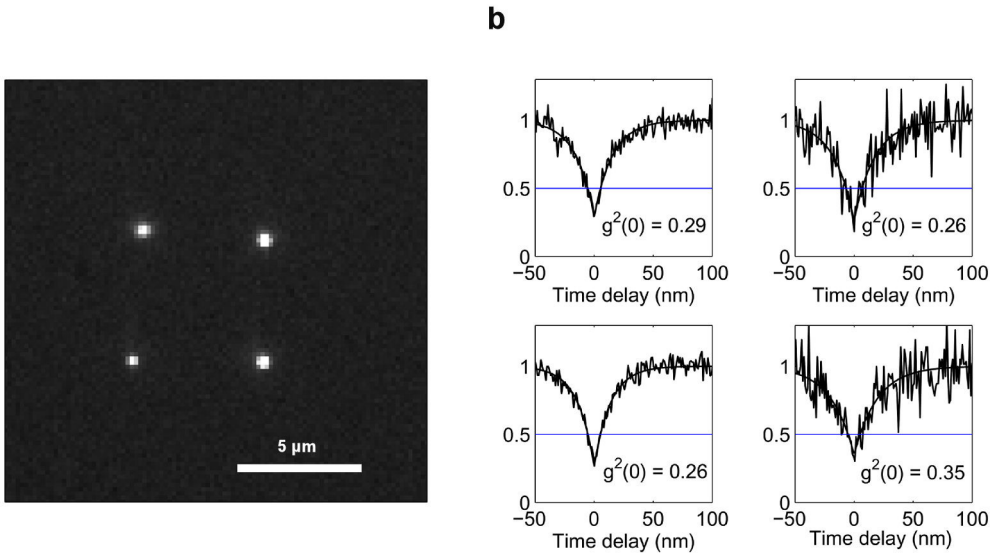

Figure 16. Array of immobilized dots and their measured $g^2(\tau)$s. (a) Image of the 2 × 2 array of QDs spaced 5 μm apart. (b) The corresponding $g^2(\tau)$ measurements for each of the four respective QDs. Autocorrelations are taken over a 1 minute integration time while the QDs are still in the channel. The measured $g^2(0)$s are 0.29, 0.26, 0.26, and 0.35 and all show signs of the photon antibunching that is characteristic to quantum emitters.

when the QD is in a dark state. Correlations were obtained over a one minute integration time. For these measurements, our pumping power was well below saturation. The normalized cumulative counts could be fit to a function of the form $g^2(\tau) = [1 - (1 - g^2(0))e^{-\Gamma_s \tau}]$, where Γ_s is the spontaneous emission rate of the QD. The resulting $g^2(\tau)$ measurements for each of the four immobilized QDs are shown in Figure 16b. The measured $g^2(0)$s were found to be 0.29, 0.26, 0.26, and 0.35. All $g^2(0)$s are well below 0.50, indicating that we are positioning only single photon emitters.

Proximity to surface

To measure the distance of the immobilized QDs from the surface, we exploited the fact that a small fraction of QDs adhere to the surface naturally in the course of an

experiment. These adhered QDs serve as reference points that enable us to determine the position of the glass surface. We positioned and immobilized three QDs in a 20 × 20 μm area that contained three naturally adhered QDs. This small region was used to minimize systematic errors in depth measurements due to non-uniformity of the surface and to spherical aberrations in the microscope. The distance between the objective lens and the surface was then varied by moving the piezo stage in and out of focus in steps of 200 nm. Both the immobilized and naturally adhered QDs were imaged for many frames at each stage position and the sizes of the diffraction spots were tabulated using the variances of the QD image. For every QD, a median diffraction spot size was calculated at each position and the data were fit to a beam divergence function of the form [86]

$$w(z) = w_0\sqrt{1+\left(\frac{z-z_0}{z_R}\right)^2}\ , \tag{3.1}$$

where w represents the width of the diffraction spot as a function of focus position z. The minimal diffraction spot size denoted by w_0 is located at the vertical position z_0. The Rayleigh range of the diverging spot is z_R. A plot of the diffraction spot size, in pixels, of one of the encapsulated QDs as a function of focal depth is shown in Figure 17a. The fit was used to determine the location of the minimal diffraction spot (and hence the in-focus z position of the QD) from the fitting parameter z_0. This procedure was carried out for the remainder of the QDs, and the results are shown in Figure 17b. The vertical positions of the naturally adhered QDs are shown in black and those of the immobilized QDs are shown in red. We denote the average position of the naturally adhered QDs as z = 0, the location of the glass surface. The position of this

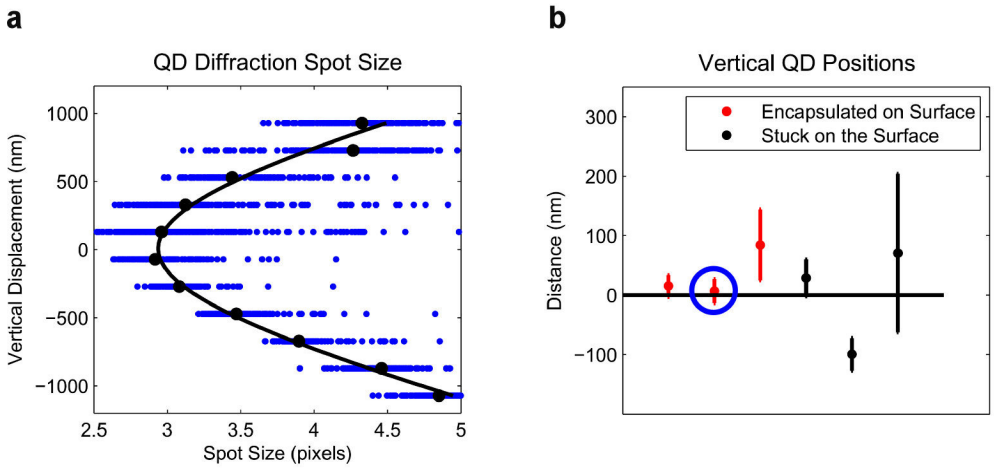

Figure 17. Proximity of QDs to the surface. (a) Graph of the diffraction spot size of an encapsulated QD at varied focal distances from the surface. At each position the diffraction spot size was measured many times (blue data points) and a median size (black points) was calculated. A fit was used to find the location of the minimum spot size (black line), establishing the vertical position of the QD. (b) Measured in-focus vertical positions of three encapsulated QDs (red) and three QDs adhered to the surface (black) with corresponding error bars. The blue circle denotes the data point corresponding to measurements shown in panel a.

surface was determined with a standard deviation of 80 nm. The average position of the three encapsulated QDs is given by 35 ± 38 nm. The uncertainty in the vertical measurements of both the adhered and encapsulated QDs is likely caused by vision noise in our imaging setup, QD blinking, and the inherent roughness of the slide cover. The accuracy of the measurement could be improved significantly by using better methods for measuring the out-of-plane position of the QDs based on cylindrical lenses [87] or a double-helix point-spread function [88].

3.8 Summary

In summary we have demonstrated a method for positioning and immobilization of pre-selected nanoparticles along a two dimensional surface. These results were

achieved by combining high precision tracking and feedback control with the development of a water-based photoresist that restricts QDs to a thin sheath near the surface of a microfluidic channel. Here we have demonstrated the positioning of colloidal QDs, but the technique is general and can be employed with any nanoscopic particle that can be visualized. It is also potentially amenable to use with virtually any substrate that is compatible with water. This technique is a powerful new approach for the precision, high-yield assembly of complex nanophotonic and plasmonic devices that can combine synthesized nanostructures and substrates created by nanolithographic techniques, thereby combining the advantages of bottom-up and top-down nanofabrication.

Chapter 4: Assembling complex nanostructures using flow control

4.1 Introduction

Assembling nanoparticles on chip is a critical challenge in nanoscience research. Stochastic assembly approaches that utilize random deposition are effective at creating small-scale devices with a few interacting particles [15,89,90]. But when fabricating more complex devices these approaches suffer from very low device yield. To overcome this limitation, new methods for deterministic assembly are required to place particles at desired locations on-demand.

Here we present a deterministic approach for assembly of complex nanostructures in a microfluidic device using flow control. We develop a versatile toolbox for positioning, orienting, and immobilizing various nanoparticles with nanoscale accuracy. We use obstructions as levers to rotate and orient nanowires with high precision. These obstructions can further be used to separate and combine multiple nano-objects, a task that is difficult to achieve using flow control alone. Once a particle is positioned and oriented, it is immobilized using a fluid that is crosslinked under UV illumination. We use these tools to assemble silver nanowires into complex nanostructures, demonstrating the scalability of the approach. These tools can manipulate a variety of nanoparticles with different sizes, compositions, and geometries for an all-in-one approach to nano-assembly.

4.2 Experimental setup for microfluidic control

We performed all measurements using an inverted microscope system. Our microscope consists of a sample stage with a 1.45 NA oil-immersion objective. The

objective both focuses light to illuminate particles in the control chamber and collects their image. The control chamber is approximately 100 μm in diameter and 5 μm tall. Our microscope employs both fluorescence and white light scattering for imaging quantum dots and plasmonic nanoparticles, respectively. We perform fluorescence imaging using a 250 W/cm^2 green (532 nm) pump laser and white light imaging with a broadband halogen lamp. An EMCCD camera captures images of particles at 10 Hz frame rate. These images are sent to a computer that implements the particle tracking and feedback algorithm in real-time.

4.3 Fluid chemistry

The fluid used in this chapter is composed of 40-52.5% by volume monomer resin, 1.31-0.83 wt% rheology modifier, 0.5 wt% MBS, and 0.15-0.30 wt% EDAB. This chemistry enables localization of suspended particles along the surface of the channel, as well as immobilization using a UV exposure to cause local fluid polymerization [91]. Higher concentrations of rheology modifier and monomer are used to increase fluid viscosity for improved positioning of small nanoparticles, such as QDs and nanorods. Experiments positioning QDs also used a lower concentration of EDAB, which can increase unwanted photo-bleaching. MBS was only added for experiments requiring fluid polymerization.

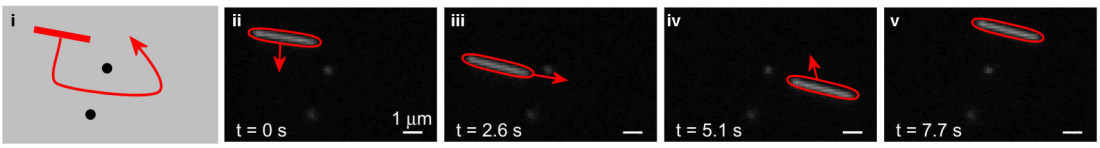

Figure 18: Illustration of nanowire positioning through two obstacles. {ii-v} Time-stamped images. In all figures arrows denote direction of fluid flow.

4.4 Positioning nanoparticles with flow control

Figure 18 shows a serious of optical images in which we demonstrate manipulation of a silver nanowire. We demonstrate controlled positioning by moving this particle through two objects stuck to the sample surface. All objects are in focus in the same plane, signifying that the suspended wire moves along the channel surface. We determine the positioning precision by holding a silver nanowire in place and continuously monitoring its position. Figure 19a shows a scatter plot of the held wire positions, which are rotated so that the x (y) coordinate correspond to the direction perpendicular (parallel) to the wire axis. Panels b and c show histograms of the positions for each coordinate. The standard deviation in the held position is $\sigma_{hp} = 6$ (4) nm in the directions perpendicular (parallel) to the wire axis. We also performed the same measurement using a nanowire that was adhered to the surface to determine the accuracy of the tracking algorithm. We determined the uncertainty in tracking the wire position, $\sigma_{tp} = 3$ (2) nm in the perpendicular (parallel) directions. The positioning precision is calculated by subtracting tracking uncertainty from the held

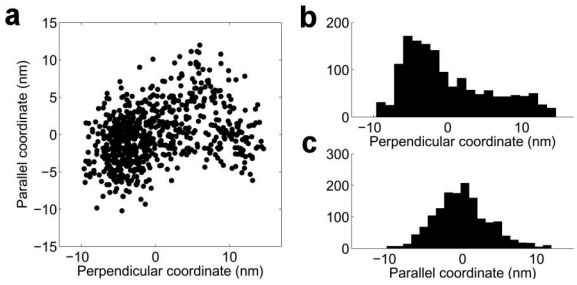

Figure 19: (a) Scatter plot of the measured centroid location of a nanowire held in place by flow control. (b-c) Histograms of the measured positions in the direction perpendicular and parallel to the wire axis.

position accuracy using $\sigma_p = \sqrt{\sigma_{hp}^2 - \sigma_{tp}^2}$, which yields $\sigma_p = 5$ (3) nm perpendicular (parallel) to the wire.

4.5 Rotating and orienting nanoparticles with pivots

In addition to positioning, we need to be able to orient nanoparticles. Optical [92] and magnetic [93] fields can be used to rotate objects to a desired orientation, but these techniques require materials be polarizable or magnetic, respectively. Flow control can rotate nano-objects independently of their material properties, which has been

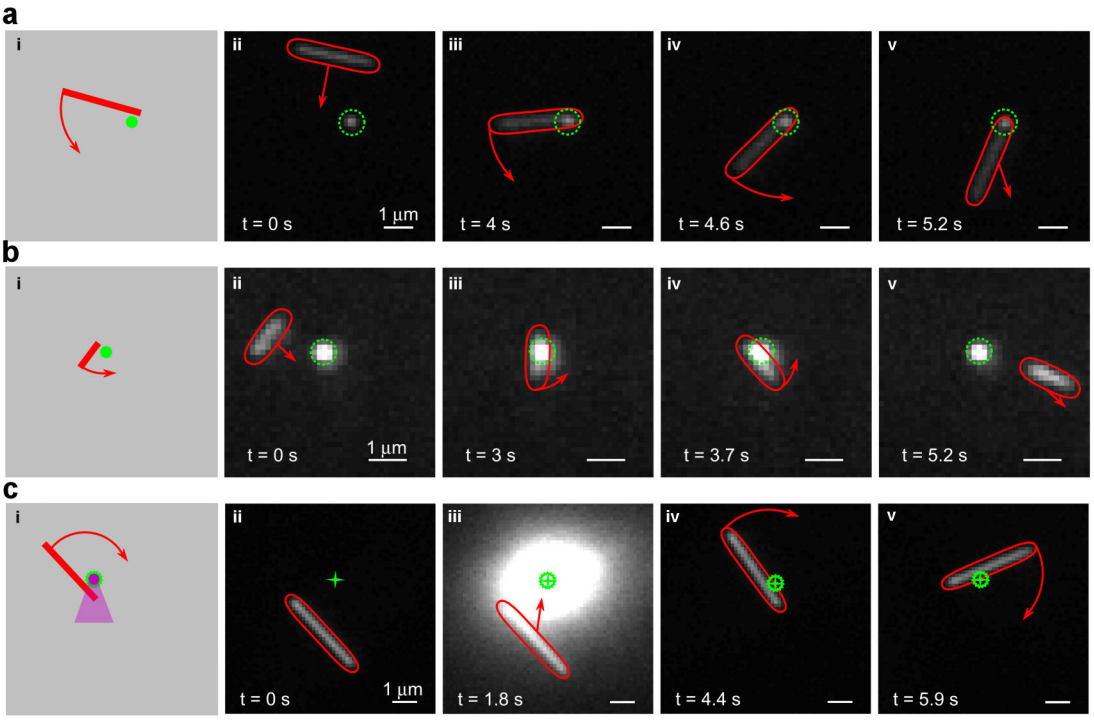

Figure 20: (a){i} Illustration of nanowire rotation using a nanoparticle pivot. {ii-v} Time-stamped images. (b){i} Illustration of nanorod rotation using a nanoparticle pivot. {ii-v} Time-stamped images. (c){i} Illustration of nanowire rotation using a polymerized obstacle, created by UV-exposure (purple). {ii-v} Time-stamped images. Green crosshairs denote the aligned location of the UV laser. In all figures, arrows denote direction of object translation and rotation and green circles indicate location of pivot obstacle

shown previously using fluid shear flows [94,95]. Here we demonstrate a fluidic method to rotate objects using obstacle pivots, which takes advantage of the planar geometry created by our fluid chemistry.

We control the orientation of an object by bringing it in contact with an immobile obstacle on the surface. Obstacle particles are deposited onto the channel surface prior to filling with fluid. These obstacles serve as pivots for torquing the manipulated particles. Figure 20 shows a sequence of optical image frames demonstrating rotation of a silver nanowire using an obstacle pivot, along with an illustration of the rotation concept. The nanowire is positioned so one end comes in contact with the obstacle and flow is applied perpendicular to the wire to apply torque. In row a, a silver nanowire (3 μm) rotates about a silver nanoparticle pivot (indicated by dashed circle). Row b shows rotation of a 1 μm long gold nanorod about a similar pivot. We can also

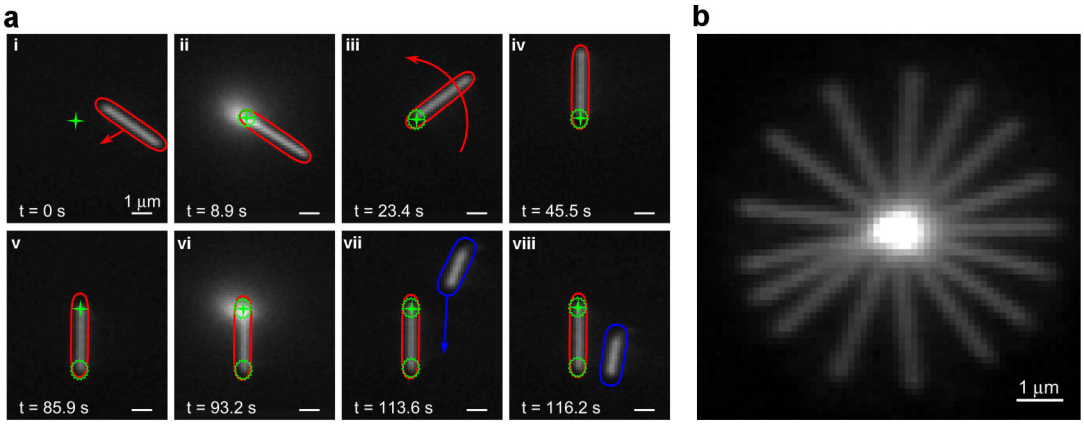

Figure 21: (a) Orienting a nanowire by immobilizing one end. {i-ii} The wire is positioned by flow control, where a local UV immobilizes one end of the wire. {iii-iv} The wire is then rotated about this pivot point and held at vertical orientation. {v} The stage is translated so the UV is aligned to the second end. {vi} A second UV exposure immobilizes the second end. {vii-viii} Another wire is positioned with flow control (in blue) to show that the first wire is immobilized. (b) Composite image from several frames of a wire rotating 360° about its immobilized end.

create pivots as needed with UV polymerization, as shown in panel row c. Here, we first create a pivot using a 1.5 second exposure of a 375 nm UV laser (25 W/cm^2) focused to a target location (shown by the green crosshairs). The laser creates a polymer capsule on the surface that is invisible to the camera (panels iv-v). When we bring the nanowire end to the polymerized region, it rotates along the fabricated pivot as shown in frames iii and iv. These polymer pivots can be created anywhere within the channel to aid object manipulation.

We can also orient nanowires by partially immobilizing one of the ends. Figure 21a is a sequence of camera images that show how the process works. First, we translate one wire end to the aligned UV location indicated by the green crosshair. We then expose this end to a short (0.5 seconds) UV exposure (intensity of 90 mW/cm^2) that loosely affixes it to the surface by partially solidifying the surrounding fluid. This affixed end acts as a pivot about which the wire rotates. A subsequent UV exposure at the second wire end permanently immobilizes the wire in place. An immobilized end enables full 360° rotation of a wire. This is shown in panel b which is a composite of 16 images illustrating full circle rotation.

Affixing one end to the surface provides very accurate control of a wire's orientation. Once tacked down, flow control actuates fluid motion perpendicular to the wire's axis in order to rotate it to a desired angle. Feedback control continually adjusts to compensate for deviations in wire orientation due to rotational Brownian motion. We quantify orientation precision by monitoring the angle of a wire held by flow control for 1 minute. The wire's angle is measured by least squares fitting of the image to a line [95]. Figure 22b plots histograms of the measured angles for the held wire (blue)

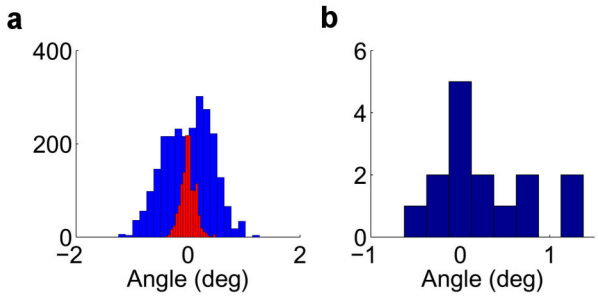

Figure 22: (a) Histograms comparing the measured centroid location of a nanowire that is immobile on a surface (red) with one that is held to an angle by flow control (blue) (b) Histogram of the measured difference in angle from the desired orientation for 15 wires that were fully immobilized.

compared to the measured angle for an immobile wire (red). We calculate the standard deviation in held angle, $\sigma_{h\theta} = 0.42°$. The standard deviation of the immobilized wire's angle provides an estimate for the uncertainty in tracking the wire's angle, determined to be $\sigma_{t\theta} = 0.13°$. We subtract the tracking uncertainty from the held angle accuracy to get the orientation accuracy given by $\sigma_\theta = \sqrt{\sigma_{h\theta}^2 - \sigma_{t\theta}^2}$ and calculated to be 0.40°.

To measure the precision within which we can fully orient and immobilize a nanowire, we repeated the full procedure illustrated in Figure 21 for 15 wires. For each wire we immobilized one end, rotated the wire to vertical orientation, and immobilized the second end. We measured the final orientation of all 15 trials and calculated the differences in angle from the vertical orientation. Figure 22b shows a histogram of these measured differences, which have a standard deviation of 0.53°. This standard deviation is close to the measured value of our orientation precision,

which suggest that the precision with which we can immobilize a wire is limited by how well we can control its orientation. The immobilization process contributes only a small additional error.

4.6 Manipulating nanoparticles with barriers and guides

Immobilized nanowires and nanorods act as obstacles that can improve the positioning of other nanoparticles. Due to their one-dimensional nature, these obstacles act as barriers and guides for separating, combining, and orienting other mobile particles. Figure 23 shows how a nanowire obstacles can be used to separate and combine nanoparticles. For this experiment, we used cadmium selenide QDs, which are suspended in the fluid for positioning. Prior to filling with fluid, we dried a solution of silver nanowires onto the channel surface. These wires acted as the obstacles for the QDs. The wires and dots are imaged simultaneously using a combination of white light scattering and fluorescence imaging. Figure 23a shows two QDs being separated using an immobilized silver nanowire as a barrier

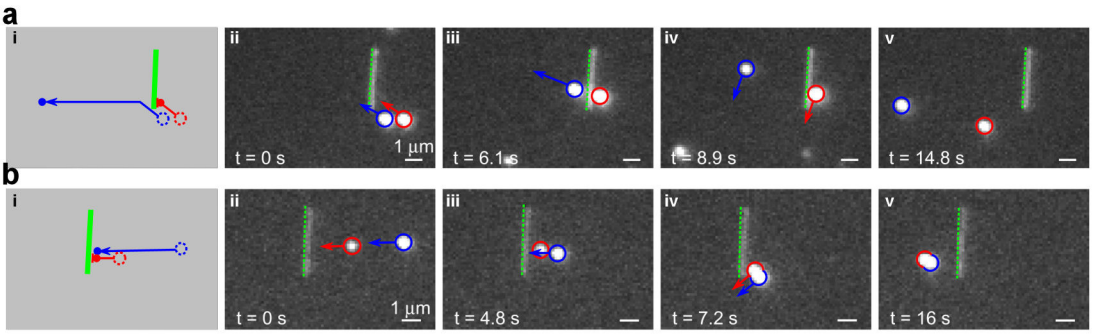

Figure 23: (a){i} Illustration of QD separation (blue from red) using an AgNW barrier. {ii-v} Time-stamped images. (b){i} Illustration of quantum dot coalescence (blue to red) using an AgNW barrier. {ii-v} Time-stamped images. In all panels arrows denote direction of particle motion and green delineates the location of the obstacle barrier.

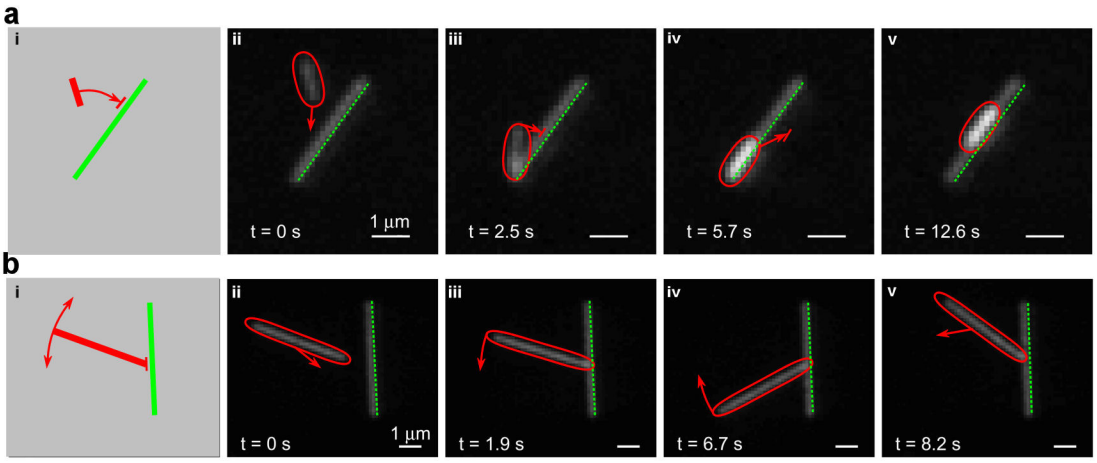

Figure 24: (a){i} Illustration of nanorod alignment to an nanowire guide. {ii-v} Time-stamped images. (b){i} Illustration of nanowire rotation using the foothold of an nanowire barrier. {ii-v} Time-stamped images. In all panels arrows denote direction of fluid flow and object rotation and green delineates the location of the obstacle barrier.

(delineated in green). The figure shows a sequence of time stamped images, along with an illustration of the approach. QD separation uses the end of a silver nanowire as a wedge to pull one QD (circled blue) away from the second (circled red). Figure 23b shows the reverse process, in which the wire is used to combine two QDs by pushing them both up against the barrier. Once combined, the QDs can be positioned together to a desired location. The same approach can also be applied to wires and rods.

In addition to separating and merging, immobile wires can also serve as guides to align mobile nanowires and nanorods along a defined direction. Figure 24a demonstrates this capability. Flow was used to align a gold nanorod with a silver nanowire barrier. We pushed the gold nanorod against the nanowire with flow. The

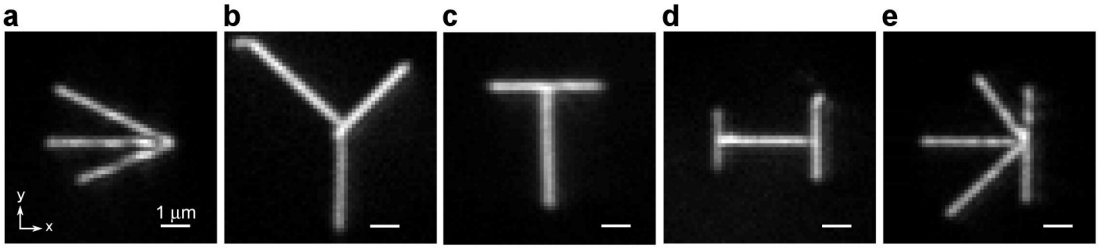

Figure 25: Images of nanowire structures assembled using our toolbox of techniques.

wire served as a barrier that oriented the rod in the parallel direction. Once together, the wire guided the rod, which slid along the wire (panels iv-v).

Immobile nanowires can also orient mobile wires at various relative angles. Figure 24b demonstrates orientation of one silver nanowire using a second immobilized wire as a barrier. We created a component of the fluid flow normal to the barrier to exert a force that held one end of the wire in place by static friction. A component of flow parallel to the barrier could rotate the wire in either direction. Static friction provides ample footing for rotation of angles between 30-40° to the normal.

4.7 Assembling nanoparticles

As a final demonstration, we used a combination of the techniques described in our toolbox to assemble nanoparticle structures from individual silver nanowires, shown in Figure 25. For each structure, we first immobilized a wire either along the y (panels b and e) or x directions (panels a, c, and d) using the technique outlined in Figure 21. We assembled the subsequent wires in panels a-d by first coarsely orienting and placing them near the correct location (technique in Figure 20). Finer orientation was achieved by tacking down one end of the wire and rotating the other

to the desired orientation. Once oriented, the second wire end was immobilized, fixing the whole wire in place (technique described in Figure 21). The structure pictured in Figure 25e used the technique shown in Figure 24b to orient a second wire perpendicular to the first. We oriented subsequent wires using the 'v' shaped grooves created by the first two wires.

4.8 Summary

In this chapter, we demonstrated a microfluidic toolbox for constructing complex nanostructures on chip with nanoscale accuracy. We used electroosmotic flow control and an engineered photoresist fluid chemistry to position and immobilize single nanoparticles on a two-dimensional surface. The mechanics provided by this planar geometry provides the tools necessary for controlled nanoparticle assembly. We employ nanoparticle obstacles and local fluid polymerization to orient and assemble nanoparticles together. This scheme enables bottom-up assembly using immobilized particles as platforms off of which subsequent particles can be built.

We demonstrated assembly of nanostructures using single silver nanowires. These wires are useful for nanophotonic applications since they can guide light, confined to nanoscale volumes, in the form of surface plasmons [96]. The assembly method we develop could enable construction of plasmonic circuits for creating subwavelength interferometers [14] and resonators [13]. In addition, integrating single emitters, such as QDs [15], with plasmonic nanowires can be used to engineer single photon transistors for quantum computation [17] and efficient single photon sources for quantum communication [16].

Flow control achieves positioning of objects independent of their material properties. As a result, a wide variety of particles can be positioned together to assemble complex nanosystems. This capability opens the door for realizing lumped element nanoelectronics [51] and user-defined metamaterials [97]. Flow control also provides the ability to manipulate several particles simultaneously [60]. Incorporating parallel manipulation with our techniques for orienting and immobilizing particles could pave the way for efficiently assembling large scale nanoparticle systems on chip.

Chapter 5: Nanoscale imaging and spontaneous emission control with a single nano-positioned quantum dot

5.1 Introduction

Plasmonic nanostructures confine light on the nanoscale, enabling the creation of ultra-compact optical devices that exhibit strong light-matter interactions. QDs are ideal for probing plasmonic devices because of their nanoscopic size and desirable emission properties. However, probing with single QDs has been challenging because their small size also makes them difficult to manipulate. Here we demonstrate the use of QDs as on-demand probes for imaging plasmonic nanostructures, as well as for realizing spontaneous emission control at the single emitter level with nanoscale spatial precision. A single QD is positioned with microfluidic flow control to probe the local density of optical states (LDOS) of a silver nanowire, achieving 12 nm imaging precision. The high spatial precision of this scanning technique enables development of a new method for spontaneous emission control in which interference of counter-propagating surface plasmon polaritons results in spatial oscillations of the QD lifetime as it is positioned along the wire axis.

Controlled interactions between nano-emitters and plasmonic nanostructures are important for a broad range of applications in photonics and quantum optics. Plasmonic nanostructures localize electromagnetic fields to nanometer dimensions in the form of surface plasmon polariton (SPP) waves. Accurate placement of nano-emitters in the high-field regions of SPP modes can improve the efficiency and directionality of light emitters [98,99], provide large nonlinear optical effects at low light levels [17,100,101], enhance sensing capabilities [102,103], and enable the development of lump-element nanophotonic circuits [51] as well as quantum optical

circuits for quantum networking [16,17]. Nano-emitters can also serve as nearly ideal localized excitation sources that can be used to probe electromagnetic properties of plasmonic nanostructures, such as the LDOS, with high spatial resolution [32].

A variety of methods have been applied for sub-wavelength probing of plasmonic structures. Near-field scanning optical microscopy uses a tapered tip to probe the LDOS [104–109]. This tapered probe, however, can add unwanted distortion to the image [32,110,111]. Other imaging techniques, such as electron energy-loss spectroscopy [112] and cathodoluminescence imaging spectroscopy [113,114], enable the study of plasmonic mode structures with nanometric precision by using a tightly focused electron beam. However, these techniques typically require high vacuum and an electron beam that has been accelerated at high voltage, which has limited their applicability.

An ideal probe for nanoscale electromagnetic imaging is a single, isolated, point-like dipole emitter, which provides high spatial resolution with minimal distortion of the LDOS [32]. Additionally, the strong back-action of the plasmonic nanostructure on the emitter can enhance or suppress spontaneous emission. This back-action provides an effective method for performing spontaneous emission control [15,115], forming the basis for novel light sources [99] and quantum circuits [17]. Methods that incorporate either single emitters [116,117] or ensembles of emitters [115,118] on a scanning tapered probe have been demonstrated for both near-field imaging and spontaneous emission control, but these techniques have so far been limited to an imaging resolution of about 100 nm. Mechanical dragging of diamond nanocrystals in the vicinity of plasmonic structures using scanning-probe manipulators has also been

demonstrated [119,120], but to date this method has only provided sparse sampling of the electromagnetic mode with too few data points to reconstruct an accurate image. Three-dimensional manipulation of 75-nm diamond nanocrystals by optical trapping has also been reported recently and used to image the LDOS of dielectric waveguides [121], but the extension of this approach to plasmonic structures is challenging because the field typically decays on a length scale that is on the order of the size of the nanocrystal. Random diffusion of fluorescent molecules has also been used to image plasmonic hot spots, achieving spatial imaging accuracy as fine as 1.2 nm [122]. However, this procedure is entirely stochastic and cannot be used to probe a desired location or target on demand.

Semiconductor QDs are ideal nano-emitters for local probing and excitation of plasmonic nanostructures. Due to their nanometric size, QDs can act as sensitive probes for studying the electromagnetic properties of plasmonic nanostructures with high spatial precision. However, the application of QDs as nanoscale probes has been challenging. Their small size makes them difficult to manipulate using standard approaches such as optical trapping [37]. Although optical trapping of single QDs has been demonstrated [36], the spatial accuracy of this trapping procedure has not been reported and the positioning accuracy that can be achieved with this approach remains unclear. Additionally, optical trapping forces are not selective, which can result in many particles getting caught in a single trap over a short timescale. Alternate methods that use tapered probes with single QDs attached to the tip [35] or, conversely, scan an attached sample over a single QD immobilized on a surface

[123], have been reported. However, these approaches have been largely limited by QD blinking and bleaching, which significantly distort the acquired image.

In this work we demonstrate that a single QD can be used as a nanoprobe for imaging plasmonic nanostructures and for spontaneous emission control with high spatial accuracy. Specifically, we use a single QD to image the LDOS of a silver nanowire (AgNW). The QD is deterministically positioned at desired locations adjacent to the AgNW by actuating flow in a microfluidic device through electroosmosis [44], thereby moving the QD via viscous drag [82,91]. Using this approach we image the LDOS with a spatial precision as fine as 12 nm. Furthermore, we use the back-action of the AgNW on the QD to perform spatially resolved spontaneous emission control with nanoscale precision. We demonstrate control of the QD lifetime by placing it in regions with different magnitudes of the LDOS. The high spatial precision of our approach reveals oscillations in the QD spontaneous emission rate as it is positioned along the wire axis. These oscillations are the signature of direct coupling to surface plasmon modes induced by interference between counter-propagating surface plasmon waves. The ability to control light-matter interactions at these length scales is crucial for optimizing interactions between single emitters and surface plasmons, and plays an important role in the study of quantum optics in plasmonic structures as well as in the development of nanoscale quantum devices [17].

5.2 Description of imaging approach

Our imaging approach relies on the strong electromagnetic interactions between the QD and the SPP mode of the wire. When a QD is positioned near an AgNW, energy

from the photoexcited QD is transferred to the wire's SPP mode through an electric dipole interaction [15]. The rate of energy decay of an isotropic emitter into the guided SPP mode of the AgNW is given by Fermi's Golden Rule:

$$\gamma_{nw} = 2\pi\mu^2 \left\langle \left|\mathbf{E}(\mathbf{r},\omega)\right|^2 \right\rangle D(\omega), \tag{5.1}$$

where $D(\omega)$ is the spectral density of electromagnetic modes, $\mathbf{E}(\mathbf{r},\omega)$ is the electric field operator for the AgNW mode, and μ is the transition dipole moment of the emitter [124]. Although QDs can exhibit polarized light emission and are therefore not completely isotropic [125], rotational Brownian motion in the fluid averages out orientational effects on a time scale that is much faster than the data integration time (Figure 26), enabling the QD to behave as an effectively isotropic emitter. The spontaneous emission rate is often expressed in terms of the LDOS defined as [126]:

$$\rho(\omega) = \left\langle \left|\mathbf{E}(\mathbf{r},\omega)\right|^2 \right\rangle D(\omega) / 4\pi k^2 \tag{5.2}$$

where k=ω/c. Thus, γ_{nw} is proportional to the LDOS, and provides a direct measure of the local field intensity of the AgNW mode at the location of the emitter. In our experiment, this rate is measured in two independent ways: by monitoring the radiated light intensity from the wire end and by directly measuring the QD lifetime as a function of position. These two observables provide mutually complementary approaches for studying the electromagnetic properties of the wire.

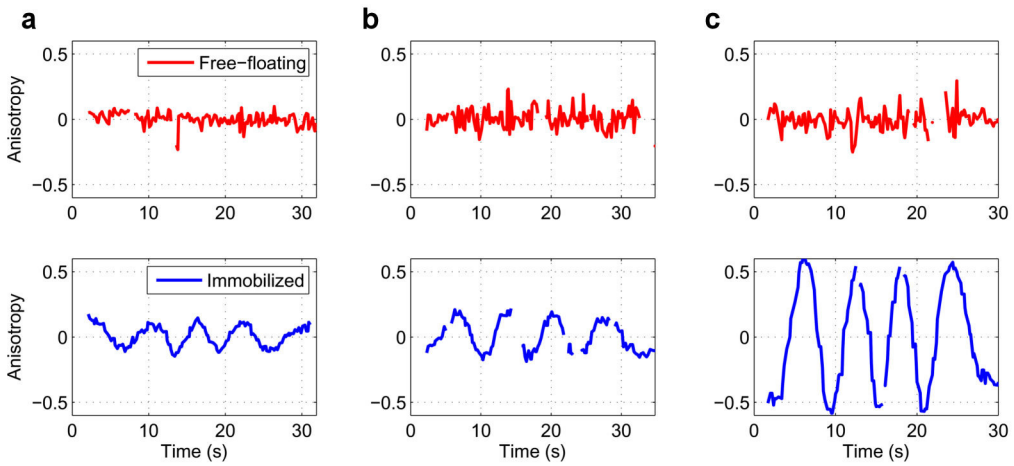

Figure 26: QD polarization in a microfluidic channel. The emission anisotropy of three pairs of QDs (a-c) as a function of polarization (which was rotated in time). Each pair consisted of a free-floating (red) and an immobilized (blue) QD. The emission polarizations for each pair were characterized simultaneously using a setup in which the emission was sent through a half-wave plate and then split into vertical (V) and horizontal (H) polarization by a calcite beam displacer. Plotted here is the measured emission anisotropy, $(I_V-I_H)/(I_V+I_H)$, for each QD as the emission polarization is rotated with the half-wave plate. The immobilized QDs demonstrate a clear polarization dependence, however the free-floating QDs appear largely unpolarized. We attribute this lack of polarization for the suspended QDs to rotational Brownian motion, which causes polarization effects to be averaged out if the data acquisition time exceeds the orientational diffusion rate. As a result, free-floating probe QDs behave as effectively isotropic emitters.

5.3 Experimental procedure

An optical image of the microfluidic device used to position QDs is shown in Figure 27a. Four microfluidic channels intersect at the control region, where QD manipulation occurs (the dashed circle). Figure 27b illustrates the probing procedure for an AgNW. Within the control region, a single QD is selected and driven along a trajectory that samples the LDOS of the wire at a desired set of locations. AgNWs with an average diameter of 100 nm and an average length of 4 μm (SEM image in

Figure 27b inset) are deposited on the polydimethylsiloxane (PDMS) surface of the control region. The channels are filled with fluid containing QDs that are confined to a thin sheath along the surface by the fluid chemistry [91]. Within this sheath, single QDs are manipulated with nanometric precision using flow control. The deposited AgNW acts as an obstacle for the QDs, indicating that the QDs are constrained to be within 100 nm of the surface (the diameter of the AgNW). The QD fluorescence signal is collected using a confocal micro-photoluminescence system [82,91], and 25% of the emission is sent to a CCD camera for tracking. The remaining 75% of the emission is sent to an avalanche photodiode (APD) to perform lifetime measurements. Each detection event from the APD is saved with a time stamp that is synchronized to the camera frame acquisition rate.

The control fluid was composed of 45-48% by volume ethoxylated-15 trimethylolpropane triacrylate resin (SR-9035, Sartomer), 1.25-1.4 wt% rheology modifier (Acrysol RM-825, Rohm and Haas Co.) [69], 0.15-0.3% of a zwitterionic betaine surfactant [70], and CdSe/ZnS core-shell QDs (Ocean NanoTech©, Carboxylic Acid, 620 nm) in deionized water. The triacrylate resin causes the fluid sheath to form. The surfactant was introduced to improve electroosmotic actuation on the PDMS surface while the rheology modifier was used to reduce Brownian motion and inhibit unwanted adhesion of the QDs to surfaces.

The microfluidic device was composed of a molded PDMS cross pattern placed on top of a glass coverslip. The resulting channel was 5 μm in height with a control region that was approximately 100 μm in diameter. The QDs were excited simultaneously by a 532 nm continuous wave laser at an intensity of 250 W/cm^2 and

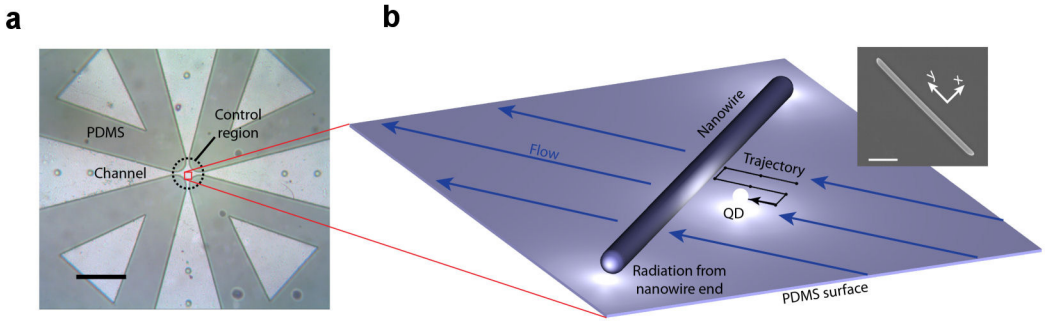

Figure 27: Near-field probing with a single QD. (a) Optical image of the microfluidic crossed-channel device. Flow in the center control region (dashed circle) is manipulated in two dimensions by 4 external electrodes (not shown). Scale bar is 500 μm. (b). Schematic of the positioning and imaging technique. A single QD is driven along a trajectory close to the wire by flow control. The coupling between the QD and AgNW is measured either by the radiated intensity from the wire ends or by QD lifetime measurements. The inset shows an SEM image of a typical AgNW used in our experiments with 1 μm scale bar. The x-y coordinate system is defined relative to the orientation of the AgNW, as illustrated in the inset.

a 405 nm pulsed laser with a 10 MHz repetition rate at 35 W/cm^2. A fraction (25%) of the QD emission was imaged using an EMCCD camera (Hamamatsu C9100-13) operating at 10 Hz frame rate while the remaining signal was focused onto an avalanche photodiode (APD, PerkinElmer SPCM-AQR) for time-resolved lifetime measurements. Data were analyzed using a time-correlated single-photon counting module (PicoQuant PicoHarp300) that synchronizes photon events with camera frames.

QD positions were tracked with sub-wavelength accuracy by fitting the imaged diffraction spot to a Gaussian point-spread function. The spatial accuracy of the tracking algorithm is limited by system vision noise, which includes a combination of camera read noise, multiplication noise, and shot noise. We determined the tracking

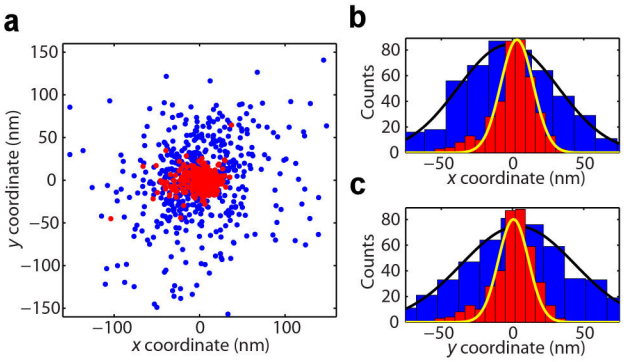

Figure 28: QD tracking and positioning accuracy. (a) Scatter plots of the measured positions of a QD over the course of one minute. Red data points correspond to a QD that is immobilized while blue data points correspond to a QD that is held in place by flow control. (b-c) Histograms of the x and y coordinate corresponding to data from panel a. Red bars are the histogram for an immobilized QD, while blue bars are the histogram for a positioned QD. The yellow solid line is a Gaussian fit for an immobilized QD showing a measure standard deviation of 12 ± 1 (11 ± 1) nm along the x (y) coordinate. The black solid line is a Gaussian fit for the positioned QD with standard deviation of 36 ± 2 (40 ± 2) nm for the x (y) coordinate.

accuracy by monitoring an immobilized QD on a glass surface for one minute. The measured QD positions are plotted as red points in Figure 28a. The red bars in Figure 28b-c plot a histogram of the measured QD position along the x and y coordinates respectively. The solid yellow line represents a Gaussian fit, the standard deviation (s.d.) of which is used to determine a tracking precision of σ_{tr} = of 12 ± 1 (11 ± 1) nm along the x (y) directions.

Nanoscale positioning precision is achieved by employing vision-based feedback control that creates corrective flows to position the QD at a desired location. The positioning precision is measured by monitoring a QD that is held in place by flow control for one minute. The measured QD positions are plotted as blue data points in

Figure 28a. The blue bars in Figure 28b-c are a histogram of these measurements, while the black solid line is a Gaussian fit for which the s.d. gives a positioning accuracy of σ_p = 34 ± 3 (39 ± 3) nm along the x (y) directions. These numbers were corrected for noise in the tracking algorithm using the relation $\sigma_p = \sqrt{\sigma^2 - \sigma_{tr}^2}$, where σ is the total measured position fluctuations. These results indicate that we can deterministically probe the wire mode at a desired location on demand with nanometric precision. It is important to note that the positioning accuracy does not limit the spatial imaging accuracy of the system, since the position of the QD is known to a higher precision than that with which it can be controlled.

Figs. 29a-c show a series of images of a single QD being moved progressively closer to an AgNW. When the QD is close to the wire, light radiates from the wire ends

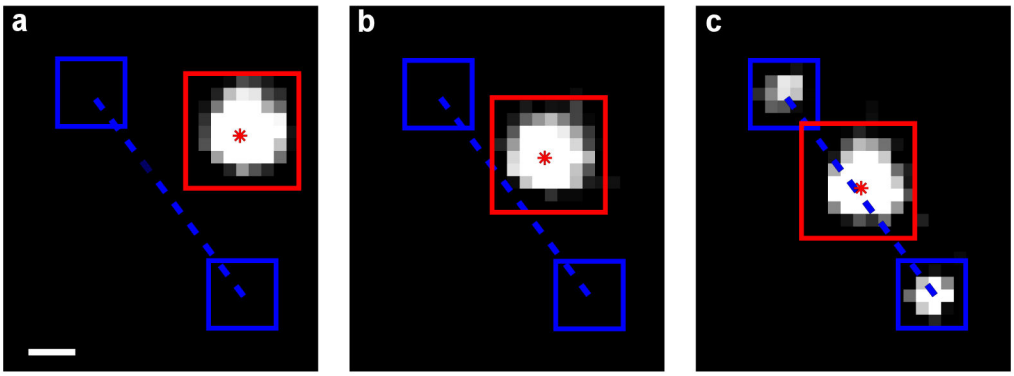

Figure 29: Coupling a QD to an AgNW. (a-c) This series of images shows coupling of the QD to the AgNW as the QD is moved closer to the wire. The scale bar is 500 nm and intensities are plotted on a logarithmic scale. The red and blue boxes show the image integration region used to calculate the radiation intensities and positions of the QD and the wire ends, respectively. The measured location of the QD is labeled with a red star and the axis of the AgNW is labeled with a blue dashed line.

(Figure 29c). This radiation arises from direct dipolar coupling of the QD excitation to the waveguided SPP mode. The extraction efficiency of the QD excitation into the AgNW mode is given by $\eta_{ex} = \gamma_{nw} / \gamma$ where γ is the total decay rate of the QD due to all radiative and non-radiative decay channels, and γ_{nw} is defined in equation (5.1). In the limit in which γ is dominated by free-space modes the efficiency is proportional to the LDOS at the location of the emitter. Therefore, by simultaneously monitoring the QD position and the radiated intensity from the wire end we can construct an image of the LDOS. In addition, we can determine the LDOS by directly measuring the QD radiative lifetime [115]. Such direct lifetime measurements have the advantage that they are independent of sample geometry, since they do not rely on monitoring the AgNW end radiation. Thus, in contrast to measurements that monitor the end of a wire, lifetime imaging can be applied to objects that are sub-wavelength in all three dimensions, such as metallic nanospheres and nanorods.

QD probing was performed at various locations along the middle and end of an AgNW. The QD trajectory was selected to maximize data sampling near the wire surface (Figure 30). A significant challenge of probing with QDs is that they blink [127], which leads to emission intensity fluctuations that complicate the interpretation of the radiated intensity from the wire end. Our imaging approach offers a convenient solution to this problem because it enables the simultaneous measurement of the intensity radiated both from the wire end and directly from the QD. The direct radiation from the QD is used to normalize for QD blinking and local field enhancement of the pump. The QD emission and the AgNW radiated intensity are

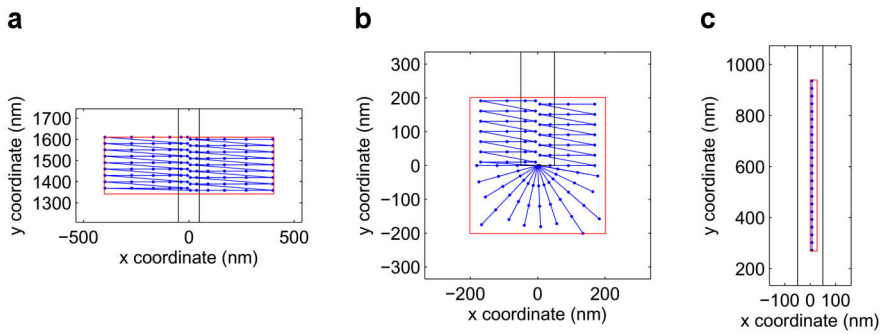

Figure 30: Scanning Trajectories. (a) Mid-wire scanning trajectory (corresponding to Figure 31). (b) A trajectory scanning the wire tip (corresponding to Figure 34). (c) A trajectory scanning the wire along the side (corresponding to Figure 36). Blue points connected with lines correspond to the trajectory points, connected in order of scanning. During the experiment, flow is applied to position the QD to the desired trajectory point for two seconds before moving on to the next point. Red boxes define the scanning regions. Black lines designate the physical extent of the wire. Some points along the trajectory lie inside the wire or on the opposite side of the wire, however, since the wire acts as an obstacle the QD cannot generally reach these points and instead is forced against the wire to ensure data is collected as close as possible to the surface. Additionally, the trajectory points are more densely spaced closer to the wire in order to ensure probing of the near-field region.

measured by summing the pixels within their respective windows (Figure 29a-c). We define the normalized coupled intensity $\bar{I}$ as:

$$\bar{I}(x,y) = \frac{\sum_{n,m}\left(I_{n,m}^{NW} - I^{BKG}\right)}{\sum_{p,q}\left(I_{p,q}^{QD} - I^{BKG}\right)} \tag{5.3}$$

where $I_{n,m}^{NW}$ and $I_{p,q}^{QD}$ are the intensities of the $(n,m)^{th}$ and $(p,q)^{th}$ pixels within the AgNW and QD windows respectively, while I^{BKG} is the average pixel background intensity. The background level is calculated by averaging pixels sufficiently far away

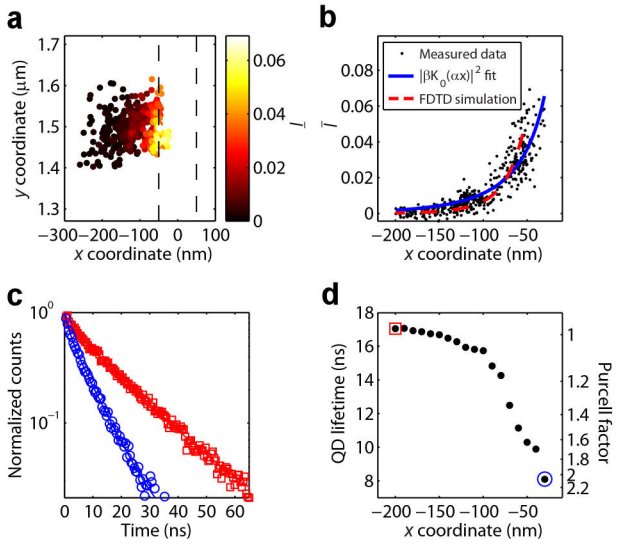

Figure 31: Probing the LDOS profile near the middle of the AgNW. (a) $\bar{I}$ as a function of position near the middle of the wire. The dashed region indicates the assumed location of the AgNW surface. (b) $\bar{I}$ as a function of distance from the wire axis (x coordinate) using data from panel a. The blue line indicates the best fit to a modified Bessel function. The red dotted line is an FDTD simulation of the AgNW evanescent field. The simulation result was fit to the data using an overall scaling factor. (c) Radiative decay of the QD at 200 nm (red squares) and 30 nm (blue circles) distance from the AgNW axis with lifetime fits of 17 and 8 ns respectively. (d) QD lifetime as a function of x position. The second y-axis denotes the Purcell factor corresponding to the measured lifetimes. Colored markers indicate the data points used for panel c.

from the AgNW and the QD. The value of $\bar{I}$ is proportional to the coupling efficiency η, and thus to the LDOS of the nanowire.

5.4 Probing the side of an AgNW

Figure 31a is a scatter plot of $\bar{I}$ as a function of QD position when the QD was positioned near the midpoint of the AgNW. The dashed lines represent the location of the AgNW surface, which is assumed to be 50 nm from the wire axis (the typical

radius of the wires used in this work). The wire orientation and length were determined by tracking the diffraction spots of the radiated light from the wire ends (blue boxes in Figure 29c) with the same algorithm used to track the QD. The data points are plotted relative to the measured wire location with the y-direction aligned along the wire axis and the x-direction corresponding to distance from the wire axis, as indicated in the inset of Figure 27b, with the origin placed at the lower end of the wire.

Figure 31b shows $\bar{I}$ as a function of radial distance from the wire axis. $\bar{I}$ is seen to increase as the QD approaches the wire surface. For a cylindrically symmetric AgNW, the evanescent field from the surface is predicted to follow a Bessel-function decay [128]. The data are therefore fit to a function of the form $\left|\beta K_0(\alpha x)\right|^2$ where $K_0(\alpha x)$ is the zeroeth-order modified Bessel function, x is the distance from the AgNW axis, and α and β are fitting parameters (calculated from the fit to be 0.006 nm^{-1} and 0.142, respectively). The solid blue line in Figure 31b is the Bessel-function fit and the red dashed line corresponds to the AgNW evanescent field as calculated using a finite-difference time-domain (FDTD) method. The FDTD solution was multiplied by a constant to provide the best fit to the data. Both the analytical and numerical solutions show good agreement with the measured LDOS profile.

Simulations were performed using the Lumerical FDTD Solutions software package (http://www.lumerical.com). A 4 μm long silver nanowire with 100 nm diameter was simulated surrounded by a background index of 1.4, which corresponds to the index of refraction for PDMS. The QD fluid was assumed to have the same index.

Simulations were performed by exciting the AgNW with a transient dipole source, and calculating the field after the dipole excitation had finished.

The spontaneous emission lifetime of the QD was measured using the APD while the camera simultaneously measured the QD position. Figure 31c shows two time-resolved fluorescence measurements obtained by collecting photon events detected when the QD was at radial distances of 200 ± 12 nm (red squares) and 30 ± 12 nm (blue circles) from the wire axis, respectively. A biexponential fit was used to determine the QD's lifetime [129], yielding values of 17 ns and 8 ns for the two distances, respectively. This reduction in lifetime at short distance is consistent with previous measurements of QDs coupled to nanowires [15].

Figure 31d plots the QD lifetime as a function of position. Each lifetime was calculated by grouping all photon events in which the QD was within a ±12 nm window from the specified radial distance. The positional dependence of the lifetime mirrors the intensity of the emission from the wire end, demonstrating a clear agreement between the two methods, as well as the ability to perform spontaneous emission control by localizing the QD near the wire surface. The color scale in Figure 31d is labeled both in units of raw lifetime (left labels) and Purcell factor (right labels), which is defined as $F_P = \gamma / \gamma_0$, where γ_0 is the emission rate of the QD far from the AgNW and γ is the measured decay rate.

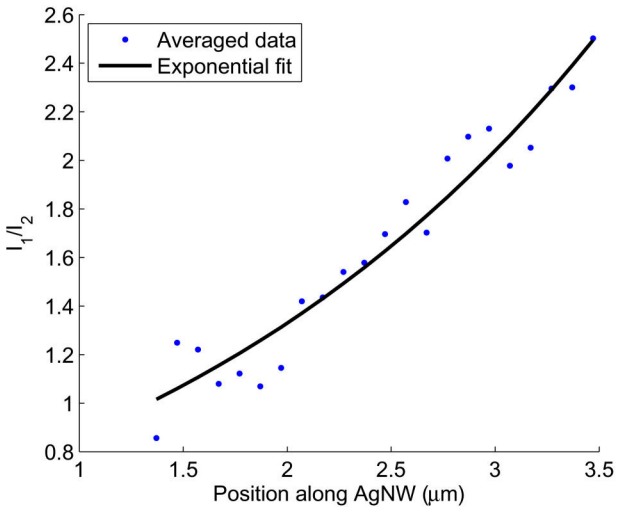

Figure 32: SPP decay along AgNW length. Ratio of emission intensity measured from both AgNW ends as a function of position along the wire. The black line is an exponential fit.

5.5 Propagation loss

In probing along the length of the AgNW, the measured parameter $\bar{I}$ may experience distortion due to different propagation losses to the wire end. The position dependence of propagation loss can be determined by monitoring the emission intensity from the two ends of the AgNW simultaneously as the QD is moved along the length of the wire. Here we calculate the propagation length of a typical AgNW used in this work. We describe the radiated intensity from the two AgNW ends as having an exponential dependence according to:

$$\begin{aligned} I_1 &= \beta^{(1)} e^{-(x-L/2)/x_l} \\ I_2 &= \beta^{(2)} e^{(x-L/2)/x_l} \end{aligned} \tag{5.4}$$

where x is the location of the QD between the wire ends, $\beta^{(1)}$ and $\beta^{(2)}$ are the radiated intensities from the two AgNW ends labeled (1) and (2) when the QD is coupled in the middle of the wire, L is the length of the wire, and x_l is the decay length of the SPP mode. In the case in which the two facets of the AgNW are completely symmetric, $\beta^{(1)} = \beta^{(2)}$, but in general these parameters are not equal.

The ratio of the measured intensities is therefore:

$$\frac{I_1}{I_2} = \beta e^{-2x/x_l} \tag{5.5}$$

where β and x_l are now constant fitting parameters. Figure 32 shows the average value of I_1 / I_2 as a function of position along an AgNW for an experiment in which the QD was probed along the length of the wire. We use a fitting function of the form in Eq (5.5) and calculate a propagation length of 4.7 μm, which corresponds well with other published results [13]. This absorption length is much longer than the 200 nm scanning distance along the y-direction used for Figure 31. As a result, propagation losses are expected to have only a minimal effect on the measured parameter $\bar{I}$.

5.6 Spatial accuracy of measured QD positions

The measurements in Figure 31b can be used to determine the spatial imaging accuracy. This accuracy is the root-mean-square (rms) deviation in the measured positions of the QD relative to the position predicted by the Bessel-function fit. The rms deviation provides an upper bound on the spatial imaging accuracy.

Here we derive a bound on the spatial accuracy of the measured data points. We use the data in Figure 31b, which have been reproduced in Figure 33a. Both the measured data and Bessel-function fits are shown as a function of distance from the wire axis. The red lines indicate the spatial distance of each data point from the predicted value given by the Bessel function fit. Fluctuations in the spatial coordinate of the raw data relative to the Bessel function arises from both position uncertainty due to measurement error (fluctuations along the horizontal axis) and intensity noise (fluctuations along the vertical axis). Thus,

$$\sigma_d^2 = \sigma_x^2 + S_I \sigma_I^2 \tag{5.6}$$

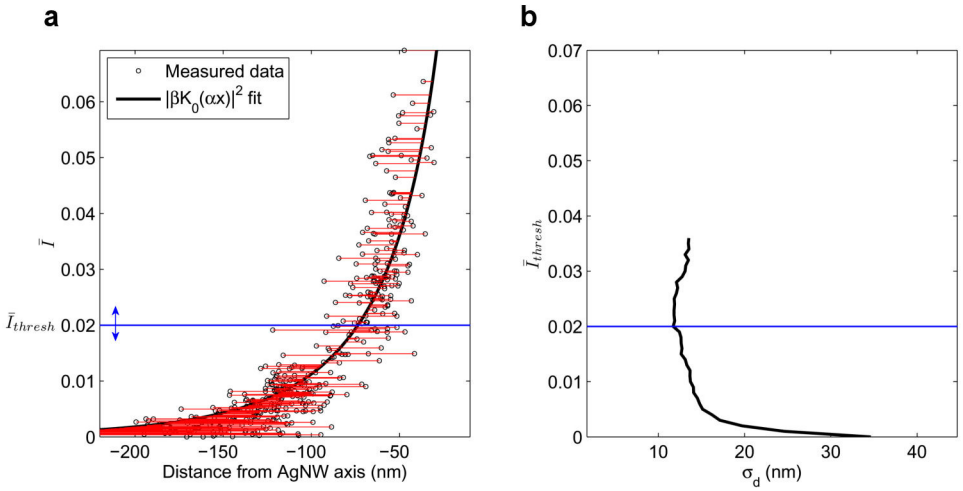

Figure 33: Spatial accuracy of measured QD positions. (a) Figure 31b with Bessel-function fit. Red lines indicate spatial distance between the measured QD position and position predicted by Bessel-function fit based on the measured intensity. $\bar{I}_{thresh}$ is labeled with a blue line. (b) Plot of σ_d for a range of $\bar{I}_{thresh}$ values. The minimum standard deviation of 12 nm occurs at $\bar{I}_{thresh}$ = 0.02 and is represented by the horizontal blue line.

where σ_d represents the fluctuations in the distance between the measured position and predicted value (the red lines in Figure 33a), and σ_I represents fluctuations in the measured value of $\bar{I}$ due to effects such as shot noise and camera pixel noise. The spatial imaging accuracy is given by σ_x, which is the uncertainty in the measured value of the QD position. $S_I = \left[\partial d / \partial \bar{I}\right]^2$ is the sensitivity parameter for the intensity fluctuations, which depends on the slope of the Bessel function at the measured intensity value. We calculate σ_d using the rms distance between data points and the Bessel function fit along the position axis. From Eq. (5.6) it can be seen that $\sigma_x \leq \sigma_d$. Thus, σ_d provides a worst case estimate of the spatial imaging accuracy.

The inequality, $\sigma_x \leq \sigma_d$, will tend to overestimate the imaging accuracy when intensity noise is not negligible. From the Bessel-function fit one can see that when the QD is near to the nanowire (approximately 50 nm from the surface) the measured intensity is strongly dependent on the position of the QD due to the steep slope of the curve. In this region the value of S_I, which is related to the inverse of the slope, is small and we expect the noise to be dominated by the measurement inaccuracy of the QD position. Further away from the wire, where the slope becomes shallow and S_I becomes large, the intensity noise contributes significantly to the measured error. In this region, the bound will overestimate uncertainty of the measured QD position.

To prevent overestimation of the calculated spatial accuracy we introduce an intensity threshold $\bar{I}_{thresh}$, as indicated in Figure 33a. All data points whose coupled intensity $\bar{I}$ exceeds this threshold are included in the calculation for σ_d, while data points that

lie below the cutoff are rejected. We varied $\bar{I}_{thresh}$ to determine when the intensity noise becomes significant in the calculation of σ_d. Figure 33b plots σ_d as a function of $\bar{I}_{thresh}$. The calculated σ_d is largely independent of the intensity threshold for larger values of $\bar{I}_{thresh}$. For $\bar{I}_{thresh} < 0.01$ the bound for the position accuracy begins to increase rapidly because we are including more data points from the region that is highly sensitive to intensity noise. Since each data point in Figure 33b represents an upper bound on the spatial accuracy, we take the minimum value as the tightest upper bound which gives the best estimate. The minimum value is calculated to be 12 nm and is attained at $\bar{I}_{thresh} = 0.02$ (plotted with a horizontal blue line), which is consistent with the 12 ± 1 nm tracking accuracy calculated previously by observing an immobilized QD, indicating that the spatial imaging accuracy is primarily limited by vision noise.

5.7 Probing the tip of an AgNW

Figure 34a is a scatter plot of data recorded when a QD was scanned near one end of the AgNW while the intensity was monitored at the opposite end. Probing the AgNW tip required several minutes of QD scanning. Over this time span, sample drift can be appreciable, potentially creating image distortion. To account for sample drift, the QD position was measured relative to the wire end that was tracked throughout the experiment. The ability to correct for drift represents an important practical advantage of this approach, enabling us to acquire images over long periods without distortion.

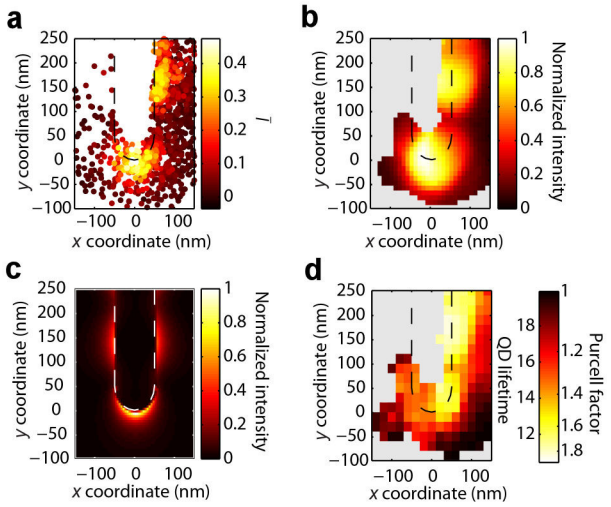

Figure 34: Probing the tip of an AgNW. (a) Scatter plot of measured positions and intensities near the end of the AgNW. The color of each data point corresponds to $\bar{I}$. The dashed region indicates the location of the AgNW. (b) Reconstructed image using a Gaussian-weighted average. The image intensity is normalized by its maximum. (c) FDTD simulation of the AgNW mode profile showing an enhancement at the tip (also normalized by its maximum). (d) Image of the measured QD lifetime as a function of position. The color scale is labeled with both lifetime and Purcell factor.

The raw data presented in Figure 34a can be used to construct an image of the LDOS. The value of each pixel in the image is found by taking a Gaussian-weighted spatial average of the raw data. The Gaussian is centered at the location of the pixel and the standard deviation is set to 33 nm, corresponding to the rms combined spatial accuracy of the QD (12 nm) and the tracked AgNW end (30 nm) (see Figure 35). The reduced spatial accuracy at the wire ends is attributed to the fact that their emission is much dimmer than the direct QD emission, as can be seen in Figure 29c. The additional error incurred by tracking the wire end is not fundamental to the imaging

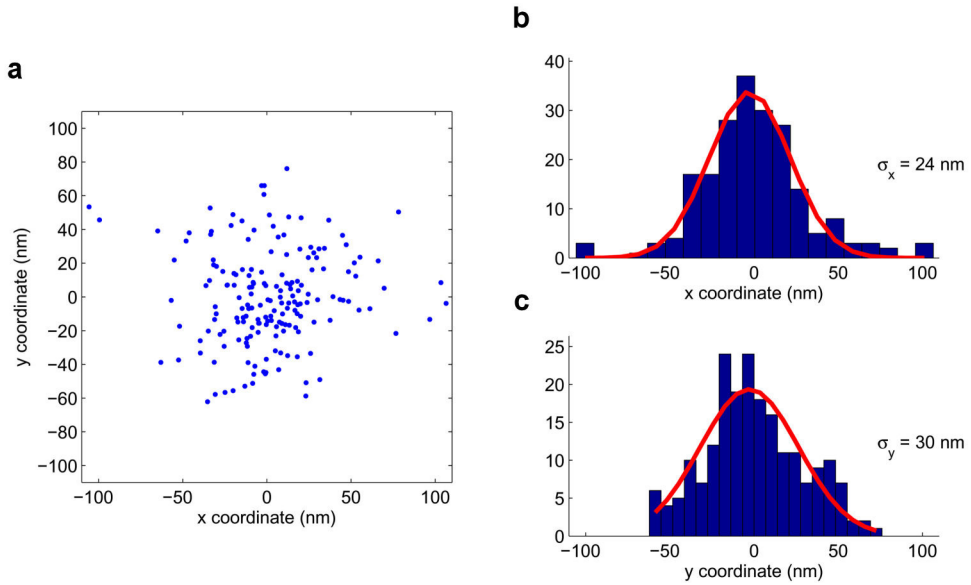

Figure 35: Spatial accuracy of measured AgNW end positions. (a) Scatter plot of the measured positions of an AgNW end over the course of 1 minute. (b-c) Histograms of the x and y positions with Gaussian fits measuring 24 ± 2 and 30 ± 3 nm standard deviations respectively. A single QD is placed on an AgNW and the position of the wire end is determined by measuring the center of the diffraction spot of the radiated light and fitting it with a Gaussian point spread function. This light radiated from the wire end is much dimmer than the direct emission from the QD. Thus, the accuracy with which we can track the AgNW is worse than the accuracy with which we can track the QD.

procedure and could be largely removed by using brighter tracking objects to monitor the drift. The resulting two-dimensional image is shown in Figure 34b. Comparison of the measured LDOS profile with the calculated mode obtained from FDTD simulations (Figure 34c) shows good agreement. Figure 34d plots the measured QD lifetime in the region around the AgNW tip. Each lifetime measurement was obtained by combining all photon events for which the QD was within a 33 nm radius of the center pixel location. The measured lifetime exhibits good agreement with the results obtained from measuring the intensity of the wire end.

5.8 Spatial oscillation of the LDOS due to interference

In addition to the high field intensity at the wire end, the data in Figure 36 suggest the presence of an oscillatory mode structure along the sides of the AgNW. To examine this mode structure in more detail, the LDOS was probed along a 500 nm region at one end of a wire. The measurement results for $\bar{I}$ are shown in Figure 36a, where position is once again plotted relative to the wire end to compensate for drift. In this measurement, the QD was positioned as closely as possible to the wire surface. Under

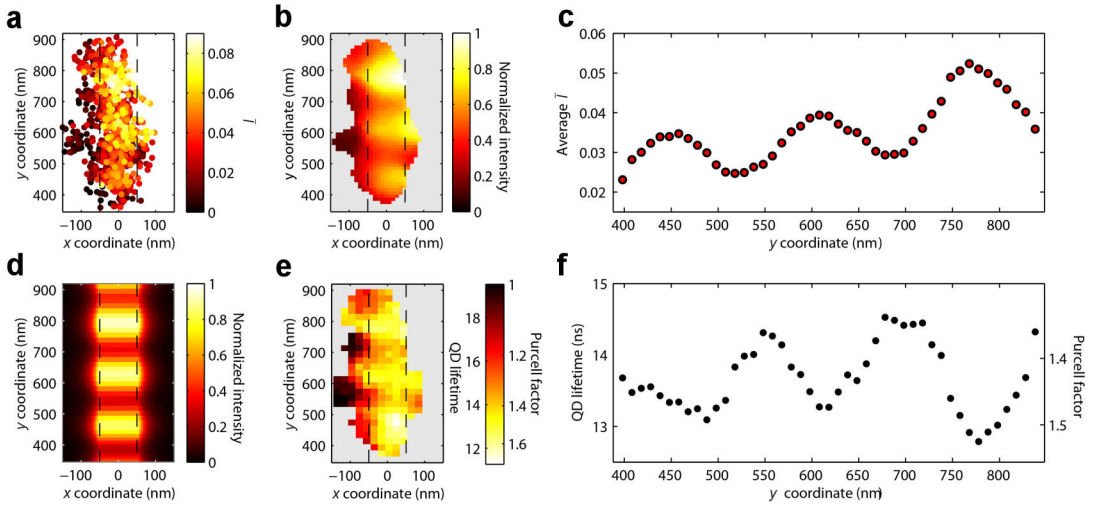

Figure 36: SPP wave interference along an AgNW. (a) Scatter plot of the measured QD positions near the end of the wire. The color of each data point corresponds to the value of $\bar{I}$ measured at each location. The dashed region indicates the location of the AgNW. (b) Reconstructed image using a Gaussian-weighted average. The image intensity is normalized by its maximum. (c) Plot of an averaged value of $\bar{I}$ as a function of position along the wire. (d) FDTD simulation of the field intensity standing-wave pattern along the side of the AgNW (normalized by its maximum) with the profile within the dashed wire region corresponding to the field immediately outside the wire. (e) Image of the measured QD lifetime as a function of position. The color scale is labeled with both lifetime and Purcell factor. (f) Plot of QD lifetime measured along the length of the AgNW.

these conditions most of the QD positions were measured within the dashed AgNW region. Data points located within this region are attributed to the QD being pushed slightly onto the top of the wire, which does not act as a perfect obstacle.

A periodic pattern is observed in the scatter plot along the length of the AgNW. These oscillatory fringes arise from interference between the QD emission component coupled to the forward propagating SPP wave and the backward propagating wave that is reflected from the wire end [13]. The oscillatory pattern is more readily observed in the Gaussian image reconstruction in Figure 36b. Figure 36c shows $\bar{I}$ plotted as a function of the y coordinate. Each data point is averaged over a ±33 nm window centered at the y coordinate. Averaging is performed only for points that are within 50 nm of the wire axis. By measuring the peak-to-peak distance from Figure 36c we determine the wavelength of the SPP mode to be 320 nm, which is consistent with the 329 nm wavelength calculated from FDTD simulations. The simulated FDTD field profile is displayed in Figure 36d and exhibits good qualitative agreement with the measured data.

The spatial dependence of the QD lifetime along the AgNW is shown in Figure 36e. The lifetime in a given pixel was measured by consolidating all photon count events when the QD was within 33 nm of the center location of the pixel. Figure 36f shows the QD lifetime when photon counts were combined using the same spatial window used to obtain Figure 36c. A clear oscillation in the QD lifetime is observed, mirroring the oscillations in intensity from the wire end. The QD lifetime oscillation is caused by interference between the spontaneous emission components of the forward and backward propagating SPP waves. This mechanism for modifying the

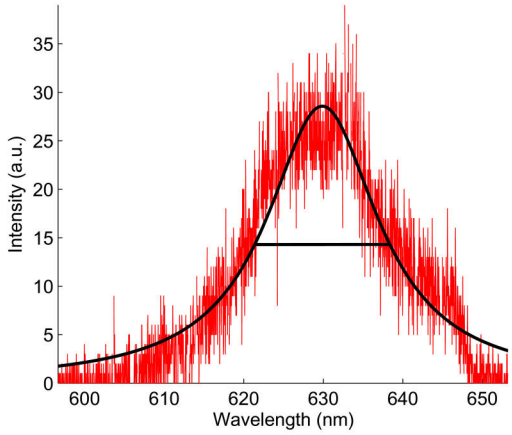

Figure 37: Single QD Spectrum. Emission spectrum (red) of a single QD that was immobilized on a glass coverslip as measured using a grating spectrometer (Acton SP 2758). The black curve is a Lorentzian fit that indicates a spectral linewidth of 17 nm.

spontaneous emission provides an important means of controlling and optimizing light-matter interactions between quantum emitters and nanophotonics structures.

The oscillations in Figure 36 result from the interference between the forward-propagating SPP wave and the backward wave that reflects from the near end of the AgNW. Interference will occur so long as the length difference between the two paths of the SPP waves is within the coherence length of the optical field, which can be determined from the measured emission spectrum of a single QD. This measurement was performed using a grating spectrometer (Figure 37). The spectral bandwidth of the QD emission, in units of free space wavelength, was determined to be $\Delta\lambda_0 = 17$ nm centered at a wavelength of $\lambda_0 = 630$ nm, which agrees well with other measured results [68,130]. The coherence length of the field propagating in the AgNW can be calculated directly from the measured spectral bandwidth using the relation [131]

$$L_{coh} = \frac{1}{2\pi}\frac{\lambda^2}{\Delta\lambda} \tag{5.7}$$

where λ = 320 nm is the measured wavelength of the SPP mode and $\Delta\lambda = \Delta\lambda_0(\lambda/\lambda_0)$. From the measured QD emission bandwidth and wavelength of the SPP mode the coherence length is calculated to be 1.89 μm, which is long enough to observe good interference at a distance of up to 944 nm away from the AgNW end. Thus, the relatively narrow emission bandwidth of QDs makes them ideal candidates for studying interference and coherent optical effects in plasmonic nanostructures. It should be noted that other nanoscopic emitters, such as fluorescent molecules and nitrogen vacancy centers in nanodiamonds, can have much broader room-temperature emission linewidths [26,132], sometimes exceeding 100 nm. These broad linewidths result in a significantly reduced coherence length, making it more difficult to probe interference effects without spectral filtering, which would result in a large reduction of measured signal.

5.9 Summary

In summary, we have demonstrated a technique for both nanoscale imaging of the LDOS of a silver nanowire and spontaneous emission control using a single nano-manipulated QD. These results enable on-demand control of light-matter interactions and provide a highly flexible method to optimize coupling between single quantum emitters and nanophotonic structures. Additionally, the probing method that we have presented could also find applications in the study of other nanoscale phenomena such as Förster resonance energy transfer [118] and local electric field sensing [133].

We note that the demonstrated probing technique is highly robust to emitter degradation and photobleaching [68]. If the probe emitter degrades, it can be discarded and a replacement can be selected from the ensemble to continue the scan seamlessly, enabling image acquisition over long integration times. Combining this probing scheme with precision placement and immobilization of individually chosen QDs [91] would enable deterministic and optimized assembly of active quantum emitter and plasmonic structures for development of nanoelectronic devices [51] and quantum optical circuits [17].

Chapter 6: Conclusion and future directions

In my thesis, I demonstrated manipulation of single nanoparticles with nanoscale accuracy using electroosmotic flow control. I achieved positioning accuracies of 39 nm for single QDs and 5 nm for silver nanowires. Positioning accuracy is predominantly limited by object Brownian motion and camera vision noise. Flow control can position brighter and larger objects better because they are more easily visualized above camera noise and move more slowly in the fluid. Therefore, flow control positions nanowires, which are relatively large and bright, more accurately than QDs, which are smaller and dimmer. Improvements to QD positioning can be achieved by increasing fluid viscosity to reduce Brownian motion, up to the point where viscosity inhibits electroosmotic actuation. Improvements beyond this limit require a more sensitive imaging system.

The concept of flow control works regardless of the imaging system. In general, positioning requires a microfluidic cross-channel, a voltage supply with electrodes, and several off-the-shelf chemicals. All of these components are relatively inexpensive. The other requirements are an imaging microscope and controller software, both of which can be customized based on the application. Thus, flow control can be easily implemented as a microscope attachment for positioning a variety of micro- to nano-sized objects.

Electroosmotic flow control offers a desirable all-in-one approach for particle manipulation. I demonstrate positioning of both single QDs and plasmonic wires using flow control. This technique scales more favorably for positioning nanoscale objects than do conventional approaches like optical tweezers. Fluid actuation also

moves particles independent of their material properties and can position mechanically or optically fragile objects that would be damaged by other methods.

The versatility of flow control enables assembly of many different objects together for bottom-up construction of complex nanoscale systems. Using flow control, I assembled structures composed of plasmonic nanowires. Such structures could be useful for sub-wavelength optical circuitry. Future assembly could include integrating active elements, such as QDs, with plasmonic wires for creating quantum transistors and optical logic gates.

Incorporating other modes of feedback with vision tracking could improve nanoscale assembly. For example, QD lifetime measurements can be integrated with feedback control to optimize dot placement and maximize coupling to a plasmonic wire. As a part of this thesis, I demonstrated that the local density of states for a silver nanowire could be visualized using QD lifetime imaging, incorporating this measurement for feedback positioning would be the next step. Another improvement would be to combine spectral measurements with feedback control. This approach could be used to help assemble nanostructures with tailored optical resonances.

Flow control assembly requires engineering fluid chemistry to localize and immobilize particles along a channel surface. I engineer this fluid chemistry by introducing a water-immiscible monomer and a water-soluble photoinitiator to the fluid. Microfluidics is flexible when it comes to system fluid chemistry. There remain many opportunities for developing “smart” fluids to enhance object manipulation. Examples include fluids that locally and reversibly change viscosity to temporarily

immobilize particles, and fluids that trigger local agglomeration of objects to assemble suspended structures without immobilizing them to a surface.

Engineering channel surface chemistry can also improve particle manipulation. Several features of my particle positioning approach are intimately linked with surface chemistry, such as inhibiting unwanted surface adhesion and actuating electroosmosis. I find that hydrophobic surfaces, such as that of PDMS, prevent unwanted surface adhesion, yet weaken electroosmosis. Introducing a zwitterionic surfactant to the fluid recovers electroosmotic actuation. Incorporating other surfactants to the fluid or modifying the surface with chemical monolayers could improve flow control positioning on various substrates, such as patterned substrates like planar photonic crystal heterostructures that are fabricated using top-down techniques. The ability to integrate single nanoparticles with these pre-patterned surfaces would bridge the gap between top-down and bottom-up fabrication.

In conclusion, I developed a technology for manipulating single nanoparticles with nanoscale precision. Microfluidic positioning addresses problems specific to colloidal QDs, which are difficult to position by other means. This approach is versatile and can position other types of nanoparticles, including metallic nanowires and rods. By engineering system fluid chemistry, I deterministically immobilized and assembled single nanoparticles with nanoscale precision. I extended particle positioning to demonstrate nanoscale probing. This technique positions a single quantum dot to scan and probe the local density of optical states of a plasmonic nanowire. With this probing technique, I achieved 12 nm imaging accuracy and the first demonstration of

lifetime imaging with a single positioned emitter. These results establish microfluidics as a valuable tool for studying and engineering nanoscale systems.

Bibliography

[1] C. Gunn, "CMOS Photonics for High-Speed Interconnects," *IEEE Micro* **26**(2), 58–66 (2006).

[2] R. Bose, D. Sridharan, H. Kim, G. S. Solomon, and E. Waks, "Low-Photon-Number Optical Switching with a Single Quantum Dot Coupled to a Photonic Crystal Cavity," *Phys. Rev. Lett.* **108**(22), 227402 (2012).

[3] C. H. Bennett and G. Brassard, "Quantum Cryptography: Public Key Distribution and Coin Tossing," in *IEEE International Conference on Computers, Systems & Signal Processing*, pp. 175–179, IEEE, New York, Bangalore, India (1984).

[4] P. W. Shor, "Polynomial-Time Algorithms for Prime Factorization and Discrete Logarithms on a Quantum Computer," *SIAM J. Comput.* **26**(5), 1484–1509 (1997).

[5] A. P. Alivisatos, "Semiconductor Clusters, Nanocrystals, and Quantum Dots," *Science* **271**(5251), 933–937 (1996).

[6] R. D. Averitt, D. Sarkar, and N. J. Halas, "Plasmon Resonance Shifts of Au-Coated Au2S Nanoshells: Insight into Multicomponent Nanoparticle Growth," *Phys. Rev. Lett.* **78**(22), 4217–4220 (1997).

[7] K. Asakawa, Y. Sugimoto, Y. Watanabe, N. Ozaki, A. Mizutani, Y. Takata, Y. Kitagawa, H. Ishikawa, N. Ikeda, et al., "Photonic Crystal and Quantum Dot Technologies for All-Optical Switch and Logic Device," *New J. Phys.* **8**(9), 208 (2006).

[8] B. Luk'yanchuk, N. I. Zheludev, S. A. Maier, N. J. Halas, P. Nordlander, H. Giessen, and C. T. Chong, "The Fano Resonance in Plasmonic Nanostructures and Metamaterials," *Nature Mater.* **9**(9), 707–715 (2010).

[9] W. L. Barnes, A. Dereux, and T. W. Ebbesen, "Surface Plasmon Subwavelength Optics," *Nature* **424**(6950), 824–830 (2003).

[10] K. Hinton, G. Raskutti, P. M. Farrell, and null, "Switching Energy and Device Size Limits on Digital Photonic Signal Processing Technologies," *IEEE J. Quantum Electron.* **14**(3), 938–945 (2008).

[11] R. W. Boyd, *Nonlinear Optics*, Acad. Press (2003).

[12] A. V. Zayats, I. I. Smolyaninov, and A. A. Maradudin, "Nano-Optics of Surface Plasmon Polaritons," *Physics Reports* **408**(3–4), 131–314 (2005).

[13] H. Ditlbacher, A. Hohenau, D. Wagner, U. Kreibig, M. Rogers, F. Hofer, F. R. Aussenegg, and J. R. Krenn, "Silver Nanowires as Surface Plasmon Resonators," *Phys. Rev. Lett.* **95**(25), 257403 (2005).

[14] H. Wei, Z. Li, X. Tian, Z. Wang, F. Cong, N. Liu, S. Zhang, P. Nordlander, N. J. Halas, et al., "Quantum Dot-Based Local Field Imaging Reveals Plasmon-Based Interferometric Logic in Silver Nanowire Networks," *Nano Lett.* **11**(2), 471–475 (2011).

[15] A. V. Akimov, A. Mukherjee, C. L. Yu, D. E. Chang, A. S. Zibrov, P. R. Hemmer, H. Park, and M. D. Lukin, "Generation of Single Optical Plasmons in Metallic Nanowires Coupled to Quantum Dots," *Nature* **450**(7168), 402–406 (2007).

[16] D. E. Chang, A. S. Sørensen, P. R. Hemmer, and M. D. Lukin, "Quantum Optics with Surface Plasmons," *Phys. Rev. Lett.* **97**(5), 053002 (2006).

[17] D. E. Chang, A. S. Sørensen, E. A. Demler, and M. D. Lukin, "A Single-Photon Transistor Using Nanoscale Surface Plasmons," *Nature Physics* **3**(11), 807–812 (2007).

[18] D. Ratchford, F. Shafiei, S. Kim, S. K. Gray, and X. Li, "Manipulating Coupling between a Single Semiconductor Quantum Dot and Single Gold Nanoparticle," *Nano Lett.* **11**(3), 1049–1054 (2011).

[19] P. Michler, A. Imamoglu, M. D. Mason, P. J. Carson, G. F. Strouse, and S. K. Buratto, "Quantum Correlation Among Photons from a Single Quantum Dot at Room Temperature," *Nature* **406**(6799), 968–970 (2000).

[20] A. Kongkanand, K. Tvrdy, K. Takechi, M. Kuno, and P. V. Kamat, "Quantum Dot Solar Cells. Tuning Photoresponse through Size and Shape Control of CdSe–TiO2 Architecture," *J. Amer. Chem. Soc.* **130**(12), 4007–4015 (2011).

[21] J. M. Caruge, J. E. Halpert, V. Wood, V. Bulović, and M. G. Bawendi, "Colloidal Quantum-Dot Light-Emitting Diodes with Metal-Oxide Charge Transport Layers," *Nature Photon.* **2**(4), 247–250 (2008).

[22] S. Fafard, K. Hinzer, S. Raymond, M. Dion, J. McCaffrey, Y. Feng, and S. Charbonneau, "Red-Emitting Semiconductor Quantum Dot Lasers," *Science* **274**(5291), 1350–1353 (1996).

[23] P. Michler, A. Kiraz, C. Becher, W. V. Schoenfeld, P. M. Petroff, L. Zhang, E. Hu, and A. Imamoglu, "A Quantum Dot Single-Photon Turnstile Device," *Science* **290**(5500), 2282–2285 (2000).

[24] M. Han, X. Gao, J. Z. Su, and S. Nie, "Quantum-Dot-Tagged Microbeads for Multiplexed Optical Coding of Biomolecules," *Nat Biotech* **19**(7), 631–635 (2001).

[25] I. L. Medintz, H. T. Uyeda, E. R. Goldman, and H. Mattoussi, "Quantum Dot Bioconjugates for Imaging, Labelling and Sensing," *Nat. Mater.* **4**(6), 435–446 (2005).

[26] W. C. W. Chan and S. Nie, "Quantum Dot Bioconjugates for Ultrasensitive Nonisotopic Detection," *Science* **281**(5385), 2016 –2018 (1998).

[27] J.-Y. Marzin, J.-M. Gérard, A. Izraël, D. Barrier, and G. Bastard, "Photoluminescence of Single InAs Quantum Dots Obtained by Self-Organized Growth on GaAs," *Phys. Rev. Lett.* **73**(5), 716–719 (1994).

[28] A. Issac, C. von Borczyskowski, and F. Cichos, "Correlation Between Photoluminescence Intermittency of CdSe Quantum Dots and Self-Trapped States in Dielectric Media," *Phys. Rev. B* **71**(16), 161302 (2005).

[29] B. O. Dabbousi, J. Rodriguez-Viejo, F. V. Mikulec, J. R. Heine, H. Mattoussi, R. Ober, K. F. Jensen, and M. G. Bawendi, "(CdSe)ZnS Core−Shell Quantum Dots: Synthesis and Characterization of a Size Series of Highly Luminescent Nanocrystallites," *J. Phys. Chem. B* **101**(46), 9463–9475 (1997).

[30] Y. Toda, O. Moriwaki, M. Nishioka, and Y. Arakawa, "Efficient Carrier Relaxation Mechanism in InGaAs/GaAs Self-Assembled Quantum Dots Based on the Existence of Continuum States," *Phys. Rev. Lett.* **82**(20), 4114–4117 (1999).

[31] M. V. Artemyev, U. Woggon, R. Wannemacher, H. Jaschinski, and W. Langbein, "Light Trapped in a Photonic Dot: Microspheres Act as a Cavity for Quantum Dot Emission," *Nano Lett.* **1**(6), 309–314 (2001).

[32] A. Drezet, A. Cuche, and S. Huant, "Near-Field Microscopy with a Single-Photon Point-like Emitter: Resolution Versus the Aperture Tip?," *Optics Communications* **284**(5), 1444–1450 (2011).

[33] I. L. Medintz, A. R. Clapp, H. Mattoussi, E. R. Goldman, B. Fisher, and J. M. Mauro, "Self-Assembled Nanoscale Biosensors Based on Quantum Dot FRET Donors," *Nat Mater* **2**(9), 630–638 (2003).

[34] A. E. Cohen and W. E. Moerner, "Suppressing Brownian Motion of Individual Biomolecules in Solution," *Proc. Natl. Acad. Sci. U.S.A* **103**(12), 4362–4365 (2006).

[35] Y. Sonnefraud, N. Chevalier, J.-F. Motte, S. Huant, P. Reiss, J. Bleuse, F. Chandezon, M. T. Burnett, W. Ding, et al., "Near-Field Optical Imaging with a CdSe Single Nanocrystal-Based Active Tip," *Opt. Express* **14**, 10596–10602 (2006).

[36] L. Jauffred, A. C. Richardson, and L. B. Oddershede, "Three-Dimensional Optical Control of Individual Quantum Dots," *Nano Lett.* **8**(10), 3376–3380 (2008).

[37] M. Dienerowitz, M. Mazilu, and K. Dholakia, "Optical Manipulation of Nanoparticles: A Review," *J. Nanophoton.* **2**(1), 021875 (2008).

[38] F. Amblard, B. Yurke, A. Pargellis, and S. Leibler, "A Magnetic Manipulator for Studying Local Rheology and Micromechanical Properties of Biological Systems," *Rev. Sci. Instrum.* **67**(3), 818–827 (1996).

[39] A. Ramos, H. Morgan, N. G. Green, and A. Castellanos, "AC Electrokinetics: A Review of Forces in Microelectrode Structures," *J. Phys. D Appl. Phys.* **31**(18), 2338–2353 (1998).

[40] O. Benson, "Assembly of Hybrid Photonic Architectures from Nanophotonic Constituents," *Nature* **480**, 193–199 (2011).

[41] M. Sitti and H. Hashimoto, "Controlled Pushing of Nanoparticles: Modeling and Experiments," *IEEE/ASME Transactions on Mechatronics* **5**(2), 199–211 (2000).

[42] S. J. Chey, L. Huang, and J. H. Weaver, "Manipulation and Writing with Ag Nanocrystals on Si(111)-7 x 7," *Appl. Phys. Lett.* **72**(21), 2698–2700 (1998).

[43] K. Neuman, E. Chadd, G. Liou, and S. Block, "Characterization of Photodamage to Escherichia Coli in Optical Traps," *Biophys J.* **77**(5), 2856–2863 (1999).

[44] R. F. Probstein, *Physicochemical Hydrodynamics*, John Wiley and Sons (1994).

[45] M. Armani, S. Chaudhary, R. Probst, and B. Shapiro, "Using Feedback Control and Micro-Fluidics to Steer Individual Particles," in *18th IEEE Int. Conf. Micro Electro Mechan. Syst., Miami, FL*, pp. 855–858 (2005).

[46] A. Badolato, K. Hennessy, M. Atatüre, J. Dreiser, E. Hu, P. M. Petroff, and A. Imamoğlu, "Deterministic Coupling of Single Quantum Dots to Single Nanocavity Modes," *Science* **308**(5725), 1158–1161 (2005).

[47] K. Hennessy, A. Badolato, M. Winger, D. Gerace, M. Atatüre, S. Gulde, S. Fält, E. L. Hu, and A. Imamoğlu, "Quantum nature of a strongly coupled single quantum dot–cavity system," *Nature* **445**(7130), 896–899 (2007).

[48] D. Englund, A. Faraon, I. Fushman, N. Stoltz, P. Petroff, and J. Vučković, "Controlling cavity reflectivity with a single quantum dot," *Nature* **450**(7171), 857–861 (2007).

[49] S. Schietinger, M. Barth, T. Aichele, and O. Benson, "Plasmon-Enhanced Single Photon Emission from a Nanoassembled Metal–Diamond Hybrid Structure at Room Temperature," *Nano Lett.* **9**(4), 1694–1698 (2009).

[50] E. Waks and J. Vuckovic, "Dipole Induced Transparency in Drop-Filter Cavity-Waveguide Systems," *Phys. Rev. Lett.* **96**(15), 153601–153604 (2006).

[51] N. Engheta, "Circuits with Light at Nanoscales: Optical Nanocircuits Inspired by Metamaterials," *Science* **317**(5845), 1698–1702 (2007).

[52] A. Ashkin, J. M. Dziedzic, J. E. Bjorkholm, and S. Chu, "Observation of a Single-Beam Gradient Force Optical Trap for Dielectric Particles," *Opt. Lett.* **11**(5), 288–290 (1986).

[53] Pei-Yu Chiou, A. T. Ohta, A. Jamshidi, Hsin-Yi Hsu, and M. C. Wu, "Light-Actuated AC Electroosmosis for Nanoparticle Manipulation," *J. Microelectromech. Syst.* **17**(3), 525–531 (2008).

[54] A. H. J. Yang, S. D. Moore, B. S. Schmidt, M. Klug, M. Lipson, and D. Erickson, "Optical Manipulation of Nanoparticles and Biomolecules in Sub-Wavelength Slot Waveguides," *Nature* **457**(7225), 71–75 (2009).

[55] R. E. Thompson, D. R. Larson, and W. W. Webb, "Precise Nanometer Localization Analysis for Individual Fluorescent Probes," *Biophys. J.* **82**, 2775–2783 (2002).

[56] M. Armani, S. Chaudhary, R. Probst, and B. Shapiro, "Micro Flow Control Particle Tweezers," *uTAS 2004, Malmo, Sweden* (2004).

[57] A. E. Cohen and W. E. Moerner, "Method for Trapping and Manipulating Nanoscale Objects in Solution," *Appl. Phys. Lett.* **86**(9), 093109–3 (2005).

[58] A. E. Cohen, "Control of Nanoparticles with Arbitrary Two-Dimensional Force Fields," *Phys. Rev. Lett.* **94**(11), 118102 (2005).

[59] S. Chaudhary and B. Shapiro, "Arbitrary Steering of Multiple Particles Independently in an Electro-Osmotically Driven Microfluidic System," *IEEE Trans. Contr. Syst. Technol.* **14**(4), 669–680 (2006).

[60] M. D. Armani, S. V. Chaudhary, R. Probst, and B. Shapiro, "Using Feedback Control of Microflows to Independently Steer Multiple Particles," *J. Microelectromech. Syst.* **15**(4), 945–956 (2006).

[61] J. Enderlein, "Tracking of Fluorescent Molecules Diffusing within Membranes," *Appl. Phys. B-Lasers O* **71**(5), 773–777 (2000).

[62] V. Levi, Q. Ruan, K. Kis-Petikova, and E. Gratton, "Scanning FCS, a Novel Method for Three-Dimensional Particle Tracking," *Biochem. Soc. Trans* **31**(Pt 5), 997–1000 (2003).

[63] A. Berglund and H. Mabuchi, "Tracking-FCS: Fluorescence correlation spectroscopy of individual particles," *Opt. Express* **13**(20), 8069–8082 (2005).

[64] A. J. Berglund and H. Mabuchi, "Performance Bounds on Single-Particle Tracking by Fluorescence Modulation," *Appl. Phys. B* **83**(1), 127–133 (2006).

[65] K. McHale, A. J. Berglund, and H. Mabuchi, "Quantum Dot Photon Statistics Measured by Three-Dimensional Particle Tracking," *Nano Lett.* **7**(11), 3535–3539 (2007).

[66] A. E. Cohen and W. E. Moerner, "Controlling Brownian Motion of Single Protein Molecules and Single Fluorophores in Aqueous Buffer," *Opt. Express* **16**(10), 6941–6956 (2008).

[67] Y. Jiang, Q. Wang, A. E. Cohen, N. Douglas, J. Frydman, and W. E. Moerner, "Hardware-Based Anti-Brownian Electrokinetic Trap (ABEL Trap) for Single Molecules: Control Loop Simulations and Application to ATP Binding Stoichiometry in Multi-Subunit Enzymes," in *Optical Trapping and Optical Micromanipulation V* **7038**, pp. 703807–703812, SPIE, San Diego, CA, USA (2008).

[68] W. G. J. H. M. van Sark, P. Frederix, A. A. Bol, H. C. Gerritsen, and A. Meijerink, "Blueing, Bleaching, and Blinking of Single CdSe/ZnS Quantum Dots," *ChemPhysChem* **3**(10), 871–879 (2002).

[69] R. Kumar and S. R. Raghavan, "Thermothickening in Solutions of Telechelic Associating Polymers and Cyclodextrins," *Langmuir* **26**(1), 56–62 (2010).

[70] Kumar, R., Kalur, G.C., Ziserman, L., Danino, D., and Raghavan, S.R., "Wormlike Micelles of a C22-Tailed Zwitterionic Betaine Surfactant: From Viscoelastic Solutions to Elastic Gels," *Langmuir* **23**, 12849–12856 (2007).

[71] R. Borsali and R. Pecora, *Soft Matter*, Springer (2008).

[72] S. Hohng and T. Ha, "Near-Complete Suppression of Quantum Dot Blinking in Ambient Conditions," *J. Am. Chem. Soc* **126**(5), 1324–1325 (2004).

[73] B. Lounis, H. A. Bechtel, D. Gerion, P. Alivisatos, and W. E. Moerner, "Photon Antibunching in Single CdSe/ZnS Quantum Dot Fluorescence," *Chem. Phys. Lett.* **329**(5-6), 399–404 (2000).

[74] R. Probst and B. Shapiro, "Three-Dimensional Electrokinetic Tweezing: Device Design, Modeling, and Control Algorithms," *J. Micromech. Microeng.* **21**(2), 027004 (2011).

[75] Q. Zhang, C. Dang, H. Urabe, J. Wang, S. Sun, and A. Nurmikko, "Large Ordered Arrays of Single Photon Sources Based on II-VI Semiconductor Colloidal Quantum Dot," *Opt. Express* **16**(24), 19599, 19592 (2008).

[76] J. Liu, D. Gao, H.-F. Li, and J.-M. Lin, "Controlled Photopolymerization of Hydrogel Microstructures Inside Microchannels for Bioassays," *Lab. Chip* **9**(9), 1301–1305 (2009).

[77] C. W. Wong, J. Gao, J. F. McMillan, F. W. Sun, and R. Bose, "Quantum Information Processing Through Quantum Dots in Slow-Light Photonic Crystal Waveguides," *Photonics Nanostruct* **7**(1), 47–55 (2009).

[78] C. Santori, M. Pelton, G. Solomon, Y. Dale, and Y. Yamamoto, "Triggered Single Photons from a Quantum Dot," *Phys. Rev. Lett.* **86**(8), 1502 (2001).

[79] Z. Yuan, B. E. Kardynal, R. M. Stevenson, A. J. Shields, C. J. Lobo, K. Cooper, N. S. Beattie, D. A. Ritchie, and M. Pepper, "Electrically Driven Single-Photon Source," *Science* **295**(5552), 102–105 (2002).

[80] D. L. Huffaker, G. Park, Z. Zou, O. B. Shchekin, and D. G. Deppe, "1.3 μm room-temperature GaAs-based quantum-dot laser," *Appl. Phys. Lett.* **73**(18), 2564 (1998).

[81] I. Fushman, D. Englund, A. Faraon, N. Stoltz, P. Petroff, and J. Vuckovic, "Controlled Phase Shifts with a Single Quantum Dot," *Science* **320**(5877), 769–772 (2008).

[82] C. Ropp, R. Probst, Z. Cummins, R. Kumar, A. J. Berglund, S. R. Raghavan, E. Waks, and B. Shapiro, "Manipulating Quantum Dots to Nanometer Precision by Control of Flow," *Nano Lett.* **10**(7), 2525–2530 (2010).

[83] K. Kojima, M. Ito, H. Morishita, and N. Hayashi, "A Novel Water-Soluble Photoinitiator for the Acrylic Photopolymerization Type Resist System," *Chem. Mater.* **10**(11), 3429–3433 (1998).

[84] C. N. LaFratta, J. T. Fourkas, T. Baldacchini, and R. A. Farrer, "Multiphoton Fabrication," *Angew. Chem. Int. Ed.* **46**(33), 6238–6258 (2007).

[85] S. Maruo and J. T. Fourkas, "Recent Progress in Multiphoton Microfabrication," *Laser Photonics Rev.* **2**(1-2), 100–111 (2008).

[86] A. E. Siegman, *Lasers*, University Science Books (1986).

[87] H. P. Kao and A. S. Verkman, "Tracking of Single Fluorescent Particles in Three Dimensions: Use of Cylindrical Optics to Encode Particle Position.," *Biophys. J.* **67**(3), 1291–1300 (1994).

[88] S. R. P. Pavani, M. A. Thompson, J. S. Biteen, S. J. Lord, N. Liu, R. J. Twieg, R. Piestun, and W. E. Moerner, "Three-Dimensional, Single-Molecule Fluorescence Imaging Beyond the Diffraction Limit by Using a Double-Helix Point Spread Function," *Proc. Natl. Acad. Sci. U.S.A* **106**(9), 2995–2999 (2009).

[89] M. W. Knight, N. K. Grady, R. Bardhan, F. Hao, P. Nordlander, and N. J. Halas, "Nanoparticle-Mediated Coupling of Light into a Nanowire," *Nano Lett.* **7**(8), 2346–2350 (2007).

[90] S. Y. Lee, L. Hung, G. S. Lang, J. E. Cornett, I. D. Mayergoyz, and O. Rabin, "Dispersion in the SERS Enhancement with Silver Nanocube Dimers," *ACS Nano* **4**(10), 5763–5772 (2010).

[91] C. Ropp, Z. Cummins, R. Probst, S. Qin, J. T. Fourkas, B. Shapiro, and E. Waks, "Positioning and Immobilization of Individual Quantum Dots with Nanoscale Precision," *Nano Lett.* **10**(11), 4673–4679 (2010).

[92] M. E. J. Friese, T. A. Nieminen, N. R. Heckenberg, and H. Rubinsztein-Dunlop, "Optical Alignment and Spinning of Laser-Trapped Microscopic Particles," *Nature* **394**(6691), 348–350 (1998).

[93] L. Sacconi, G. Romano, R. Ballerini, M. Capitanio, M. De Pas, M. Giuntini, D. Dunlap, L. Finzi, and F. S. Pavone, "Three-Dimensional Magneto-Optic Trap for Micro-Object Manipulation," *Opt. Lett.* **26**(17), 1359–1361 (2001).

[94] P. P. Mathai, A. J. Berglund, J. Alexander Liddle, and B. A. Shapiro, "Simultaneous Positioning and Orientation of a Single Nano-Object by Flow Control: Theory and Simulations," *New J. Phys.* **13**(1), 013027 (2011).

[95] P. P. Mathai, P. T. Carmichael, B. A. Shapiro, and J. A. Liddle, "Simultaneous Positioning and Orientation of Single Nano-Wires Using Flow Control," *RSC Adv.* **3**(8), 2677–2682 (2013).

[96] R. M. Dickson and L. A. Lyon, "Unidirectional Plasmon Propagation in Metallic Nanowires," *J. Phys. Chem. B* **104**(26), 6095–6098 (2000).

[97] J. A. Fan, C. Wu, K. Bao, J. Bao, R. Bardhan, N. J. Halas, V. N. Manoharan, P. Nordlander, G. Shvets, et al., "Self-Assembled Plasmonic Nanoparticle Clusters," *Science* **328**(5982), 1135–1138 (2010).

[98] P. Anger, P. Bharadwaj, and L. Novotny, "Enhancement and Quenching of Single-Molecule Fluorescence," *Phys. Rev. Lett.* **96**(11), 113002 (2006).

[99] A. G. Curto, G. Volpe, T. H. Taminiau, M. P. Kreuzer, R. Quidant, and N. F. van Hulst, "Unidirectional Emission of a Quantum Dot Coupled to a Nanoantenna," *Science* **329**(5994), 930 –933 (2010).

[100] A. Nahata, R. A. Linke, T. Ishi, and K. Ohashi, "Enhanced Nonlinear Optical Conversion from a Periodically Nanostructured Metal Film," *Opt. Lett.* **28**(6), 423–425 (2003).

[101] S. Kim, J. Jin, Y.-J. Kim, I.-Y. Park, Y. Kim, and S.-W. Kim, "High-Harmonic Generation by Resonant Plasmon Field Enhancement," *Nature* **453**(7196), 757–760 (2008).

[102] S. Nie and S. R. Emory, "Probing Single Molecules and Single Nanoparticles by Surface-Enhanced Raman Scattering," *Science* **275**(5303), 1102 –1106 (1997).

[103] A. J. Haes and R. P. Van Duyne, "A Nanoscale Optical Biosensor: Sensitivity and Selectivity of an Approach Based on the Localized Surface Plasmon Resonance Spectroscopy of Triangular Silver Nanoparticles," *J. Am. Chem. Soc.* **124**(35), 10596–10604 (2011).

[104] S. I. Bozhevolnyi and B. Vohnsen, "Near-Field Optics with Uncoated Fiber Tips: Light Confinement and Spatial Resolution," *J. Opt. Soc. Am. B* **14**(7), 1656–1663 (1997).

[105] B. Hecht, B. Sick, U. P. Wild, V. Deckert, R. Zenobi, O. J. F. Martin, and D. W. Pohl, "Scanning Near-Field Optical Microscopy with Aperture Probes: Fundamentals and Applications," *J. Chem. Phys.* **112**(18), 7761–7774 (2000).

[106] Y. Inouye and S. Kawata, "Near-Field Scanning Optical Microscope with a Metallic Probe Tip," *Opt. Lett.* **19**(3), 159–161 (1994).

[107] F. Zenhausern, M. P. O'Boyle, and H. K. Wickramasinghe, "Apertureless Near-Field Optical Microscope," *Appl. Phys. Lett.* **65**(13), 1623–1625 (1994).

[108] J. Dorfmüller, R. Vogelgesang, R. T. Weitz, C. Rockstuhl, C. Etrich, T. Pertsch, F. Lederer, and K. Kern, "Fabry-Pérot Resonances in One-Dimensional Plasmonic Nanostructures," *Nano Lett.* **9**(6), 2372–2377 (2009).

[109] M. Schnell, A. Garcia-Etxarri, J. Alkorta, J. Aizpurua, and R. Hillenbrand, "Phase-Resolved Mapping of the Near-Field Vector and Polarization State in Nanoscale Antenna Gaps," *Nano Lett.* **10**(9), 3524–3528 (2010).

[110] K. Imura and H. Okamoto, "Reciprocity in Scanning Near-Field Optical Microscopy: Illumination and Collection Modes of Transmission Measurements," *Opt. Lett.* **31**(10), 1474–1476 (2006).

[111] H. Yao, Z. Li, and Q. Gong, "Coupling-Induced Excitation of a Forbidden Surface Plasmon Mode of a Gold Nanorod," *Sci. China Ser. G-Phys. Mech. Astron.* **52**(8), 1129–1138 (2009).

[112] J. Nelayah, M. Kociak, O. Stéphan, F. J. G. de Abajo, M. Tencé, L. Henrard, D. Taverna, I. Pastoriza-Santos, L. M. Liz-Marzán, et al., "Mapping Surface Plasmons on a Single Metallic Nanoparticle," *Nature Physics* **3**(5), 348–353 (2007).

[113] E. J. R. Vesseur, R. de Waele, M. Kuttge, and A. Polman, "Direct Observation of Plasmonic Modes in Au Nanowires Using High-Resolution Cathodoluminescence Spectroscopy," *Nano Lett.* **7**(9), 2843–2846 (2007).

[114] M. Frimmer, T. Coenen, and A. F. Koenderink, "Signature of a Fano Resonance in a Plasmonic Metamolecule's Local Density of Optical States," *Phys. Rev. Lett.* **108**(7), 077404 (2012).

[115] M. Frimmer, Y. Chen, and A. F. Koenderink, "Scanning Emitter Lifetime Imaging Microscopy for Spontaneous Emission Control," *Phys. Rev. Lett.* **107**(12), 123602 (2011).

[116] J. Michaelis, C. Hettich, J. Mlynek, and V. Sandoghdar, "Optical Microscopy Using a Single-Molecule Light Source," *Nature* **405**(6784), 325–328 (2000).

[117] A. Cuche, A. Drezet, Y. Sonnefraud, O. Faklaris, F. Treussart, J.-F. Roch, and S. Huant, "Near-Field Optical Microscopy with a Nanodiamond-Based Single-Photon tip," *Opt. Express* **17**(22), 19969–19980 (2009).

[118] G. T. Shubeita, S. K. Sekatskii, G. Dietler, I. Potapova, A. Mews, and T. Basché, "Scanning Near‐Field Optical Microscopy Using Semiconductor Nanocrystals as a Local Fluorescence and Fluorescence Resonance Energy Transfer Source," *J. Microsc.* **210**(3), 274–278 (2003).

[119] A. Huck, S. Kumar, A. Shakoor, and U. L. Andersen, "Controlled Coupling of a Single Nitrogen-Vacancy Center to a Silver Nanowire," *Phys. Rev. Lett.* **106**(9), 096801 (2011).

[120] A. W. Schell, G. Kewes, T. Hanke, A. Leitenstorfer, R. Bratschitsch, O. Benson, and T. Aichele, "Single Defect Centers in Diamond Nanocrystals as Quantum Probes for Plasmonic Nanostructures," *Opt. Express* **19**(8), 7914–7920 (2011).

[121] M. Geiselmann, M. L. Juan, J. Renger, J. M. Say, L. J. Brown, F. J. G. de Abajo, F. Koppens, and R. Quidant, "Three-Dimensional Optical Manipulation of a Single Electron Spin," *Nature Nanotech.* **8**(3), 175–179 (2013).

[122] H. Cang, A. Labno, C. Lu, X. Yin, M. Liu, C. Gladden, Y. Liu, and X. Zhang, "Probing the Electromagnetic Field of a 15-Nanometre Hotspot by Single Molecule Imaging," *Nature* **469**(7330), 385–388 (2011).

[123] J. N. Farahani, D. W. Pohl, H.-J. Eisler, and B. Hecht, "Single Quantum Dot Coupled to a Scanning Optical Antenna: A Tunable Superemitter," *Phys. Rev. Lett.* **95**(1), 017402 (2005).

[124] U. Hohenester and A. Trugler, "Interaction of Single Molecules With Metallic Nanoparticles," *IEEE J. Quantum Electron.* **14**(6), 1430 –1440 (2008).

[125] S. A. Empedocles, R. Neuhauser, and M. G. Bawendi, "Three-Dimensional Orientation Measurements of Symmetric Single Chromophores Using Polarization microscopy," *Nature* **399**(6732), 126–130 (1999).

[126] C. Chicanne, T. David, R. Quidant, J. C. Weeber, Y. Lacroute, E. Bourillot, A. Dereux, G. Colas des Francs, and C. Girard, "Imaging the Local Density of States of Optical Corrals," *Phys. Rev. Lett.* **88**(9), 097402 (2002).

[127] K. T. Shimizu, R. G. Neuhauser, C. A. Leatherdale, S. A. Empedocles, W. K. Woo, and M. G. Bawendi, "Blinking Statistics in Single Semiconductor Nanocrystal Quantum Dots," *Phys. Rev. B* **63**(20), 205316 (2001).

[128] C. A. Balanis, *Advanced Engineering and Electromagnetics*, John Wiley & Sons (2011).

[129] G.-W. Shu, W.-Z. Lee, I.-J. Shu, J.-L. Shen, J. C.-A. Lin, W. H. Chang, R.-C. Ruaan, and W. C. Chou, "Photoluminescence of Colloidal CdSe/ZnS Quantum Dots Under Oxygen Atmosphere," *IEEE T. Nanotechnol.* **4**(5), 632 – 636 (2005).

[130] W. van Sark, P. L. T. M. Frederix, D. J. Van den Heuvel, H. C. Gerritsen, A. A. Bol, J. N. J. van Lingen, C. de Mello Donegá, and A. Meijerink, "Photooxidation and Photobleaching of Single CdSe/ZnS Quantum Dots Probed by Room-Temperature Time-Resolved Spectroscopy," *The Journal of Physical Chemistry B* **105**(35), 8281–8284 (2001).

[131] P. W. Milonni and J. H. Eberly, *Lasers*, Wiley-Interscience (1988).

[132] C. Kurtsiefer, S. Mayer, P. Zarda, and H. Weinfurter, "Stable Solid-State Source of Single Photons," *Phys. Rev. Lett.* **85**(2), 290–293 (2000).

[133] K. T. Early, P. K. Sudeep, T. Emrick, and M. D. Barnes, “Polarization-Driven Stark Shifts in Quantum Dot Luminescence from Single CdSe/oligo-PPV Nanoparticles,” *Nano Lett.* **10**(5), 1754–1758 (2010).